Quantification and Minimization the Uncertainty Propagation of Monte Carlo Cross Section Generation for HTR Applications

by

Jin Li

A dissertation submitted in partial fulfillment
of the requirements for the degree of
Doctor of Philosophy
(Nuclear Engineering and Radiological Sciences)
in the University of Michigan
2023

Doctoral Committee:

- Professor Thomas Downar, Chair
- Professor Liliana Borcea
- Professor Brendan Kochunas
- Assistant Research Scientist Volkan Seker
- Professor Won Sik Yang

Jin Li
lijinthu@umich.edu
ORCID iD: 0000-0003-4622-7609

Dedication

For all who love and support me

ACKNOWLEDGEMENTS

First, I would like to thank my advisor, Professor Thomas Downar, for his guidance, support and patience throughout my Ph.D. study. Prof. Downar has profound knowledge and extensive experience in the field of nuclear engineering, and I have been greatly benefited from his mentorship. I feel extremely fortunate and honored to be his last Ph.D. student. His guidance has not only shaped my academic journey but also contributed to my personal growth.

Second, I would like to thank all my committee members. Doctor Volkan Seker is the author of the AGREE code. My research would not have been possible without his support. Professor Brendan Kochunas has been helping me a lot since I came to the University of Michigan. His comments and suggestions can always inspire me to explore more in my research. Professor Won Sik Yang has provided me with many valuable suggestions and comments on my research. His insight and knowledge have been very helpful for me to improve my research. Professor Liliana Borcea is the teacher of my numerical linear algebra course. The linear algebra knowledge I learned from her course has been very useful for my research and will help me in my future career.

I would also like to thank all my colleagues in our research team. Doctor Andrew Ward is the author of the GenPMAXS code. He has provided a lot of technical support for my research. I have collaborated with Doctor Shai Kinast and Kaitlyn Barr. We have all benefited a lot from each other. The atmosphere within our research group has always been harmonious, and I feel fortunate to engage in meetings and discussions with these colleagues, which brings me a sense of happiness. I worked closely with Doctor Shen Qicang, Doctor Dan Jabaay and Doctor Albert Hsieh during my first two years in UM. They have helped me a lot in my research. I came to UM with Kyle Vaughn, Mattew Kabelitz and Nickolas Herring in the same year and we had several classes together. I would like to thank them for the help they provided to me. I would also like to thank Thomas Folk, who has discussed with me for some issues in my research.

Besides, I would like to thank all the friends I met during the past five years. I knew some of them in the NERS Department, including Shen Qicang, Che Shuai, Yang Zimu, Zhao Chen, Liu Yuxuan, Wang Jipu, Chen Zhuo, Wang Yuhao, Qin Sunming, Mao Jiaxin, Yang Gang. We used to have lunch together at Pierpont Commons before the pandemic. I knew some of them in other occasions, including Yang Zhuoran, Zan Xin, Dong Tianshu, Tang Hongmei, Xu Haokui, Wen Lu, Yao Li'ang, Deng Changyu. Two friends, Wang Yiran and Xu Weiran, are I knew since

undergraduate and we came to the U.S. for Ph.D. study together. All the friends, including those who I haven't mention their name explicitly here, are who I played tennis with, went to skiing with, visited nearby parks with and tried tasty food with. We have also traveled together to many places. I treasure the joyful and unforgettable moments we spent together. You companionship has made me go through the difficult times and enjoy the happy times.

Finally, I have special thanks to the teachers I met. Professor Yang Zhenwei was my head teacher in undergraduate. His passion and dedication to research have inspired me and led me into the field of scientific research. Professor Yu Ganglin and Professor Wang Kan were the professors who introduced me to the field of nuclear engineering. During my early days in research, they provided me with invaluable assistance and guidance. I would also like to thank Professor Jason Hou and Professor Xu Yunlin, who provided me with a lot of help when I came to the U.S. for the short-term internships. They also helped me a lot when I applied to the Ph.D. program in UM. Professor Sun Xiaodong, Professor Wang Lumin and Professor Hao Chen are the professors not only taught me but also invited me to their Thanksgiving or New Year's Eve parties. I would like to thank them for their teaching and kindness.

I would not be able to finish my Ph.D. study without the support and companion of all the people above. Thank you all!

TABLE OF CONTENTS

CHAPTER

LIST OF FIGURES

FIGURE

LIST OF TABLES

TABLE

LIST OF APPENDICES

LIST OF ABBREVIATIONS

AGREE Advance Gas Reactor Evaluator

ANL Argonne National Laboratory

CFD Computational Fluid Dynamics

CFP Coated Fuel Particle

CPT Conventional Perturbation Theory

CZP Cold Zero Power

DOE Department of Energy

FHR Fluoride-salt-cooled High-temperature Reactor

gFHR generic FHR

GenPMAXS Generation of the Purdue Macroscopic XS set

GIF Generation IV Forum

GPU Graphics Processing Unit

HFP Hot Full Power

HTGR High Temperature Gas Reactor

HTR High Temperature Reactor

HZP Hot Zero Power

IAEA International Atomic Energy Agency

INET Institute of Nuclear Energy Technology

KP-FHR Kairos Power FHR

LANL Los Alamos National Laboratory

LWR Light Water Reacttor

MC Monte Carlo

MIT Massachusetts Institute of Technology

MOC Methods of Characteristics

MOOSE Multiphysics Object-Oriented Simulation Environment

NEA Nuclear Energy Agency

NEAMS Nuclear Energy Advanced Modeling and Simulation

OECD Organisation for Economic Co-operation and Development

PB-FHR Pebble-Bed Fluoride-salt-cooled High-temperature Reactor

PKE Point Kinetics Equation

RMS Root Mean Square

RTP Rated Thermal Power

SAM System Analysis Module

SFR Salt-cooled Fast Reactor

SNL Sandia National Laboratory

TH Thermal-Hydraulics

TRISO TRi-structural ISOtropic

UAM Uncertainty Analysis in Modelling

ULOF Unprotected Loss Of Flow

UQ Uncertainty Quantification

XS Cross Section

ABSTRACT

The High Temperature Reactor (HTR) is one of the six Generation IV advanced reactor designs. HTRs have become more and more attractive for power generation applications among both commercial companies and research institutes because of its intrinsically safety and modular design features. For several reasons, the modeling and simulation of HTRs can be much more challenging than traditional Light Water Reactors which rely primarily on deterministic methods to analyze the coupled neutronic and temperature fluid fields. In the research here, hybrid methods combining stochastic Monte Carlo methods and deterministic methods were applied to HTR simulations. In particular, Monte Carlo methods are an attractive alternative to overcome the complexities in the modelling and analysis of the considerable heterogeneity of small modular reactors such as the HTR which use TRISO fuel. In the research here, the Monte Carlo code Serpent was used for few-group neutron cross section generation and the deterministic codes AGREE and SAM were used for neutronics and thermo-fluids transient simulation using the cross sections generated by Serpent.

The stochastic nature of Monte Carlo processes has the potential to introduce additional statistical uncertainties. Quantifying this uncertainty was a principal focus of the research performed here. In order to quantify the uncertainties introduced from Monte Carlo cross section generation, two different methods were investigated, including an analytic perturbation-based method and a stochastic probabilistic method using the industry standard code Dakota. The ultimate objective was to quantify the uncertainty for a model of an advanced HTR, the Kairos Power FHR (KP-FHR) which is a novel advanced reactor technology that leverages TRISO fuel in pebble form combined with a low-pressure fluoride salt coolant. However, the research methods developed here were first demonstrated using an experimental HTR reactor, the HTR-10, which became an international IAEA benchmark and is currently used world-wide to validate computer codes used in the safety analysis of small modular advanced HTRs such as the FHR. Specifically, the four benchmark problems of the HTR-10 were modeled. Good agreement of the deterministic and probabilistic was demonstrated which provided confidence in then applying the stochastic methods to the FHR for both steady-statue and coupled neutron and temperature fluid field transient analysis. Parametric studies were also performed to investigate the factors that may affect the uncertainty quantification. The results for the FHR equilibrium core problem showed that the uncertainty of the k_{eff} and local power introduced from the Monte Carlo generated cross section was small if sufficient number of histories were used to generate the neutron cross sections in Serpent. However, the uncertainty of some important safety parameters, e.g. the region-wise reactivity coefficients, was very large if insufficient numbers of histories were used. A ramp reactivity insertion simulated using the industry standard SAM code with coefficients generated through Serpent/AGREE. Despite the uncertainty of some neutronics parameters being larger, the uncertainty of the important thermo-fluids parameters, such as the maximum coolant and fuel temperature, was still small. For this phase of the research the Dakota code was also coupled with the SAM code to propagate the uncertainties of Serpent/AGREE.

The results of this research demonstrated the use of innovative uncertainty quantification methods and results which provide guidance to reactor analysts on the numbers of histories necessary to minimize the contribution of the uncertainty introduced from Monte Carlo into the prediction of HTR reactor safety performance.

CHAPTER 1

Introduction

1.1 Motivation

The High Temperature Reactor (HTR) is a class of thermal reactors, in which the core contains high temperature coolant and solid fuel. There are several types of HTR designs. Based on the different states of the coolant used, these reactors can be classified into two categories: one uses gas coolant, such as helium gas or carbon dioxide gas; the other uses liquid coolant, such as fluoride salt. Both categories of HTRs use TRi-structural ISOtropic (TRISO) particle as the fuel, despite that some designs are based on the graphite pebble-bed, while other designs are based on the prismatic graphite blocks. Many of HTRs are designed with passively safe features that require best-estimate plus uncertainty analysis of reactor performance [2].

Fig. 1.1 shows the primary and secondary loop of a High Temperature Gas Reactor (HTGR) reactor, which is a typical design for the pebble-bed based HTR reactors. The HTGR operates at significantly higher temperatures compared to traditional water-cooled reactors. HTGRs use helium gas as the coolant to transfer heat from the nuclear fuel to the power generation system. The high operating temperatures of HTGRs offer several advantages, including increased thermal efficiency and the potential for more diverse applications.

Fig. 1.2 shows the system design of an Fluoride-salt-cooled High-temperature Reactor (FHR) reactor. The FHR is another typical design that is based on liquid coolant and pebble-bed core. The fluoride salt coolants are usually eutectic mixtures of liquid fluoride salts such as LiF and BeF_2. The fluoride salts have some good properties, including the relatively low neutron absorption cross section, high power density capacity, high heat transfer efficiency, high boiling temperature, low operation pressure and low chemical reactivity with water and air [3][4], which motivates the economic and intrinsically safe design of FHRs.

The pebble-bed based design attracts a lot of interest for its improved passive safety characteristics at high temperature and the convenience to recycling the fuel during operation. However, there are several challenges associated with pebble-bed reactor modeling. First, the TRISO par-

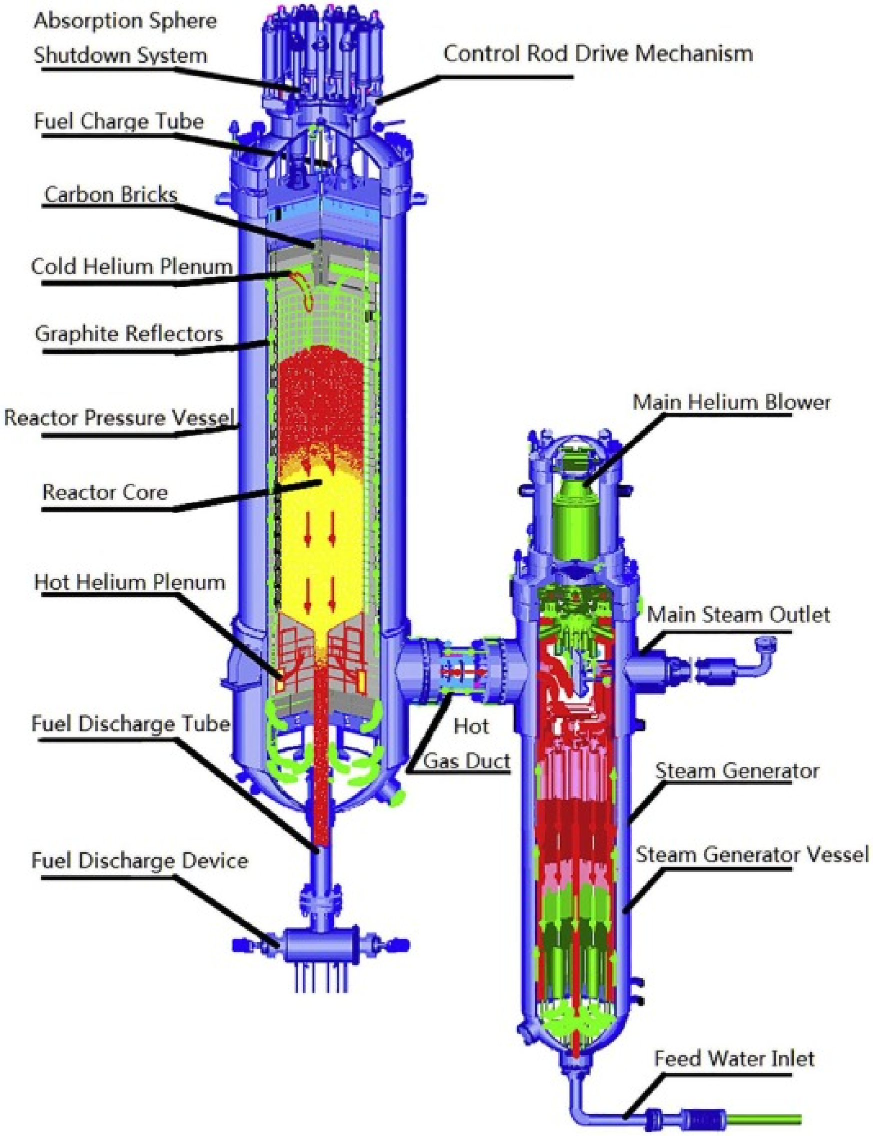

Fig. 1.1: A pebble-bed HTGR design

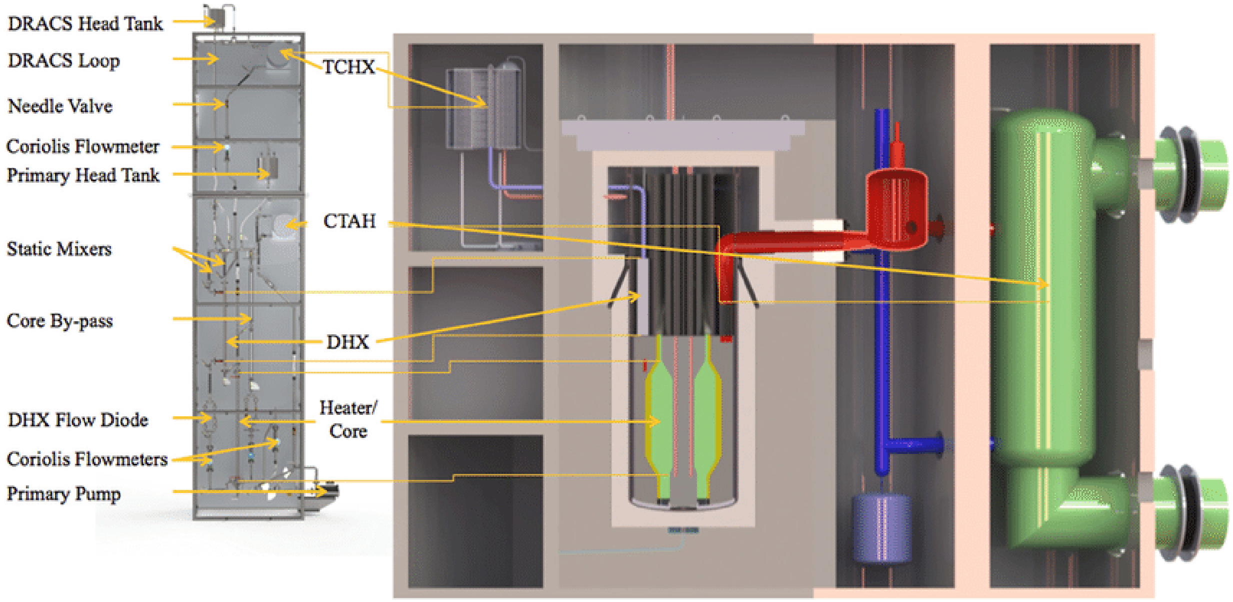

Fig. 1.2: The system design of the Mk1 FHR reactor[1]

ticles inside the pebble and the pebbles inside the core cause a double heterogenous effect in the neutronic analyses. Second, since the pebbles are mixed and recirculated in the core during operation, the depletion calculation becomes a challege because the composition of adjacent pebbles could be very different. Besides, traditional subchannel method for the thermal-hysraulics analysis becomes not suitable due to the random distribution of the pebbles in the core.

To overcome the above difficulties, a combined stochastic and deterministic method becomes more and more popular for advanced reactor studies. These so-called “hybrid” methods usually use the continuous energy (CE) Monte Carlo (MC) neutron transport code to generate few-group cross sections, and the cross sections are then applied to a deterministic code for the core analyses. The hybrid methods take advantage of the complex materials and geometries modeling capability of the stochastic codes, as well as the efficient reactor kinetics solver of the deterministic codes.

However, the stochastic nature of Monte Carlo processes has the potential to introduce additional statistical uncertainties in the overall uncertainty in the prediction of the core behavior. The work performed in this thesis is not to provide a comprehensive uncertainty analysis of the HTR. Rather, the principal objective of the research proposed here is to quantify the additional uncertainty introduced by the use of Monte Carlo multi-group cross sections into the analysis of the HTR. An overarching objective of the work here is the development of modeling guidance and procedures to minimize the contribution of the uncertainty in multi-group cross sections generated by Monte Carlo methods to the overall uncertainty in deterministic calculations.

1.2 Review of Previous Work

1.2.1 HTR Simulation Methods

Thanks to the development of reactor physics, multi-physics coupling, Computational Fluid Dynamics (CFD), and other reactor and system simulation softwares, there have been significant advancements in pebble-bed based reactor simulations in recent years.

A range of computer codes, including reactor physics, thermal-hydraulics, fuel performance and CFD, have been developed for Department of Energy (DOE)'s Nuclear Energy Advanced Modeling and Simulation (NEAMS) program, many of which have the capability to simulate pebble-bed based HTR reactors. Pronghorn is a multidimensional, coarse-mesh, Thermal-Hydraulics (TH) code for advanced reactors[5][6]. It utilizes a multi-scale modeling approach to simulate the pebble-bed based reactors. The multi-scale modeling approach includes three length scales: the macro-scale for the entire reactor core, the meso-scale for a single pebble and the micro-scale for a single Coated Fuel Particle (CFP). SAM is a system-level simulation tool for advanced reactors[7]. It models the pebble-bed reactors with multiple PBCoreChannel components with spherical heat structures. SAM has been applied to the modeling and simulation of the PB-HTGR and PB-FHR reactors[8] [9]. There are also codes developed for the reactor physics and thermal-hydraulics analysis of pebble-bed based reactors which use the Graphics Processing Unit (GPU) to accelerate the simulations, such as Nek5000[10], Cardinal[11] and Project Chrono[12].

1.2.2 UQ Methods

Over the years there has been considerable research related to the quantification of uncertainties in nuclear reactor analysis methods for both existing light water and advanced reactors. In 2013, efforts were initiated by both the Nuclear Energy Agency (NEA) of the Organisation for Economic Co-operation and Development (OECD) Uncertainty Analysis in Modelling (UAM) and the International Atomic Energy Agency (IAEA) to address uncertainty quantification for the HTGR [13]. The uncertainty analysis of HTRs (High Temperature Reactor) was divided into several phases for both the pebble-bed and prismatic HTRs [14]. The essential principles and methods proposed to assess the uncertainty in the HTR were similar in several ways to those used for LWRs (Light Water Reactor) [15]. However, the complexity of the modeling required for HTR analysis can potentially introduce additional uncertainties. Specifically, the traditional "two-step" method used for LWR analysis can be less effective for modeling the HTR core. This is primarily because of the high leakage and the significant spatial variations in the neutron spectrum in the core. Several researchers have demonstrated the advantages of using full core Monte Carlo methods to generate homogenized multi-group cross sections for the small reactors such as the HTR. These cross sections are then be used in deterministic core simulators for steady-state depletion and transient safety analysis.

In recent years, there have been several studies performed to quantify the uncertainty propagation of nuclear data and neutronics parameters to the transient and safety analysis. The work of [16] [17] investigated the impact of nuclear data uncertainties, thermal-physical properties, reactivity coefficients and operational conditions on the transient behaviors of the ABR-1000 reactor. The work employed the PERSENT code based on the COMMARA-2.0 covariance matrix to quantify the uncertainty propagation from nuclear data to the reactivity coefficients and employed the SAS4A/SASSYS-1 and Dakota code to stochastically propagate the neutronics and thermal-hydraulics uncertainties to the Unprotected Loss Of Flow (ULOF) transient analysis. Similar work was also performed by [18] on the Salt-cooled Fast Reactor (SFR) to assist in establishing the priority of future research and development. The approach was also used to validate the best-estimate tools against the experimental measurements of SFR transients Fast Flux Test Facility (FFTF) Loss of Flow Without Scram (LOFWOS) Test #13 by [19].

1.3 Thesis Outline

The detailed structure of this thesis has been shown in the table of contents. At the end of each chapter from Chapter 2 to Chapter 5, a summary is also provided to review the work and summarize the conclusions of each chapter. Therefore, the outline here will only focus on the connections between each chapter.

Chapter 1 introduces the HTGR and FHR as two types of HTR reactors and the difficulties in the modeling because of the double-heterogeneity feature of their pebble-bed based core. This leads to the use of Monte Carlo-deterministic hybrid methods for overcoming the modeling difficulties. The first chapter aims to give a big picture of the work in this thesis. Chapter 2 follows Chapter 1, giving a detailed description of the hybrid methods. The feasibility of the hybrid methods is demonstrated by applying it on the HTR-10 benchmark and gFHR benchmark. The focusing reactor in this thesis is the FHR. The reason for demonstrating the methods on the HTR-10 reactor is that the HTR-10 is a constructed and experimented reactor and its benchmark problems are well-established, while FHR is still a reactor under design.

Chapter 3 addresses that the Monte Carlo cross section generation in the hybrid methods will introduce additional uncertainty to the subsequent simulations. To understand how the Monte Carlo uncertainty propagate into subsequent simulations, it leads to the two uncertainty quantification methods — the analytical method and the stochastic method. The reason to develop two different categories of methods is to validate the results between each other. After some parametric studies and comparisons between the two methods on a simple demonstration problem, the stochastic problem is chosen for its universality and extendibility.

Chapter 4 and Chapter 5 are the practical applications of the stochastic uncertainty quantification method, one for the steady-state simulations and the other for the transient simulations. There are some issues related to the AGREE/SAM simulations or related to the uncertainty quantifications, which are also discussed in the chapters.

Finally, based on the results obtained in Chapter 4 and Chapter 5, Chapter 6 summarizes the work performed in this thesis, presents the conclusions, and discusses potential work for future investigation.

CHAPTER 2

Computational Methods

2.1 Monte Carlo-Deterministic Hybrid Methods

2.1.1 Introduction

The principal goal of simulating a nuclear reactor core is to solve for the neutron multiplication factor k_{eff} and the neutron flux distribution of the core. The methods to achieve the goal can be classified into to categories: one is the stochastic Monte Carlo method, which samples the average neutron behaviour by simulating a large amount of neutrons; the other is the deterministic method, which is aimed to establish and solve the neutron transport equation.

In the past few decades, many computer codes have been successfully developed in each of the two categories of methods. The Monte Carlo method is regarded as the gold standard of the reactor core simulation, which can resolve the neutron transport in the reactor core accurately with minimal simplifications and approximations by stochastically simulating a large number of neutron particles. There are many neutron transport computer codes developed based on the Monte Carlo methods, including the MCNP code developed by Los Alamos National Laboratory (LANL)[20], the OpenMC code developed by Massachusetts Institute of Technology (MIT)[21], the Serpent code developed by VTT Technical Research Centre of Finland[22], the RMC code developed by Tsinghua University[23], etc. The deterministic method aims to solve the Boltzmann neutron transport equation by discretizing the space-angle-energy phase space and transforming the equation into numerically solvable algebra equations. There are many deterministic codes developed based on different discretizing methods. For example, the MPACT code developed by the University of Michigan is based on the Methods of Characteristics (MOC) method[24]; the HELIOS code developed by Studsvik Scandpower is based on two-dimensional collision probabilities transport lattice physics analysis[25]; the AGREE code developed by the University of Michigan is based on solving the 3-D neutron diffusion equation[26]. The two methods and the computer codes based on them are widely used for the conceptual design, safety analysis and commercially licensing all kinds of reactors. However, there are still some limitations of both methods.

The Monte Carlo method usually requires significant computational workload and large memory, especially for the whole core simulation and deep penetration problems[27][28]. For the deterministic code, because of the simplifications and approximations in the core modeling and in the neutron transport equation solving, the accuracy of the solution decreases, especially for the reactor cores with complex geometries and for the resonance self-shielding calculations[29].

Because of above limitations of the Monte Carlo method and deterministic method, the hybrid method that combines the advantages of both methods has been more and more attractive for the advanced reactor simulations with more complex geomtries than traditional LWR lattice geometries over the recent years. The hybrid method employs the Monte Carlo code to generate homogenized few-group cross sections and then the cross sections are fed into the deterministic code for neutronics or multi-physics coupled simulations.

2.1.2 Methodology

The modeling methods used in this research to perform core simulation is depicted in Fig. 2.1. The Monte Carlo code Serpent was used to generate nodal homogenized few-group cross sections which were then converted to cross section data for the Advance Gas Reactor Evaluator (AGREE) code using the cross section converter code GenPMAXS. The neutron diffusion code AGREE was employed as the core simulator and performed both neutronics and thermal-fluids coupled calculations to produce the core power distribution for both steady-state k_{eff} and transient simulations.

The full core Serpent k_{eff} eigenvalue and power distribution results are used as reference for AGREE results. Previous methods used to analyze the HTR relied on a "two-step" in which cross sections were generated using a small "lattice" model with approximate boundary conditions. One example is the work performed by Argonne National Laboratory (ANL) using DRAGON as lattice transport code and DIF3D as nodal diffusion code. In these studies, significant errors were reported using the two-step method which are minimized by using a full core Monte-Carlo model of the core to generate cross sections, such as in the research performed here.

2.2 AGREE Code: Neutronics and Thermo-fluids

2.2.1 AGREE Thermo-Fluids

The AGREE was developed for the U.S. NRC as a thermo-fluids code to solve the steady state and time dependent mass, momentum, and energy equations in three-dimensions for High Temperature Gas Cooled reactor analyses. AGREE has two separate versions, one for Pebble Bed type reactor applications and another for Prismatic "block type" reactors in which the fuel is stationary

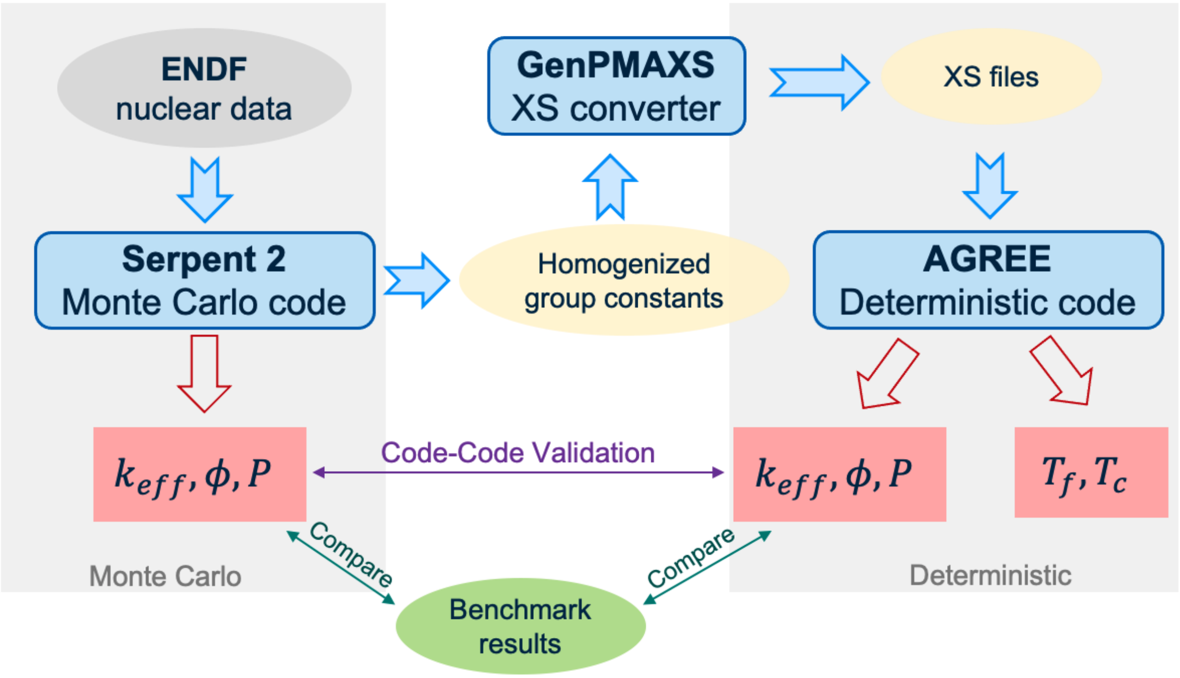

Fig. 2.1: Calculational Methods for High Temperature Reactor Modeling

throughout its burnup cycle. The pebble bed version of AGREE was recently updated to provide functionality for the FHR designed by Kairos Power as well as for the helium cooled HTR designed by X-Energy.

AGREE solves porous media mass, momentum and energy equations in 3D cylindrical geometry, as shown in Fig. 2.2. Due to presence of heat source in the solid (pebble) part of the porous media, the two-equation model for the energy balance is used. Since the convective term in the momentum equation is much smaller compared to the porous resistance, AGREE neglects that term which reduces mass and momentum equation into a pressure equation which can be solved easily by assuming ideal gas or the use of equation of state for gases. Overall AGREE solves three field equations. A pressure equation where the pressure distribution of the system is solved and mass distribution is back-calculated. Two energy equations are solved; one for the gas (fluid) where gas temperature distribution is calculated and one for the solid where solid (pebbles and solid structures) temperature distribution along with the fuel and kernel temperature are calculated.

2.2.2 AGREE Neutronics

As noted above, the "two-step" few-group, homogenized method for solving the neutron transport equation in the reactor core has been used successfully for the analysis of most all large LWRs [30][31][32]. However, the methods have not been as accurate for reactor cores that are not as

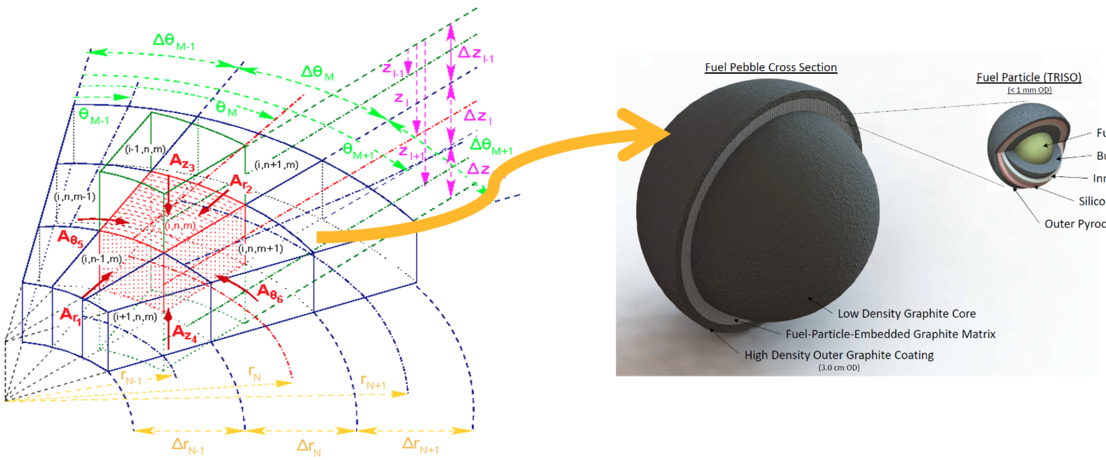

Fig. 2.2: AGREE cylindrical control volume

optically thick and which are not scattering-dominant system which is the case for some of the smaller advanced reactor concepts which have significant neutron leakage. The research here focused on the HTR which is one of the six type reactor designs that were proposed in the Generation IV Forum (GIF) in 2002 [33]. The neutronic modeling of the HTR using the few group homogenized diffusion approximation has several challenges because the additional complexity of the double heterogeneity in modeling pebbles with TRISO fuel [34].

The Monte Carlo Code Serpent directly accounts for the double heterogeneity and together with the deterministic core simulator AGREE are capable of providing computationally efficient and sufficient accuracy for an application such as the HTR. The Serpent Monte Carlo code is a continuous-energy Monte Carlo particle code [35] which has been enabled to generate homogenized cross sections for use in nodal diffusion calculations [36][22]. Although a large number of particle histories can be required to minimize the statistical uncertainty and provide accurate multigroup data, Monte Carlo methods are attractive for cross section generation calculations since they are able to solve arbitrary and complicated three-dimensional problems with minimal physics approximations. This is particularly attractive for modeling the HTR with complex physics such as the double heterogeneity introduced by the TRISO fuel form.

Serpent has unique capabilities with regards to the modeling of pebble bed reactors. Serpent can not only model the random pebble distribution, it can also model the random TRISO distribution inside the pebbles. This modeling is done explicitly in which the location of each pebble is generated using an automated dispersion routine. Serpent only requires a file with the position of each pebble's center point. Serpent uses this information to explicitly represent the location of pebbles in the core without applying any homogenization.

For the analysis of the HTR in this work, Serpent was used for preparation of the multi-group homogenized cross sections as well as to provide a detailed calculation without energy, angular, or spatial discretization error that could be used as a reference to assess the accuracy of the AGREE calculation. The version of Serpent used in this work is 2.1.31.

2.3 Validation of Methods: The HTR-10 Benchmark

The HTR-10 Reactor was completed in 1999 and began operation in China in 2001 [37][38]. Several experiments were designed as part of an international IAEA benchmark [39] [40]. The benchmarks were performed with AGREE using cross sections generated with SERPENT for the AGREE core simulator and results will be summarized here and more details are provided in the Appendix. The primary system of the HTR-10 is shown in Fig. 2.3 and some of the design characteristics again summarized in Table 4.1.

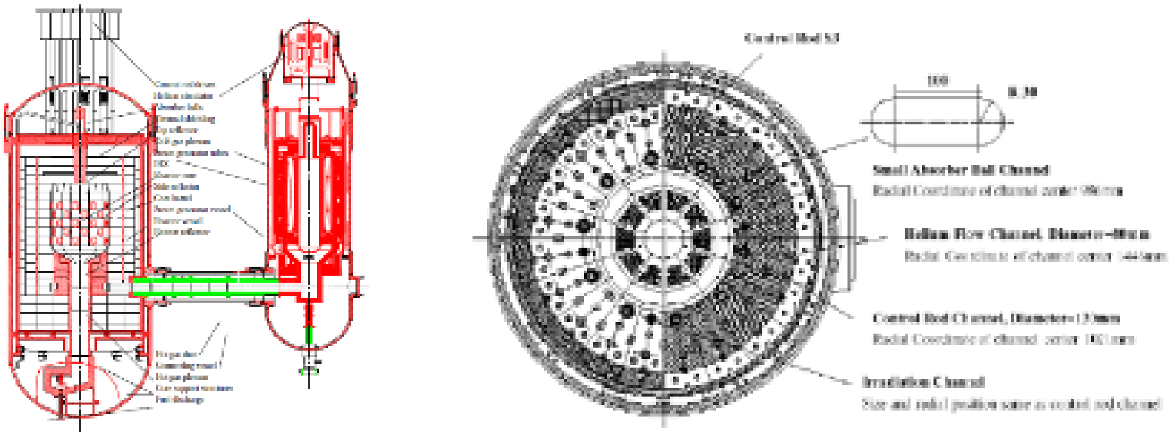

Fig. 2.3: HTR-10 primary system (left) and reactor horizontal cross section (right)

The benchmarks performed here are listed in Table 2.1 and details are provided in [39].

2.3.1 HTR-10 Modeling with Serpent-AGREE

The modeling of the HTR-10 was performed with Serpent-AGREE using the initially critical model of HTR-10 [41]. The initial Serpent model used the same nodalization as a MCNP model previously developed [39][40]. From this model, more comprehensive nodal division was developed for Serpent which was then used as the reference and to generate nodal cross sections for AGREE. Fig. 2.4 shows the nodal division model used in Serpent and AGREE.

Using this nodal division, the Serpent model was generated. In this model, the pebble position is random, which is different from hexagonal-closed-packing in the MCNP model. All control rods are modelled explicitly. Nodal cross sections are generated base on the nodal division from Fig. 2.5. The Serpent model for initially critical HTR-10 core is shown in Fig. 2.6.

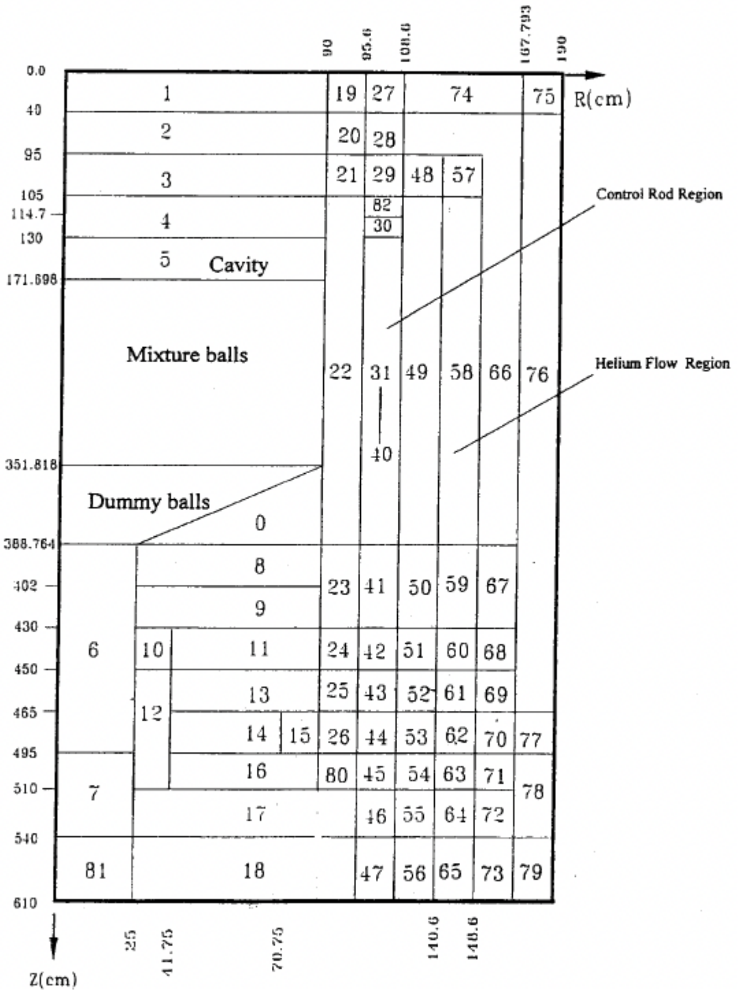

Fig. 2.4: MCNP model for initially critical HTR-10 core

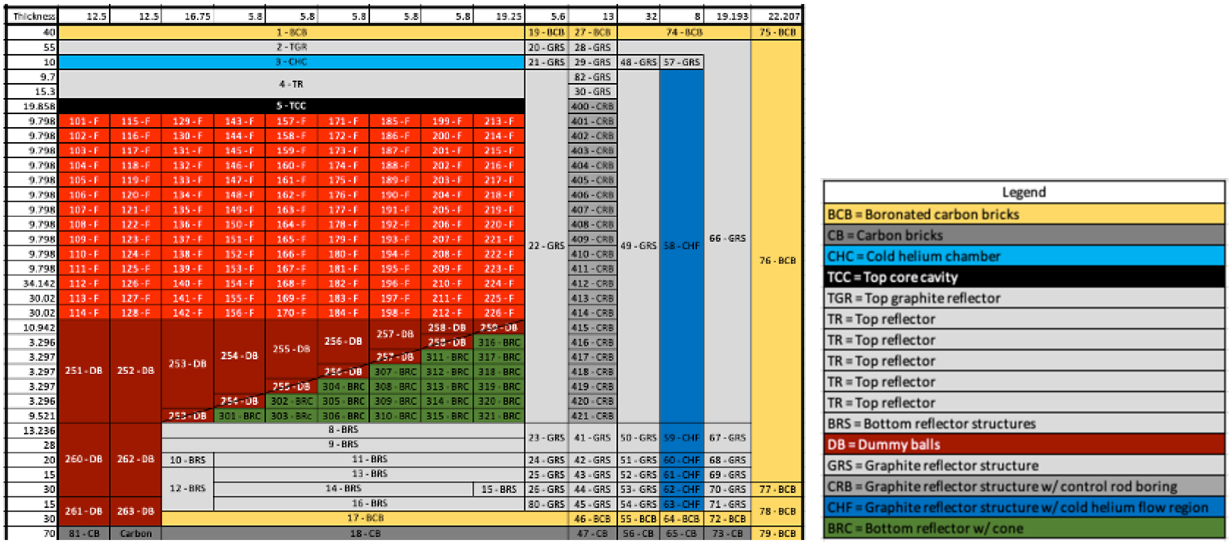

Legend
BCB = Boronated carbon bricks
CB = Carbon bricks
CHC = Cold helium chamber
TCC = Top core cavity
TGR = Top graphite reflector
TR = Top reflector
TR = Top reflector
TR = Top reflector
TR = Top reflector
TR = Top reflector
BRS = Bottom reflector structures
DB = Dummy balls
GRS = Graphite reflector structure
CRB = Graphite reflector structure w/ control rod boring
CHF = Graphite reflector structure w/ cold helium flow region
BRC = Bottom reflector w/ cone

Fig. 2.5: Nodal division of the HTR-10 core for Serpent-AGREE model

Table 2.1: The HTR-10 benchmarks

Number	Name	Description
B1	Initial Criticality Benchmark	Loading height for initial core for first criticality ($k_{eff} = 1$) with no CR insertion. This problem involved calculating the amount of loading (given in loading height) for the first core criticality without control rods being inserted.
B4	Control Rod Worth	This problem includes calculating the reactivity worth of the ten fully inserted control rods (B41) under helium atmosphere and core temperature of $20°\mathrm{C}$ for a loading height of 123.86 cm and 17000 pebbles, and the differential worth of one control rod (B42), the other rods are in withdrawn position.
B2	Temperature Coefficient Benchmark	This problem involved calculating the effective multiplication factor of the full core at $20°\mathrm{C}$, $120°\mathrm{C}$, and $250°\mathrm{C}$ without any control rods being inserted.
B3	Control Rod Worths for full core	This problem involved calculating the reactivity worth of ten fully inserted control rods and one fully inserted control rod for the full core.

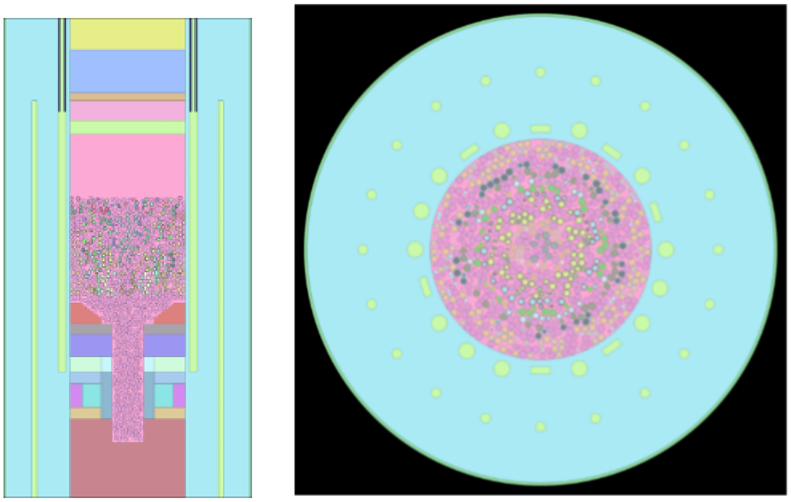

Fig. 2.6: Serpent model for initially critical HTR-10 core

2.3.2 HTR-10 Benchmarks

The detailed specifications of the four HTR-10 benchmark cases listed in Table 2.1 are presented in this section. Benchmark B1 and B4 are based on the initial critical core and measured experimental data, while benchmark B2 and B3 are based on the fully loaded initial core and code to code comparison.

The following modeling discretization and conditions were used for the initial validation of AGREE-XE using HTR-10:

1. Initial Critical Core Case: All 20 channels have their own cross sections, 40 azimuthal cross sections generated for Ring 10 of the core region. There are 924 cross section sets in total for this model. Stream option 3 is applied without DDDC. Both 8-group cross section and 14-group cross section are used. Both cross sections are generated with 200,000 neutrons per cycle.

2. Control Rod Worth Case: All 20 channels have their own cross sections, 40 azimuthal cross sections generated for Ring 10 of the core region.

3. Temperature Coefficient Case: All 20 channels have their own cross sections, 40 azimuthal cross sections generated for Ring 10 of the core region.

2.3.2.1 Benchmark B1: Initial Critical Core

Fig. 2.7 shows the AGREE model of the initially critical HTR-10 core.

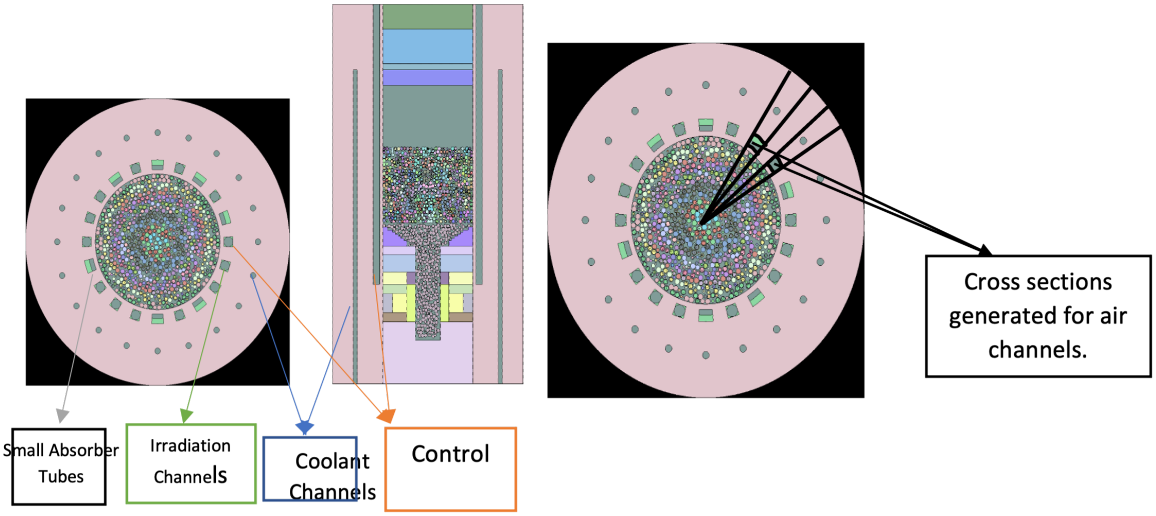

Fig. 2.7: AGREE model for initially critical HTR-10 core

The results of HTR-10 V&V (Verification and Validation) consist of eigenvalue comparison for the minimum critical core between continuous energy Serpent, and AGREE with Serpent nodal cross sections results for initially critical core are shown in Table 2.2. Linear interpolation of the above results in a critical height of 124.33 cm predicted by Serpent, which is 1.37 cm or 1.03% higher than the height found experimentally, and a critical height of 122.93 cm predicted by AGREE, which is 0.13 cm or 0.11% lower than the experimental height. The Institute of Nuclear Energy Technology (INET) computed the height of initial criticality with MCNP and VSOP, and they determined the critical loading height to be 122.87 cm and 122.56 cm, respectively, so the results found by Serpent and AGREE have similar accuracy to results found by other benchmark participants [39].

Table 2.2: k_{eff} at various loading heights

Height [cm]	Serpent k_{eff} (std = 10 pcm)	AGREE k_{eff} (8-Group, 360°)
112.06	0.95949	0.96305
118.06	0.98003	0.97770
124.06	0.99921	1.00519
130.06	1.01694	1.02358
136.06	1.03328	1.04333

2.3.2.2 Benchmark B4: Single Rod Withdrawal Experiment

This case involved the following simulation:

- One rod inserted, all other rods withdrawn
- Helium atmosphere
- 20 °C (293.15 K)
- Loading height of 126 cm
- Worth calculated when lower end of rod is at axial positions: 394.2 cm, 383.618 cm, 334.918 cm, 331.318 cm, 282.618 cm, 279.018 cm, and 230.318 cm

The configuration of the control rods is shown in Fig. 2.8. Experimental results indicate that the integral worth of one typical rod in helium atmosphere is 1.4693% .

For the reactivity worth of the ten control rods for the initial critical core (B41), the results and the comparison to the reference are listed in Table 2.3. According to [39], the experimental rod worth was 1469 pcm, which means the Serpent result in Table 2.3 is 211 pcm off the experimental data. It also shows that the agreement between Serpent and AGREE worths is very strong.

For the differential rod worth of one control rod case (B42), Fig. 2.9 shows the results of the simulation reported by China in [39] with comparisons to experimental data.

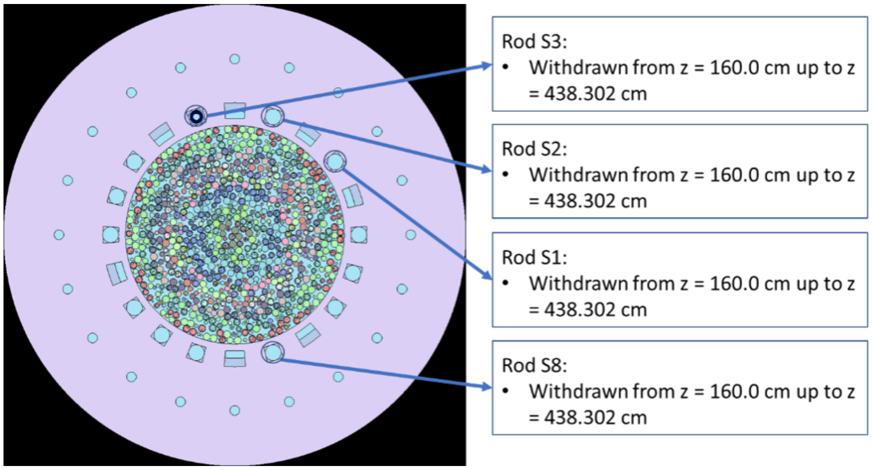

Rod S3:
- Withdrawn from z = 160.0 cm up to z = 438.302 cm

Rod S2:
- Withdrawn from z = 160.0 cm up to z = 438.302 cm

Rod S1:
- Withdrawn from z = 160.0 cm up to z = 438.302 cm

Rod S8:
- Withdrawn from z = 160.0 cm up to z = 438.302 cm

Fig. 2.8: The configuration of the control rods for Benchmark B4

Table 2.3: HTR-10 benchmark B41 rod worth results

Case	ARO k_{eff}	ARI k_{eff}	Worth [pcm]	Difference from experimental [pcm]
Serpent	0.996800	0.981000	1616	146
AGREE 4G	1.012370	0.995934	1630	161
AGREE 8G	1.002424	0.986122	1649	180
AGREE 14G	1.001299	0.984953	1657	188

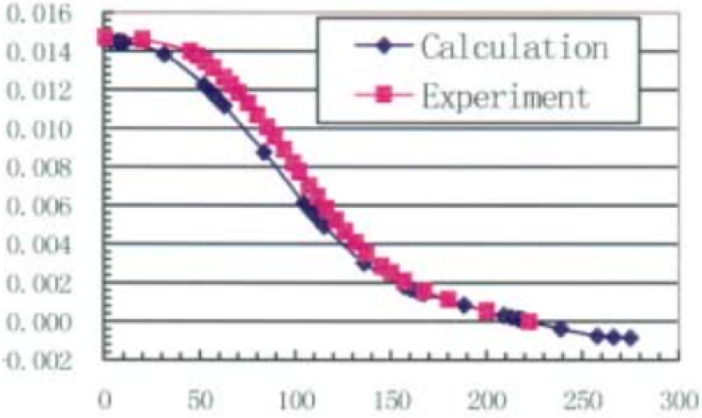

Fig. 2.9: Control rod worth curve for a single rod in Benchmark B4

2.3.2.3 Test B2: Temperature Coefficient Benchmark

For this case, the k_{eff} at different temperatures was calculated for the HTR-10 full core. Based on the TECDOC [39], the final conditions of the full core are

- Helium atmosphere
- Average loading height of 180.12 cm
- All control rods in fully withdrawn position
- k_{eff} calculated for 3 temperatures: 20°C, 120°C and 250°C
- Assumed isothermal temperature coefficient (all materials at same temperature)

Since no experimental results were provided for this case, all results are compared to the reference VSOP results. Reference MCNP results were not provided. The results from this problem found by Serpent and AGREE along with the VSOP reference results are shown in Table 2.4 below.

Table 2.4: HTR-10 full core k_{eff} at various temperatures

Case	k_{eff} at 20°C	k_{eff} at 120°C	k_{eff} at 250°C	Average difference from Serpent [pcm]	Average difference from INET VSOP [pcm]
Serpent	1.138230	1.127120	1.109200	N/A	140
Reference VSOP	1.135779	1.126158	1.111115	N/A	N/A
AGREE 4G	1.156645	1.144379	1.125527	1348	1385
AGREE 8G	1.145529	1.136234	1.117798	655	692
AGREE 14G	1.146983	1.135400	1.116970	648	685

As expected, as the number of energy groups increases, the agreement between the k_{eff} calculated by Serpent and AGREE improves as well. The minimum average difference between Serpent and AGREE is 648 pcm, and this occurs for the 14g case. Additionally, for more energy groups, the agreement between the reference VSOP results and the AGREE results also improves; for 14g, the average k_{eff} difference between AGREE and the reference VSOP results is 685 pcm compared to 1385 pcm for the 4g case. However, the Serpent k_{eff} values are much closer to the reference VSOP k_{eff} values than all of the AGREE results.

2.3.2.4 Test B3: Full Core Control Rod Worth Results

For this case, the control rod worth was calculated for the HTR-10 full core. The core conditions for this case are

- Helium atmosphere
- Loading height of 180.12 cm

- 27,000 pebbles in the core region

The results are listed in Table 2.5. According to [39], the Chinese MCNP result was 1343 pcm using nuclear data library ENDF/B-V. It shows the results in Table 2.5 agree well with the Chinese MCNP result. It also shows that the agreement between Serpent and AGREE worths is very strong.

Table 2.5: HTR-10 benchmark B3 rod worth results

Case	ARO k_{eff}	ARI k_{eff}	Worth [pcm]	Difference from experimental [pcm]
Serpent	1.136410	1.120300	1265	78
AGREE 4G	1.155052	1.138383	1268	75
AGREE 8G	1.146411	1.129690	1291	52
AGREE 14G	1.145377	1.128738	1278	56

The agreement between the worths determined by Serpent and AGREE and the reference worth is much better for the full core than for the initial core; the maximum difference in worths is only 78 pcm, and the 14g, 360° AGREE case only has a difference of 56 pcm from the reference worth. Since the main difference between the geometry in this case and the initial core is the core loading height, and therefore the size of the helium cavity above the fuel region, this result suggests that such a large cavity in the initial core could be causing calculation errors. However, it should be noted that the difference between the k_{eff} calculated by Serpent and AGREE is higher than for the initial core case, suggesting that cross section generation is not most optimized for the full core case.

2.4 Validation of Methods: The gFHR Benchmark

2.4.1 gFHR Modeling with Serpent-AGREE

The gFHR benchmark model developed by KAIROS is a cylindrical core surrounded by graphite reflectors at the top, bottom and all sides. The core is contained in the core barrel. There is a downcomer between the core barrel and the reactor vessel. The active core is randomly packed with fuel pebbles and the packing fraction is 60% of the volume. The radius of the pebbles is 2.0 cm, including a central graphite core of 1.38 cm in radius, a fuel annulus of 0.42 cm in thickness and a shell of 0.20 cm in thickness.There are 9022 TRISO particles dispersed randomly in the fuel annulus per pebble. The design of the TRISOs is the same as in the AGR-5/6/7 program [42]. The outer radius of the TRISO particles is 0.0425 cm. The fuel is made of 19.55 wt% enriched $UC_{1.5}O_{0.5}$. The coolant is flibe (Li_2BeF_4), in which the ^{7}Li is enriched at 99.995%.

The more detailed gFHR model specifications including the geometrical dimensions and material compositions can be found in the benchmark publication [43].

The gFHR core is discretized in to 19 radial regions and 28 axial regions for homogenized cross section generation, in which case the size of homogenized region is about 3∼4 times of neutron transport mean free path (λ_{tr}). This is depicted by Fig. 2.10. The 19 radial regions include 12 fuel regions, 6 reflector regions and 1 region for the barrel, downcomer and vessel. The 28 axial regions include 4 top reflector regions, 4 bottom reflector regions and 20 fuel regions.

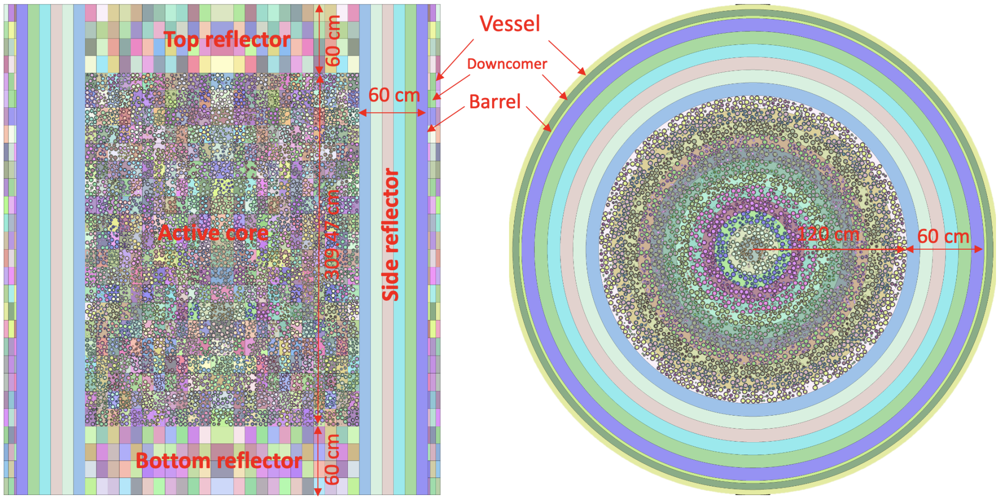

Figure 2.10: Axial (left) and radial (right) cross section views of the gFHR model

2.4.2 gFHR Benchmarks

2.4.2.1 Serpent Results

In the benchmark, the gFHR core is discretized into 4 radial × 10 axial zones for burnup calculation. The fuel compositions at equilibrium are given for the 40 zones [44]. The benchmark reference eigenvalue [43] of the equilibrium core was calculated using Serpent 2 for randomized pebble-bed with ENDF/B-VII.I library (with TSL library off). In this paper, OpenMC code [21] is employed to generate the random positions for the TRISOs and the pebbles. The eigenvalue result is shown in Table 2.6. When turning off the thermal scattering library (TSL), the $k_{\text{eff}} = 1.01272$, which agrees well with the benchmark reference value. The difference caused by the TSL library is 158 pcm in our Serpent 2 calculation, which means that the effect of thermal scattering is not negligible.

Table 2.6: Eigenvalue result of the gFHR equilibrium core

Benchmark (ref.)	Serpent 2 TSL off k_{eff} (Diff)	Serpent 2 TSL on k_{eff} (Diff)
1.01443±0.000233	1.01272±0.000049 (171 pcm)	1.01114±0.000047 (329 pcm)

2.4.2.2 AGREE Results

An AGREE model was developed using the cross sections generated by Serpent 2. The reference temperature of all other materials is set to 900 K. All five of the few-group structures were tested. To assure that the cross sections achieve the same level of statistics for the different group structures, the number of histories used for the Monte Carlo simulation are set to be proportional to G^2, where G is the number of energy groups. The results are shown in Table 2.7. As shown in the Table 2.7, the 7-group, 14-group(b) and 23-group structures achieve good agreement between Serpent 2 and AGREE.

Table 2.7: Eigenvalue comparison between Serpent 2 and AGREE

Group	Serpent 2 k_{eff}	AGREE k_{eff}	Difference (pcm)
2	1.01309±0.000290	1.02150	+841
4(a)	1.01316±0.000140	1.02023	+707
7	1.01294±0.000083	1.01560	+266
14(b)	1.01303±0.000042	1.01718	+415
23	1.01304±0.000026	1.01742	+437

2.5 Summary

In this chapter, the Monte Carlo-deterministic hybrid method is introduced to overcome the difficulties in modeling the HTR reactors due to their double-heterogeneity feature in the core and fuel structure. The Monte Carlo code Serpent 2 is employed to generate homogenized cross sections, which are then used in deterministic code AGREE for neutronics simulations based on the neutron diffusion equation.

The hybrid methods are applied to HTR-10 benchmark problems and the gFHR benchmark problems for validation purpose. Various energy group structures are tested and it shows that when increasing the number of energy groups, the agreement between the AGREE results and Serpent results can be improved.

CHAPTER 3

Development of Uncertainty Analysis Methods and Application to the HTR

The uncertainty estimation of the predicted reactor performance parameters has important implications in determining the reactor design margins and evaluating the overall plant safety performance. The uncertainties are inevitably present because of the inaccuracies in the evaluated nuclear data due to the measurement processes and the different corrections made to the microscopic cross sections. In assessing design penalties and establishing a nuclear data improvement program, it is necessary to characterize uncertainties in the nuclear data set. As noted in the introduction, the research here was to quantify the additional uncertainty that is introduced in the core calculation by the Monte Carlo method used in the Serpent/AGREE core analysis methodology.

The methodology for computing the uncertainties of the performance parameters is discussed in this Chapter. Statistical uncertainty data is generated by the Serpent Monte Carlo code. The uncertainties of the safety performance parameters for the gFHR is discussed in Chapter 4, and the proposed methods to minimize the uncertainty of the Monte Carlo data is presented in Chapter 5.

3.1 Comparison and Assessment of UQ Methods for Monte Carlo Cross Sections

A comparison and assessment of two different methods for quantifying the uncertainty in Monte Carlo cross sections was performed using case B1 of the HTR-10 Benchmark.

3.1.1 Energy Group Structure

Five different few-group structures were tested for Monte Carlo cross section generation and were used for multi-group neutron diffusion simulation. For all the five cases, a same number of 200,000 particles and 500/100 active/inactive cycles were run during the few-group cross section generation. The lower boundaries of the five few-group structures are listed in Table 3.2. The k_{eff} results obtained from Serpent and AGREE are listed in Table 3.1. It shows that when increasing the number of energy groups, the difference between Serpent and AGREE k_{eff} becomes smaller.

Table 3.1: HTR-10 benchmark B1 k_{eff} results for various group structures

Group	Serpent	AGREE	diff [pcm]	AGREE run time [s]
2G	0.99941±0.00010	1.02980	3039	472
4G	0.99908±0.00010	1.01499	1591	860
8G	0.99921±0.00010	1.00519	598	5538
14G	0.99901±0.00011	1.00396	495	18230
23G	0.99914±0.00010	1.00061	147	45118

Fig. 3.1 shows the five few-group structures superimposed on the plot of microscopic cross sections. In Fig. 3.1, the graphite elastic scattering cross section, the U-235 fission cross section and the U-238 capture cross section are plotted, which are the three significant cross sections in a HTR reactor. It shows that when the number of energy groups is increased, a better resolution in the thermal energy range can be achieved.

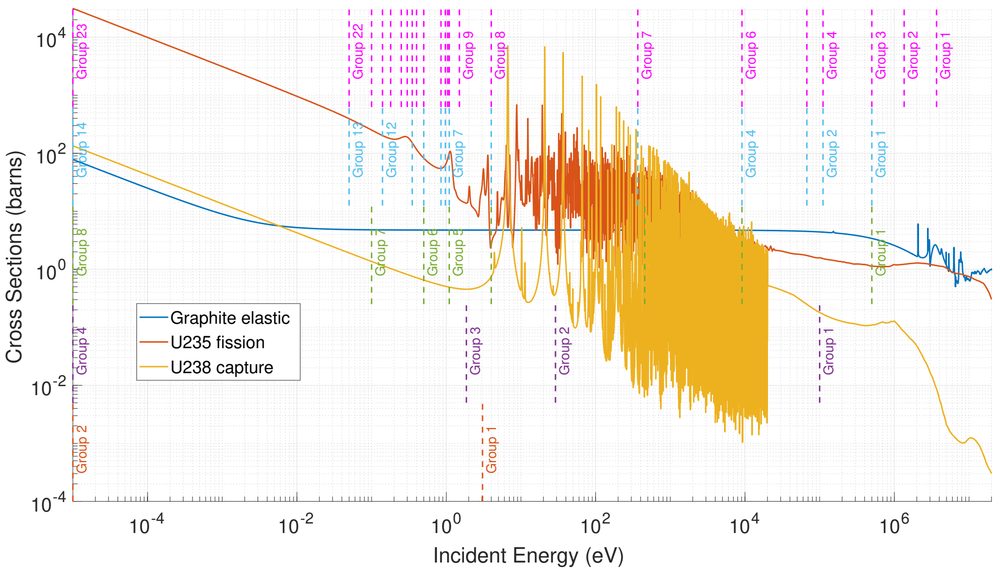

Fig. 3.1: Few group structures for HTR-10 benchmarks

Table 3.2: Lower boundaries of the five few-group structures used in HTR-10 benchmark B1 homogenized cross section generation (unit: eV)

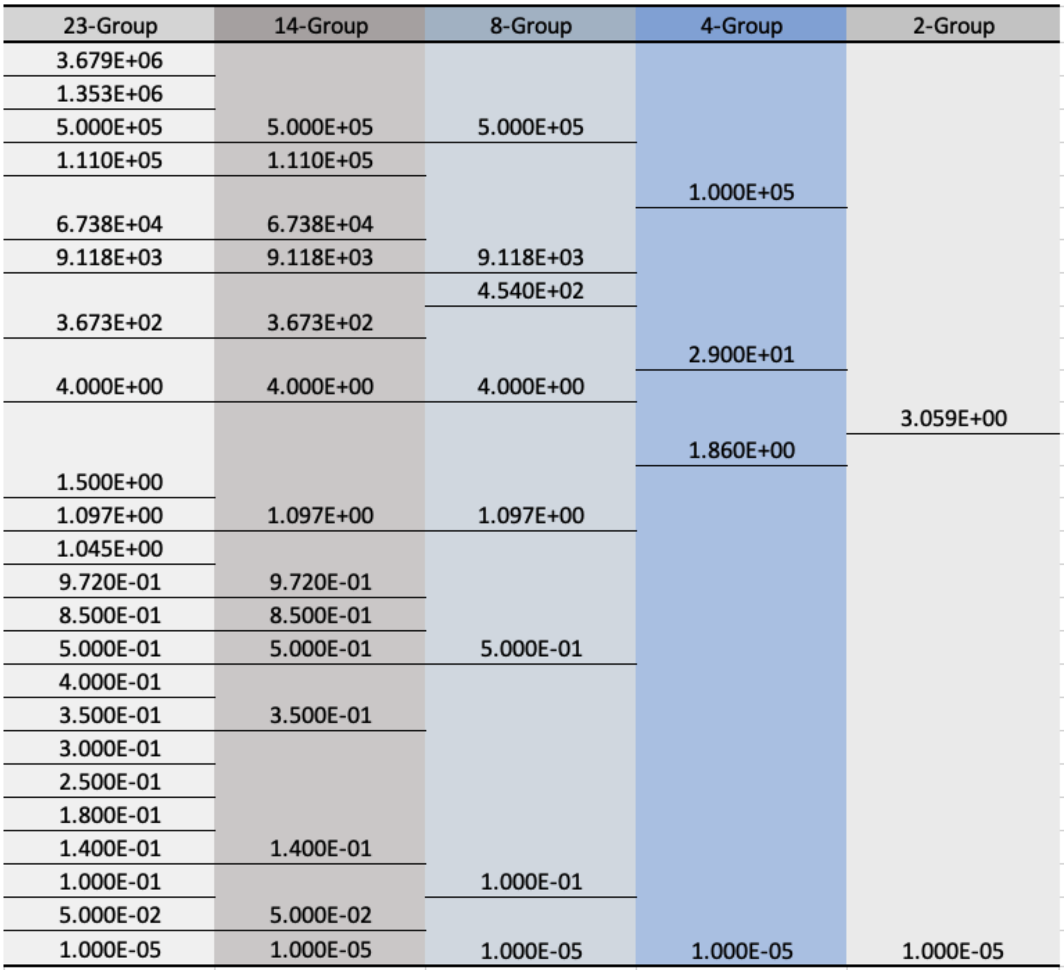

23-Group	14-Group	8-Group	4-Group	2-Group
3.679E+06				
1.353E+06				
5.000E+05	5.000E+05	5.000E+05		
1.110E+05	1.110E+05			
			1.000E+05	
6.738E+04	6.738E+04			
9.118E+03	9.118E+03	9.118E+03		
		4.540E+02		
3.673E+02	3.673E+02			
			2.900E+01	
4.000E+00	4.000E+00	4.000E+00		
				3.059E+00
			1.860E+00	
1.500E+00				
1.097E+00	1.097E+00	1.097E+00		
1.045E+00				
9.720E-01	9.720E-01			
8.500E-01	8.500E-01			
5.000E-01	5.000E-01	5.000E-01		
4.000E-01				
3.500E-01	3.500E-01			
3.000E-01				
2.500E-01				
1.800E-01				
1.400E-01	1.400E-01			
1.000E-01		1.000E-01		
5.000E-02	5.000E-02			
1.000E-05	1.000E-05	1.000E-05	1.000E-05	1.000E-05

3.1.2 MC Statistical Error of Few-group Cross Section

The standard deviation of the Monte Carlo code generated few-group cross section is the statistical uncertainty of the few-group cross section data in AGREE code. Fig. 3.2 shows the average uncertainty of the fission cross sections in 60 fuel regions for different energy group structures. It shows that when increasing the number of groups, the uncertainty of the cross section becomes larger. Besides, the uncertainty in a smaller energy interval is usually larger than the uncertainty in a larger energy interval. For the uncertainty of other cross sections, such as absorption cross section and scattering cross section, similar behaviours can be observed. Therefore, to achieve the same level of uncertainty for a energy group structure containing more groups, more Monte Carlo simulation histories are required.

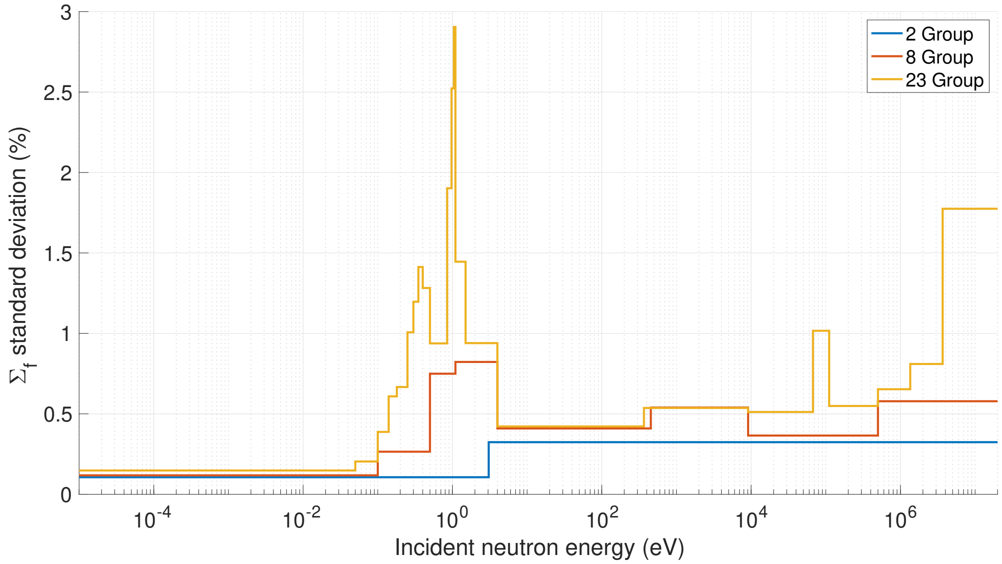

Fig. 3.2: Averaged uncertainty of Σ_f for 2-group, 8-group and 23-group

In the Monte Carlo simulation, the standard deviation of a statistical quantity is proportional to $\frac{1}{\sqrt{N}}$, where N is the number of simulation histories. Fig. 3.3 shows the averaged standard deviation of the 23-group fission cross section when different number of neutrons were simulated to generate the cross sections. For all the cases, a same number of 500/100 active/inactive cycles were run. So the total number of Monte Carlo simulation histories is proportional to the number of neutrons. The $\mathcal{L}$-1 and $\mathcal{L}$-2 norms of Σ_f uncertainties are plotted in Fig. 3.4. The x-axis y-axis in Fig. 3.4 are in logarithmic scale, and it clearly shows that the uncertainty of Σ_f is proportional to $\frac{1}{\sqrt{N}}$ as predicted.

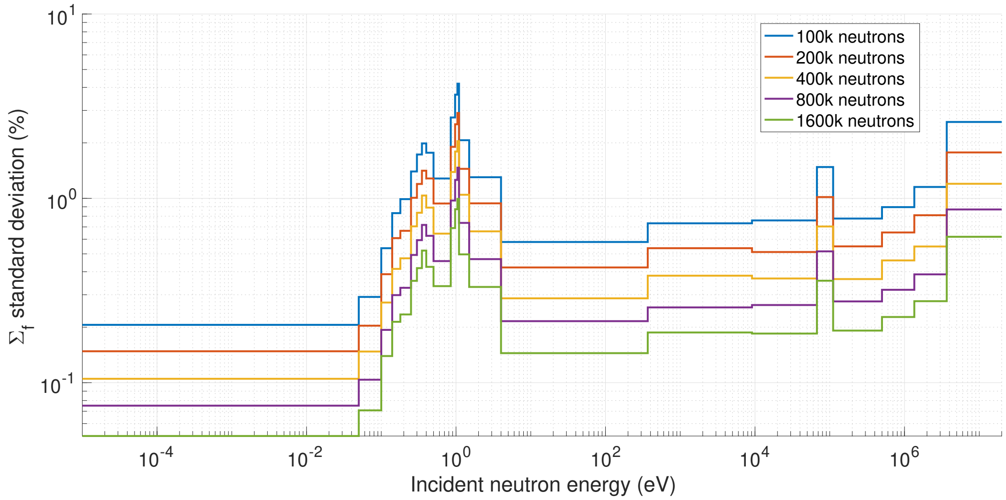

Fig. 3.3: Averaged uncertainty of Σ_f for 23-group with various number of neutrons

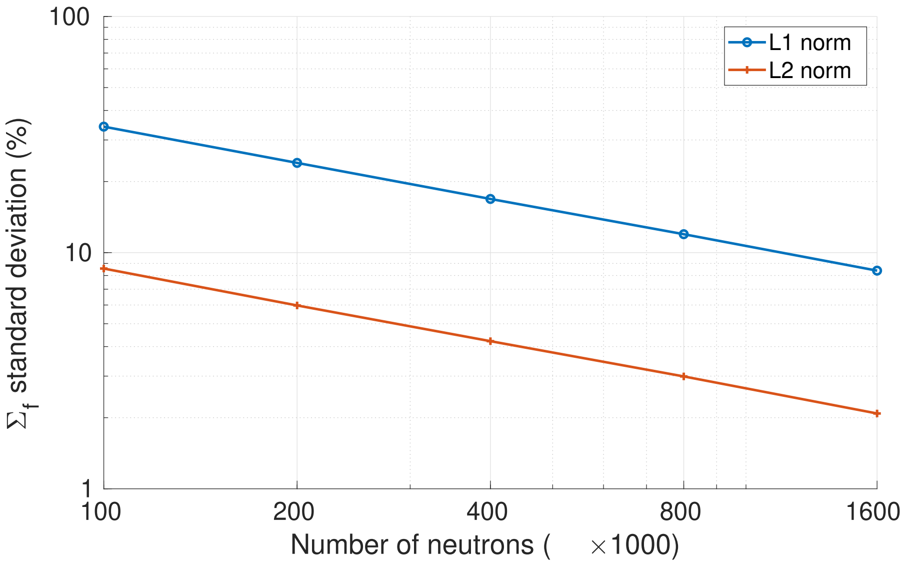

Fig. 3.4: $\mathcal{L}$-1 and $\mathcal{L}$-2 norms of Σ_f uncertainty for 23-group with various number of neutrons

3.2 Analytical and Stochastic Uncertainty Analysis Methods

3.2.1 Analytical Methods: Conventional Perturbation Theory

Conventional perturbation theory (CPT) provides a practical method for determining the uncertainties of computed performance parameters. This section will briefly outline the CPT formularization and a practical solution scheme that was used in the AGREE code.

3.2.1.1 CPT Derivation

The fundamental mode neutron diffusion equation with multi-group approximation for a steady state system is

$$B\phi = 0 \quad , \tag{3.1}$$

where

$$\begin{aligned} B\phi &= M\phi - \lambda F\phi \\ &= \nabla \cdot D^g \nabla \phi^g - \Sigma_r^g \phi^g + \sum_{g' \neq g} \Sigma_s^{g' \to g} \phi^{g'} + \lambda \chi^g \sum_{g'} \nu \Sigma_f^{g'} \phi^{g'} \quad . \end{aligned} \tag{3.2}$$

The fundamental mode adjoint flux is calculated from the equation

$$B^* \phi^* = 0 \quad , \tag{3.3}$$

where B^* is the adjoint operator of B. The full expression of B^* is

$$\begin{aligned} B^*\phi^* &= M^*\phi^* - \lambda^* F^* \phi^* \\ &= \nabla \cdot D^g \nabla \phi^{*,g} - \Sigma_r^g \phi^{*,g} + \sum_{g' \neq g} \Sigma_s^{g \to g'} \phi^{*,g'} + \lambda^* \nu \Sigma_f^g \sum_{g'} \chi^{g'} \phi^{*,g'} \quad , \end{aligned} \tag{3.4}$$

where ϕ^* in Eq. (3.3) and Eq. (3.4) is called adjoint flux, which represents the “importance” of neutrons in the reactor.

It can be shown that $\lambda = \lambda^*$, which are the eigenvalues of the neutron diffusion equation and the adjoint equation. The sensitivity and uncertainty of the eigenvalue λ can be determined using perturbation methods.

First, consider the unperturbed neutron diffusion equation and its adjoint equation

$$M_0\phi_0 = \lambda_0 F_0\phi_0 \quad ; \tag{3.5}$$

$$M_0^*\phi_0^* = \lambda_0 F_0^*\phi_0^* \quad . \tag{3.6}$$

And the neutron diffusion equation for the perturbed system is

$$M\phi = \lambda F\phi \quad . \tag{3.7}$$

Then multiply Eq. (3.6) and Eq. (3.7) by ϕ and ϕ_0^*, respectively, prior to the inner product (or integration in continuous energy case). This gives

$$\langle \phi, M_0^*\phi_0^* \rangle = \lambda_0 \langle \phi, F_0^*\phi_0^* \rangle \quad ; \tag{3.8}$$

$$\langle \phi_0^*, M\phi \rangle = \lambda \langle \phi_0^*, F\phi \rangle \quad , \tag{3.9}$$

where $\langle \cdot, \cdot \rangle$ means inner product operation of the two vectors.

According to the property of adjoint operators, Eq. (3.8) is equivalent to

$$\langle \phi_0^*, M_0\phi \rangle = \lambda_0 \langle \phi_0^*, F_0\phi \rangle \quad . \tag{3.10}$$

Subtracting Eq. (3.9) from Eq. (3.10) and using the relation

$$M = M_0 + \Delta M \quad ; \tag{3.11}$$

$$F = F_0 + \Delta F \quad , \tag{3.12}$$

yields the conventional perturbation formula for the eigenvalue increments:

$$\Delta_\lambda = \lambda - \lambda_0 = \frac{\langle \phi_0^*, (\Delta M - \lambda_0 \Delta F)\phi \rangle}{\langle \phi_0^*, F\phi \rangle} \quad . \tag{3.13}$$

Usually the neutron multiplication factor $k_{\text{eff}} = \frac{1}{\lambda}$ is preferred. So the conventional perturbation formula for the uncertainty of k_{eff} is

$$\Delta_{k_{\text{eff}}} = \frac{\langle \phi_0^*, (\frac{1}{k_{\text{eff},0}}\Delta F - \Delta M)\phi \rangle}{\langle \phi_0^*, F\phi \rangle} \times k_{\text{eff},0}^2 \quad . \tag{3.14}$$

In practice, when the perturbation is very small, the neutron flux of the perturbed system ϕ does not change much compared to the neutron flux of the unperturbed system ϕ_0. Therefore, Eq. 3.14

can be approximately calculated by

$$\Delta_{k_{\text{eff}}} \approx \frac{\langle \phi_0^*, (\frac{1}{k_{\text{eff},0}}\Delta F - \Delta M)\phi_0 \rangle}{\langle \phi_0^*, F\phi_0 \rangle} \times k_{\text{eff},0}^2 \quad . \tag{3.15}$$

With Eq. 3.15, the neutron diffusion equation and its adjoint equation will be solved only for the unperturbed system to obtain ϕ_0 and ϕ_0^*. The operator ΔF and ΔM, which are only related to at most seven terms in a 3-D discretization or five terms in a 2-D discretization, can be obtained without solving the perturbed system (See Appendix D). Since solving the neutron diffusion equation is the dominate computational burden in the AGREE simulation, using Eq. 3.15 rather than Eq. 3.14 can save the run time significantly when computing the $\Delta_{k_{\text{eff}}}$.

3.2.1.2 Calculation Scheme

Based on Eq. (3.15), a calculation scheme for calculating the uncertainty of k_{eff} due to Monte Carlo (MC) cross section uncertainties was implemented using the AGREE code. The calculation scheme is shown in Fig. 3.5.

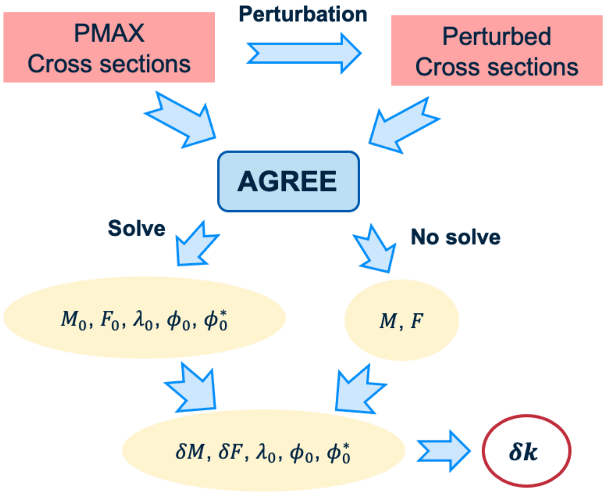

Fig. 3.5: Calculation scheme for calculating the uncertainty of k_{eff} using analytical methods

First, the original unperturbed problem is calculated using AGREE. The unperturbed neutron diffusion operator M_0 and F_0, the eigenvalue λ_0, neutron flux ϕ_0 and adjoint neutron flux ϕ_0^* are obtained during this step.

Second, perturbed the cross section data based on the standard deviation of the MC generated cross section. In this step, the neutron diffusion equation system is set up but not solved, since only the operators M and F are needed.

Based on above two steps, all the components in Eq. (3.15) are obtained. And then the uncertainty of k_{eff} can be calculated.

3.2.2 Stochastic Methods: Random Sampling

The uncertainties of interested parameters due to the uncertainties of the MC generated cross sections can also be determinted by randomly sampling, which is the stochastic methods. This section will outline the solution scheme of stochastic methods and demonstrate the scheme with a simple example problem.

3.2.2.1 Introduction to Dakota Code

Dakota is a toolkit for optimization, uncertainty quantification and model calibration developed by Sandia National Laboratory (SNL). The Dakota toolkit serves as a versatile and extensible interface, facilitating seamless interaction between simulation codes and iterative analysis methods. It encompasses a wide array of algorithms, including gradient and nongradient-based optimization, uncertainty quantification with sampling, reliability, and stochastic expansion techniques, parameter estimation using nonlinear least squares methods, and sensitivity/variance analysis employing design of experiments and parameter study approaches. These capabilities can be used independently or integrated into advanced strategies like surrogate-based optimization, mixed-integer nonlinear programming, and optimization under uncertainty. Embracing an object-oriented design philosophy to abstract essential components, Dakota offers a flexible and adaptable problem-solving environment for analyzing computational models on high-performance computers[45].

3.2.2.2 Calculation Scheme

The stochastic methods based on random sampling is very straightforwad. The calculation scheme is shown in Fig. 3.6.

First, a set of cross section samples are generated by Dakota, assuming that the cross section data follow the normal distribution, i.e.,

$$\Sigma_{x,i,g} \sim \mathcal{N}(\overline{\Sigma}_{x,i,g}, \Delta^2_{\Sigma_{x,i,g}}) \tag{3.16}$$

where x, i, g represents cross section type, homogenized region ID and energy group ID, respectively. $\overline{\Sigma}_{x,i,g}$ and $\Delta_{\Sigma_{x,i,g}}$, both generated by Serpent code, are the nominal value and standard deviation of the cross section $\Sigma_{x,i,g}$, respectively.

Second, a set of AGREE cases are performed based on cross section set generated in the first step. Since the cross section data used for AGREE code are stored in PMAX files, the input

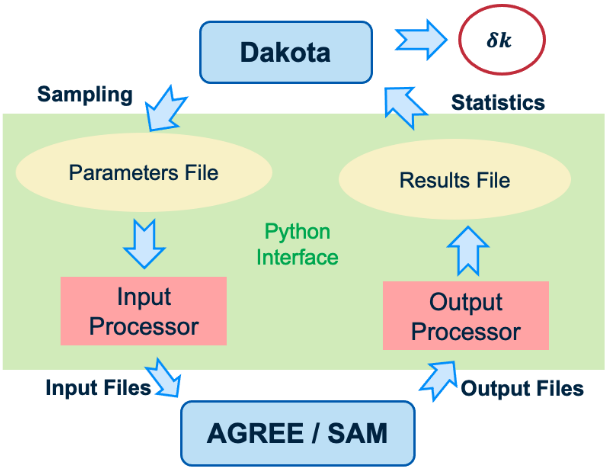

Fig. 3.6: Calculation scheme for calculating the uncertainty of k_{eff} using stochastic methods

processor generates a set of PMAX files and AGREE input files for the set of cross section samples.

Next, the set of AGREE cases is performed and the output processor is used to extract the results of interest which are written in a specific format file to be read by the Dakota code. Dakota fits the set of output parameters in specified distributions, providing the mean values and standard deviations of the output parameters. In this section, the output parameter of interest is the k_{eff} which is assumed to follow a normal distribution

$$k_{\text{eff}} \sim \mathcal{N}(\overline{k}_{\text{eff}}, \Delta^2_{k_{\text{eff}}}) \quad . \tag{3.17}$$

3.3 Results Comparison for a Demonstration Problem

In this section, a simplified gFHR fresh core benchmark model is developed to make code-code validation between the analytical method and the stochastic method.

3.3.1 Description of the Demonstration Problem

An example problem was developed by simplifying the gFHR fresh core benchmark model. The purpose of the problem was to simplify the comparison of the deterministic CPT and stochastic DAKOTA methods for estimating the uncertainty. The geometry of the demonstration problem is shown in Fig. 3.7. The active core region is a cylinder with a radius of $1.2\ \mathrm{m}$ and a height of $3.1\ \mathrm{m}$. The thicknesses of the radial reflector and the axial reflector are both $60\ \mathrm{cm}$. The gFHR fresh core is divided into 3 radial regions and 5 axial regions, among which there are 2 radial fuel regions and 3 axial fuel regions. The enrichment of the fuel in the gFHR fresh core is 19.95%. The compositions of the materials are obtained from [46].

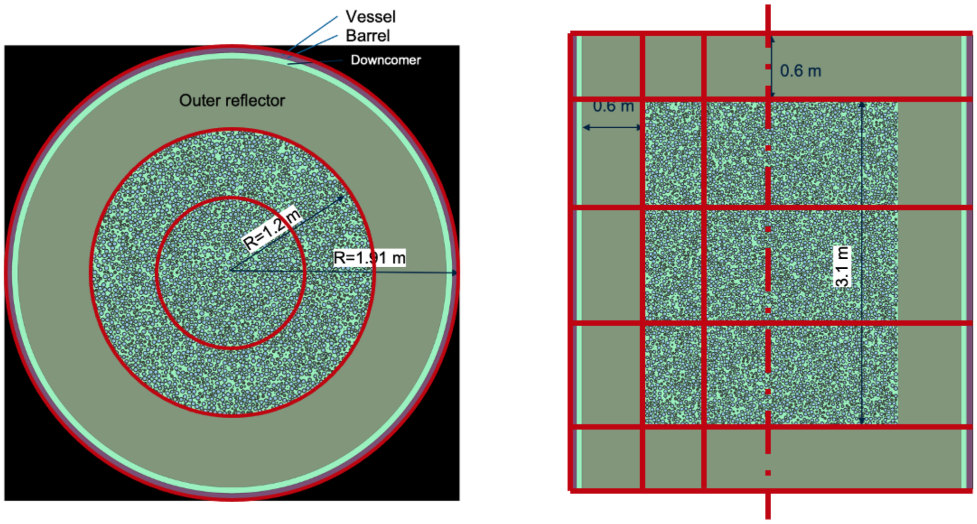

Fig. 3.7: Serpent geometry model for the simplified gFHR fresh core

Homogenized cross section data were generated for the 3×5 regions using Serpent 2 Monte Carlo code. 100,000 neutrons were simulated for 50 inactive cycles and 100 active cycles. Five few-group structures were used to generate multi-group cross sections. The lower boundaries of the five few-group structures are listed in Table 3.3.

The few-group cross sections generated by Serpent 2 were used in the AGREE code. The coarse mesh for the AGREE neutron diffusion model is shown in Fig. 3.8.

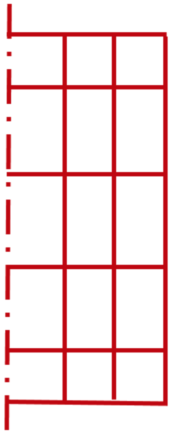

Fig. 3.8: AGREE geometry model for the simplified gFHR fresh core

The k_{eff} results calculated by Serpent and AGREE are listed in Table 3.4. It shows that when increasing the number of energy groups from 2 to 23, the difference between Serpent and AGREE

Table 3.3: Lower boundaries of the five few-group structures used in gFHR homogenized cross section generation (unit: eV)

23	14	7	4	2
3.679E+06				
1.353E+06			1.353E+06	
5.000E+05	5.000E+05	5.000E+05		
1.110E+05	1.110E+05			
6.738E+04	6.738E+04			
9.118E+03	9.118E+03	9.118E+03	9.118E+03	
3.673E+02	3.673E+02			
4.000E+00	4.000E+00	4.000E+00		3.059E+00
1.500E+00				
1.097E+00	1.097E+00	1.097E+00		
1.045E+00				
9.720E-01	9.720E-01			
8.500E-01	8.500E-01		8.500E-01	
5.000E-01	5.000E-01	5.000E-01		
4.000E-01				
3.500E-01	3.500E-01			
3.000E-01				
2.500E-01				
1.800E-01				
1.400E-01	1.400E-01			
1.000E-01		1.000E-01		
5.000E-02	5.000E-02			
1.000E-05	1.000E-05	1.000E-05	1.000E-05	1.000E-05

k_{eff} decreases from about 1000 pcm to about 200 pcm, which shows the similar behavior to the results of HTR-10 benchmark B1 (Table 3.2).

Table 3.4: Simplified gFHR k_{eff} results for various group structures

Group	Serpent	AGREE	diff [pcm]
2G	1.31416±0.00019	1.32364	948
4G	1.31392±0.00020	1.32394	1002
7G	1.31377±0.00019	1.31779	402
14G	1.31418±0.00020	1.31727	495
23G	1.31321±0.00019	1.31512	191

3.3.2 Correlations between the Cross Section Data

In the two methods developed in Section 3.2, the cross sections are assumed to be independent to each other. All the cross section data are perturbed independently and thus the total uncertainty of k_{eff} is assumed to be the $\mathcal{L}$-2 norm of all the contributions. However, the independence of the cross section data is unknown since the covariances between the cross section data are not reported in Serpent's results. Nevertheless, the uncertainty of k_{eff} can be bounded by the $\mathcal{L}$-1 norm of all the contributions (See Appendix B).

However, the homogenized cross sections generated from Monte Carlo code are generally correlated. Because the change of a certain cross section Σ_x may affect the flux distribution that used to collapse another cross section Σ_y, the cross section Σ_x and Σ_y are correlated through the flux distribution. Usually, the correlation between two cross sections in the same region is strong, while the correlation between two cross sections in different regions is weak. Based on this, a "region independent estimation" of the k_{eff} uncertainty can be proposed as:

$$\Delta_{k_{\text{eff}}} \leqslant \sqrt{\sum_{i}^{N_r} \left(\sum_{x,g} \Delta_{k_{\text{eff}}}^{\Sigma_{x,i}^{g}} \right)^2} \quad . \tag{3.18}$$

Table 3.5 summarizes the three estimations proposed above. For many cases, the correlations between the cross sections are weak and the cross section data can be treated as independent variables. In this research, the $\mathcal{L}$-2 norm estimation will be applied for the uncertainty propagation results of most cases.

Table 3.5: Three estimations of the uncertainty of k_{eff}

Estimation	Assumption
$\mathcal{L}$-1 norm	All cross sections are strongly correlated
Region independent	Cross sections in the same region are strongly correlated
$\mathcal{L}$-2 norm	Correlations between all cross sections are very weak

3.3.3 Comparison of the $\Delta_{k_{\text{eff}}}$ Results for the UQ Methods

Using the analytical and stochastic UQ analysis methods and the calculation schemes discussed in Section 3.2, the uncertainty of k_{eff} from AGREE was obtained using a deterministic CPT and a stochastic method. The contributions from fission spectrum (χ), fission cross section ($\nu\Sigma_f$), transport cross section (Σ_{tr}), absorption cross sections were considered when calculating the uncertainty of k_{eff} . The results for different group structures are listed in Table 3.6. All the three estimations of the uncertainty are provided.

Table 3.6: The uncertainty of k_{eff} contributed from MC cross section uncertainties results obtained by CPT analytical methods and by Dakota stochastic methods

Group	AGREE k_{eff}	CPT $\Delta_{k_{\text{eff}}}$ (pcm)			Dakota $\Delta_{k_{\text{eff}}}$ (pcm)		
		L-2	L-1	Region-indep.	L-2	L-1	Region-indep.
2G	1.32364	49.0	246.8	102.8	47.5	221.5	92.2
4G	1.32394	60.2	391.1	161.0	61.0	394.6	159.9
7G	1.31779	60.5	444.5	187.4	61.0	417.4	175.3
14G	1.31727	68.0	596.1	254.3	67.4	588.4	248.4
23G	1.31512	61.1	755.6	308.2	64.0	777.2	319.3

By comparing the $\Delta_{k_{\text{eff}}}$ obtained from CPT and Dakota, it can be observed that the differences between them are minimal, which demonstrates good agreement between the analytical and stochastic methods.

The Monte Carlo standard deviations of k_{eff} reported by Serpent are around 20 pcm, which is about 1/3 of the $\Delta_{k_{\text{eff}}}$ calculated by CPT and Dakota ($\mathcal{L}$-2 norm). This is because the Monte Carlo code appears to underestimate the uncertainty of k_{eff} .

To study the contributions to the total $\Delta_{k_{\text{eff}}}$ from each individual cross section data, the the contributions were estracted for each core region. Fig. 3.9 to Fig. 3.13 illustrate the contributions from cross section data errors of each region and each energy group to the total $\Delta_{k_{\text{eff}}}$.

The principal data presented in the figures is summarized in Table 3.7. It can be observed that the main contribution to $\Delta_{k_{\text{eff}}}$ comes from $\Delta_{\nu\Sigma_f}$ and $\Delta_{\Sigma_{ab}}$. The contribution from Δ_{χ} and $\Delta_{\Sigma_{tr}}$ is negligible. The contribution from Δ_{Σ_s} is generally small.

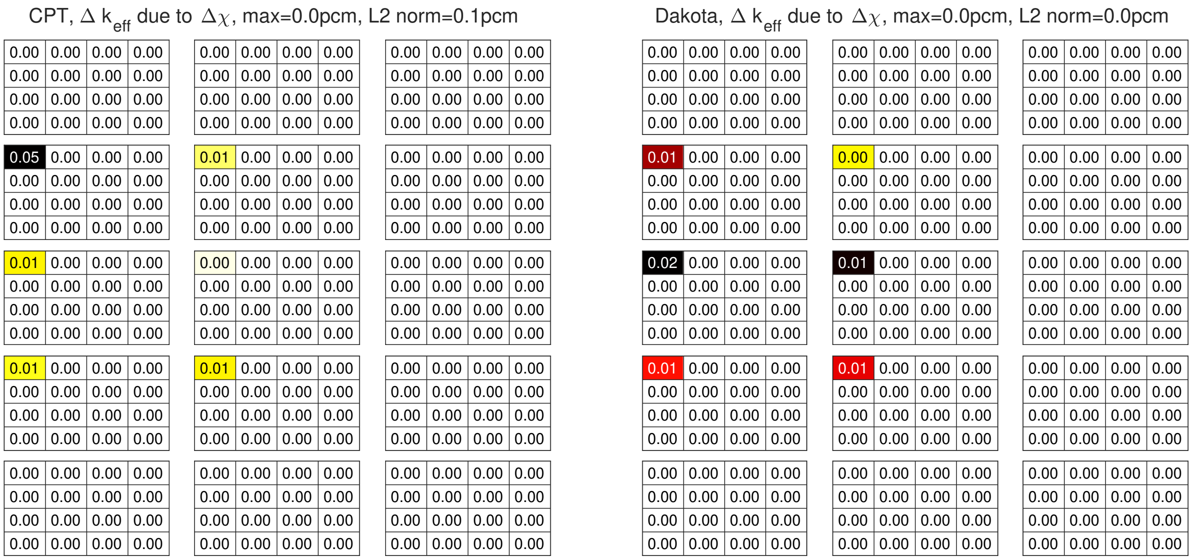
CPT, Δ k_{eff} due to $\Delta\chi$, max=0.0pcm, L2 norm=0.1pcm

0.00	0.00	0.00	0.00	0.00	0.00	0.00	0.00	0.00	0.00	0.00	0.00
0.00	0.00	0.00	0.00	0.00	0.00	0.00	0.00	0.00	0.00	0.00	0.00
0.00	0.00	0.00	0.00	0.00	0.00	0.00	0.00	0.00	0.00	0.00	0.00
0.00	0.00	0.00	0.00	0.00	0.00	0.00	0.00	0.00	0.00	0.00	0.00
0.05	0.00	0.00	0.00	0.01	0.00	0.00	0.00	0.00	0.00	0.00	0.00
0.00	0.00	0.00	0.00	0.00	0.00	0.00	0.00	0.00	0.00	0.00	0.00
0.00	0.00	0.00	0.00	0.00	0.00	0.00	0.00	0.00	0.00	0.00	0.00
0.00	0.00	0.00	0.00	0.00	0.00	0.00	0.00	0.00	0.00	0.00	0.00
0.01	0.00	0.00	0.00	0.00	0.00	0.00	0.00	0.00	0.00	0.00	0.00
0.00	0.00	0.00	0.00	0.00	0.00	0.00	0.00	0.00	0.00	0.00	0.00
0.00	0.00	0.00	0.00	0.00	0.00	0.00	0.00	0.00	0.00	0.00	0.00
0.00	0.00	0.00	0.00	0.00	0.00	0.00	0.00	0.00	0.00	0.00	0.00
0.01	0.00	0.00	0.00	0.01	0.00	0.00	0.00	0.00	0.00	0.00	0.00
0.00	0.00	0.00	0.00	0.00	0.00	0.00	0.00	0.00	0.00	0.00	0.00
0.00	0.00	0.00	0.00	0.00	0.00	0.00	0.00	0.00	0.00	0.00	0.00
0.00	0.00	0.00	0.00	0.00	0.00	0.00	0.00	0.00	0.00	0.00	0.00
0.00	0.00	0.00	0.00	0.00	0.00	0.00	0.00	0.00	0.00	0.00	0.00
0.00	0.00	0.00	0.00	0.00	0.00	0.00	0.00	0.00	0.00	0.00	0.00
0.00	0.00	0.00	0.00	0.00	0.00	0.00	0.00	0.00	0.00	0.00	0.00
0.00	0.00	0.00	0.00	0.00	0.00	0.00	0.00	0.00	0.00	0.00	0.00

Dakota, Δ k_{eff} due to $\Delta\chi$, max=0.0pcm, L2 norm=0.0pcm

0.00	0.00	0.00	0.00	0.00	0.00	0.00	0.00	0.00	0.00	0.00	0.00
0.00	0.00	0.00	0.00	0.00	0.00	0.00	0.00	0.00	0.00	0.00	0.00
0.00	0.00	0.00	0.00	0.00	0.00	0.00	0.00	0.00	0.00	0.00	0.00
0.00	0.00	0.00	0.00	0.00	0.00	0.00	0.00	0.00	0.00	0.00	0.00
0.01	0.00	0.00	0.00	0.00	0.00	0.00	0.00	0.00	0.00	0.00	0.00
0.00	0.00	0.00	0.00	0.00	0.00	0.00	0.00	0.00	0.00	0.00	0.00
0.00	0.00	0.00	0.00	0.00	0.00	0.00	0.00	0.00	0.00	0.00	0.00
0.00	0.00	0.00	0.00	0.00	0.00	0.00	0.00	0.00	0.00	0.00	0.00
0.02	0.00	0.00	0.00	0.01	0.00	0.00	0.00	0.00	0.00	0.00	0.00
0.00	0.00	0.00	0.00	0.00	0.00	0.00	0.00	0.00	0.00	0.00	0.00
0.00	0.00	0.00	0.00	0.00	0.00	0.00	0.00	0.00	0.00	0.00	0.00
0.00	0.00	0.00	0.00	0.00	0.00	0.00	0.00	0.00	0.00	0.00	0.00
0.01	0.00	0.00	0.00	0.01	0.00	0.00	0.00	0.00	0.00	0.00	0.00
0.00	0.00	0.00	0.00	0.00	0.00	0.00	0.00	0.00	0.00	0.00	0.00
0.00	0.00	0.00	0.00	0.00	0.00	0.00	0.00	0.00	0.00	0.00	0.00
0.00	0.00	0.00	0.00	0.00	0.00	0.00	0.00	0.00	0.00	0.00	0.00
0.00	0.00	0.00	0.00	0.00	0.00	0.00	0.00	0.00	0.00	0.00	0.00
0.00	0.00	0.00	0.00	0.00	0.00	0.00	0.00	0.00	0.00	0.00	0.00
0.00	0.00	0.00	0.00	0.00	0.00	0.00	0.00	0.00	0.00	0.00	0.00
0.00	0.00	0.00	0.00	0.00	0.00	0.00	0.00	0.00	0.00	0.00	0.00

Fig. 3.9: k_{eff} uncertainty contributed from Δ_{Σ_s}, 4-group case

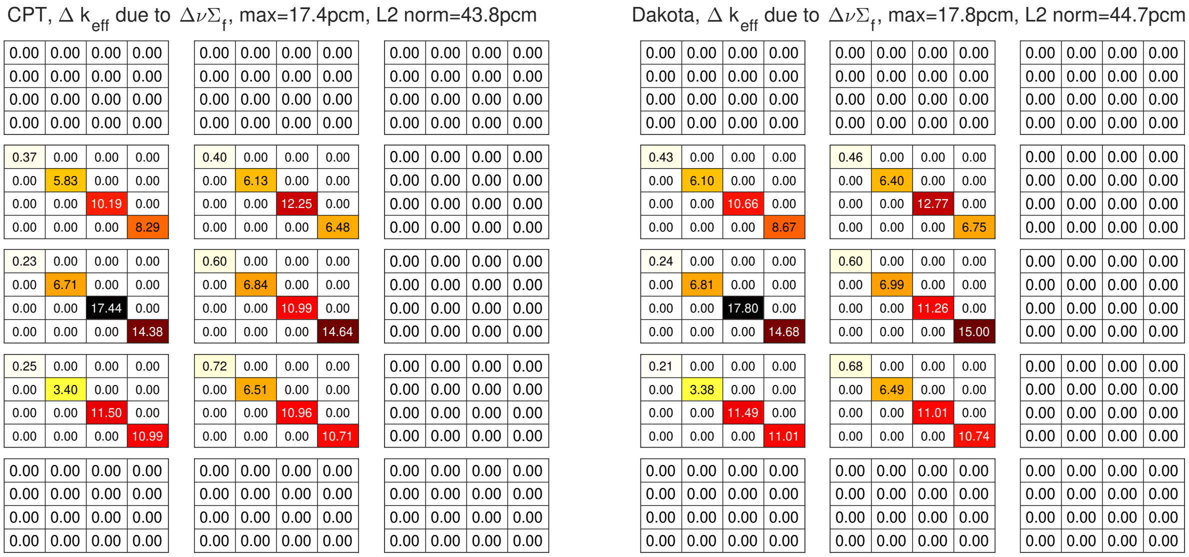
CPT, Δ k_{eff} due to $\Delta\nu\Sigma_f$, max=17.4pcm, L2 norm=43.8pcm

0.00	0.00	0.00	0.00	0.00	0.00	0.00	0.00	0.00	0.00	0.00	0.00
0.00	0.00	0.00	0.00	0.00	0.00	0.00	0.00	0.00	0.00	0.00	0.00
0.00	0.00	0.00	0.00	0.00	0.00	0.00	0.00	0.00	0.00	0.00	0.00
0.00	0.00	0.00	0.00	0.00	0.00	0.00	0.00	0.00	0.00	0.00	0.00
0.37	0.00	0.00	0.00	0.40	0.00	0.00	0.00	0.00	0.00	0.00	0.00
0.00	5.83	0.00	0.00	0.00	6.13	0.00	0.00	0.00	0.00	0.00	0.00
0.00	0.00	10.19	0.00	0.00	0.00	12.25	0.00	0.00	0.00	0.00	0.00
0.00	0.00	0.00	8.29	0.00	0.00	0.00	6.48	0.00	0.00	0.00	0.00
0.23	0.00	0.00	0.00	0.60	0.00	0.00	0.00	0.00	0.00	0.00	0.00
0.00	6.71	0.00	0.00	0.00	6.84	0.00	0.00	0.00	0.00	0.00	0.00
0.00	0.00	17.44	0.00	0.00	0.00	10.99	0.00	0.00	0.00	0.00	0.00
0.00	0.00	0.00	14.38	0.00	0.00	0.00	14.64	0.00	0.00	0.00	0.00
0.25	0.00	0.00	0.00	0.72	0.00	0.00	0.00	0.00	0.00	0.00	0.00
0.00	3.40	0.00	0.00	0.00	6.51	0.00	0.00	0.00	0.00	0.00	0.00
0.00	0.00	11.50	0.00	0.00	0.00	10.96	0.00	0.00	0.00	0.00	0.00
0.00	0.00	0.00	10.99	0.00	0.00	0.00	10.71	0.00	0.00	0.00	0.00
0.00	0.00	0.00	0.00	0.00	0.00	0.00	0.00	0.00	0.00	0.00	0.00
0.00	0.00	0.00	0.00	0.00	0.00	0.00	0.00	0.00	0.00	0.00	0.00
0.00	0.00	0.00	0.00	0.00	0.00	0.00	0.00	0.00	0.00	0.00	0.00
0.00	0.00	0.00	0.00	0.00	0.00	0.00	0.00	0.00	0.00	0.00	0.00

Dakota, Δ k_{eff} due to $\Delta\nu\Sigma_f$, max=17.8pcm, L2 norm=44.7pcm

0.00	0.00	0.00	0.00	0.00	0.00	0.00	0.00	0.00	0.00	0.00	0.00
0.00	0.00	0.00	0.00	0.00	0.00	0.00	0.00	0.00	0.00	0.00	0.00
0.00	0.00	0.00	0.00	0.00	0.00	0.00	0.00	0.00	0.00	0.00	0.00
0.00	0.00	0.00	0.00	0.00	0.00	0.00	0.00	0.00	0.00	0.00	0.00
0.43	0.00	0.00	0.00	0.46	0.00	0.00	0.00	0.00	0.00	0.00	0.00
0.00	6.10	0.00	0.00	0.00	6.40	0.00	0.00	0.00	0.00	0.00	0.00
0.00	0.00	10.66	0.00	0.00	0.00	12.77	0.00	0.00	0.00	0.00	0.00
0.00	0.00	0.00	8.67	0.00	0.00	0.00	6.75	0.00	0.00	0.00	0.00
0.24	0.00	0.00	0.00	0.60	0.00	0.00	0.00	0.00	0.00	0.00	0.00
0.00	6.81	0.00	0.00	0.00	6.99	0.00	0.00	0.00	0.00	0.00	0.00
0.00	0.00	17.80	0.00	0.00	0.00	11.26	0.00	0.00	0.00	0.00	0.00
0.00	0.00	0.00	14.68	0.00	0.00	0.00	15.00	0.00	0.00	0.00	0.00
0.21	0.00	0.00	0.00	0.68	0.00	0.00	0.00	0.00	0.00	0.00	0.00
0.00	3.38	0.00	0.00	0.00	6.49	0.00	0.00	0.00	0.00	0.00	0.00
0.00	0.00	11.49	0.00	0.00	0.00	11.01	0.00	0.00	0.00	0.00	0.00
0.00	0.00	0.00	11.01	0.00	0.00	0.00	10.74	0.00	0.00	0.00	0.00
0.00	0.00	0.00	0.00	0.00	0.00	0.00	0.00	0.00	0.00	0.00	0.00
0.00	0.00	0.00	0.00	0.00	0.00	0.00	0.00	0.00	0.00	0.00	0.00
0.00	0.00	0.00	0.00	0.00	0.00	0.00	0.00	0.00	0.00	0.00	0.00
0.00	0.00	0.00	0.00	0.00	0.00	0.00	0.00	0.00	0.00	0.00	0.00

Fig. 3.10: k_{eff} uncertainty contributed from $\Delta_{\nu\Sigma_f}$, 4-group case

Table 3.7: Summary of $\Delta_{k_{\text{eff}}}$ sources for the 4-group case

Cross section type	Max (pcm)		$\mathcal{L}$-2 norm (pcm)		percentage (%)	
	CPT	Dakota	CPT	Dakota	CPT	Dakota
Δ_χ	0.0	0.0	0.1	0.0	0.0	0.0
$\Delta_{\nu\Sigma_f}$	17.4	17.8	43.8	44.7	52.9	53.1
$\Delta_{\Sigma_{tr}}$	0.2	0.2	0.5	0.3	0.0	0.0
$\Delta_{\Sigma_{ab}}$	15.5	15.8	39.7	40.2	43.5	43.4
Δ_{Σ_s}	6.8	6.9	11.4	11.6	3.6	3.5

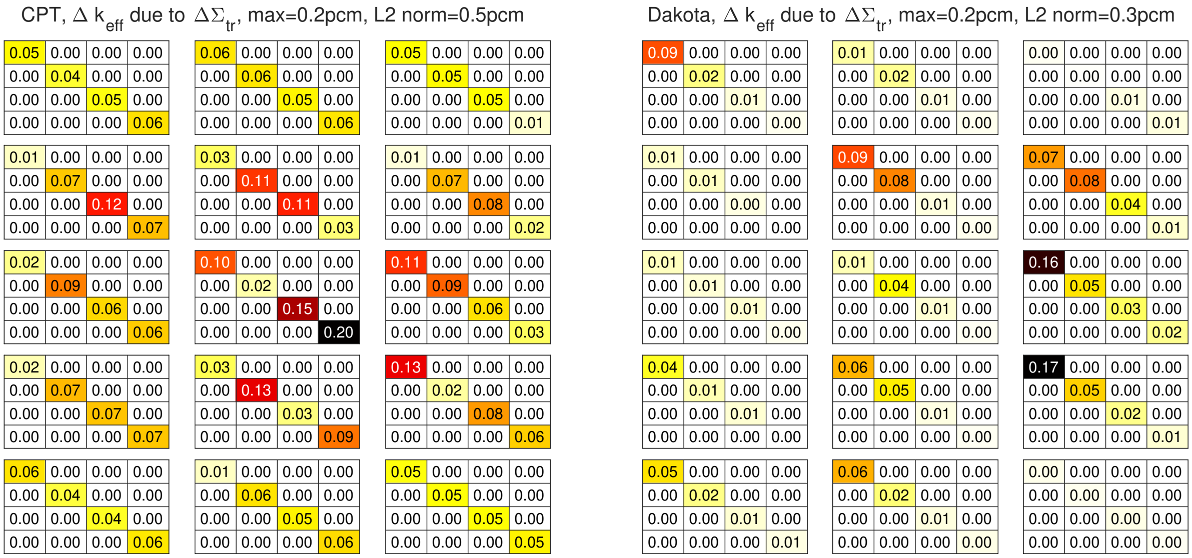

CPT, Δ k_{eff} due to $\Delta\Sigma_{tr}$, max=0.2pcm, L2 norm=0.5pcm

0.05	0.00	0.00	0.00	0.06	0.00	0.00	0.00	0.05	0.00	0.00	0.00
0.00	0.04	0.00	0.00	0.00	0.06	0.00	0.00	0.00	0.05	0.00	0.00
0.00	0.00	0.05	0.00	0.00	0.00	0.05	0.00	0.00	0.00	0.05	0.00
0.00	0.00	0.00	0.06	0.00	0.00	0.00	0.06	0.00	0.00	0.00	0.01
0.01	0.00	0.00	0.00	0.03	0.00	0.00	0.00	0.01	0.00	0.00	0.00
0.00	0.07	0.00	0.00	0.00	0.11	0.00	0.00	0.00	0.07	0.00	0.00
0.00	0.00	0.12	0.00	0.00	0.00	0.11	0.00	0.00	0.00	0.08	0.00
0.00	0.00	0.00	0.07	0.00	0.00	0.00	0.03	0.00	0.00	0.00	0.02
0.02	0.00	0.00	0.00	0.10	0.00	0.00	0.00	0.11	0.00	0.00	0.00
0.00	0.09	0.00	0.00	0.00	0.02	0.00	0.00	0.00	0.09	0.00	0.00
0.00	0.00	0.06	0.00	0.00	0.00	0.15	0.00	0.00	0.00	0.06	0.00
0.00	0.00	0.00	0.06	0.00	0.00	0.00	0.20	0.00	0.00	0.00	0.03
0.02	0.00	0.00	0.00	0.03	0.00	0.00	0.00	0.13	0.00	0.00	0.00
0.00	0.07	0.00	0.00	0.00	0.13	0.00	0.00	0.00	0.02	0.00	0.00
0.00	0.00	0.07	0.00	0.00	0.00	0.03	0.00	0.00	0.00	0.08	0.00
0.00	0.00	0.00	0.07	0.00	0.00	0.00	0.09	0.00	0.00	0.00	0.06
0.06	0.00	0.00	0.00	0.01	0.00	0.00	0.00	0.05	0.00	0.00	0.00
0.00	0.04	0.00	0.00	0.00	0.06	0.00	0.00	0.00	0.05	0.00	0.00
0.00	0.00	0.04	0.00	0.00	0.00	0.05	0.00	0.00	0.00	0.05	0.00
0.00	0.00	0.00	0.06	0.00	0.00	0.00	0.06	0.00	0.00	0.00	0.05

Dakota, Δ k_{eff} due to $\Delta\Sigma_{tr}$, max=0.2pcm, L2 norm=0.3pcm

0.09	0.00	0.00	0.00	0.01	0.00	0.00	0.00	0.00	0.00	0.00	0.00
0.00	0.02	0.00	0.00	0.00	0.02	0.00	0.00	0.00	0.00	0.00	0.00
0.00	0.00	0.01	0.00	0.00	0.00	0.01	0.00	0.00	0.00	0.01	0.00
0.00	0.00	0.00	0.00	0.00	0.00	0.00	0.00	0.00	0.00	0.00	0.01
0.01	0.00	0.00	0.00	0.09	0.00	0.00	0.00	0.07	0.00	0.00	0.00
0.00	0.01	0.00	0.00	0.00	0.08	0.00	0.00	0.00	0.08	0.00	0.00
0.00	0.00	0.00	0.00	0.00	0.00	0.01	0.00	0.00	0.00	0.04	0.00
0.00	0.00	0.00	0.00	0.00	0.00	0.00	0.00	0.00	0.00	0.00	0.01
0.01	0.00	0.00	0.00	0.01	0.00	0.00	0.00	0.16	0.00	0.00	0.00
0.00	0.01	0.00	0.00	0.00	0.04	0.00	0.00	0.00	0.05	0.00	0.00
0.00	0.00	0.01	0.00	0.00	0.00	0.01	0.00	0.00	0.00	0.03	0.00
0.00	0.00	0.00	0.00	0.00	0.00	0.00	0.00	0.00	0.00	0.00	0.02
0.04	0.00	0.00	0.00	0.06	0.00	0.00	0.00	0.17	0.00	0.00	0.00
0.00	0.01	0.00	0.00	0.00	0.05	0.00	0.00	0.00	0.05	0.00	0.00
0.00	0.00	0.01	0.00	0.00	0.00	0.01	0.00	0.00	0.00	0.02	0.00
0.00	0.00	0.00	0.00	0.00	0.00	0.00	0.00	0.00	0.00	0.00	0.01
0.05	0.00	0.00	0.00	0.06	0.00	0.00	0.00	0.00	0.00	0.00	0.00
0.00	0.02	0.00	0.00	0.00	0.02	0.00	0.00	0.00	0.00	0.00	0.00
0.00	0.00	0.01	0.00	0.00	0.00	0.01	0.00	0.00	0.00	0.00	0.00
0.00	0.00	0.00	0.01	0.00	0.00	0.00	0.00	0.00	0.00	0.00	0.00

Fig. 3.11: k_{eff} uncertainty contributed from $\Delta_{\Sigma_{tr}}$, 4-group case

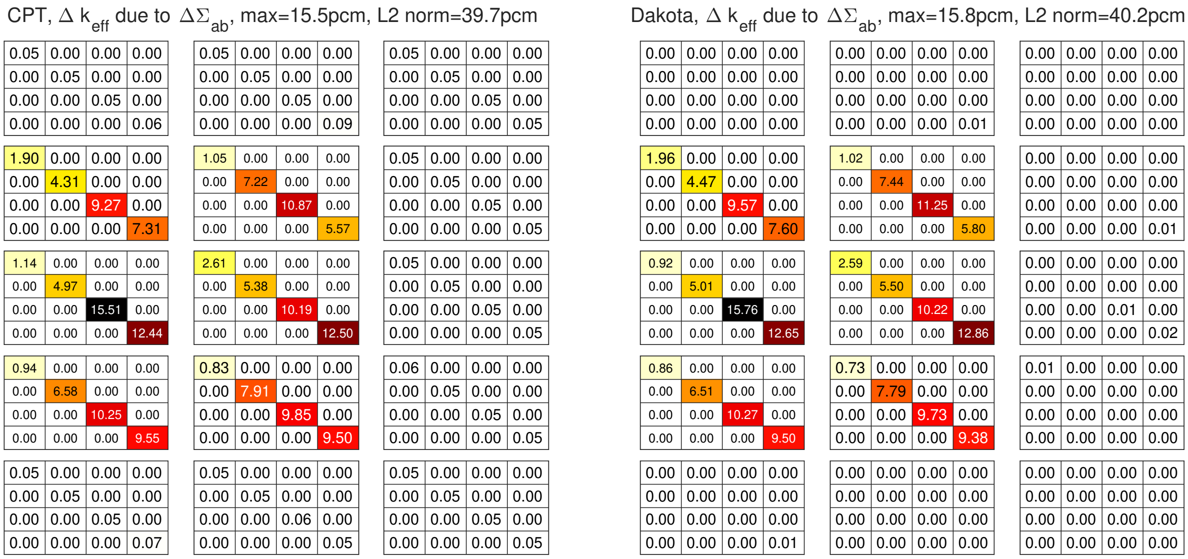

CPT, Δ k_{eff} due to $\Delta\Sigma_{ab}$, max=15.5pcm, L2 norm=39.7pcm

0.05	0.00	0.00	0.00	0.05	0.00	0.00	0.00	0.05	0.00	0.00	0.00
0.00	0.05	0.00	0.00	0.00	0.05	0.00	0.00	0.00	0.05	0.00	0.00
0.00	0.00	0.05	0.00	0.00	0.00	0.05	0.00	0.00	0.00	0.05	0.00
0.00	0.00	0.00	0.06	0.00	0.00	0.00	0.09	0.00	0.00	0.00	0.05
1.90	0.00	0.00	0.00	1.05	0.00	0.00	0.00	0.05	0.00	0.00	0.00
0.00	4.31	0.00	0.00	0.00	7.22	0.00	0.00	0.00	0.05	0.00	0.00
0.00	0.00	9.27	0.00	0.00	0.00	10.87	0.00	0.00	0.00	0.05	0.00
0.00	0.00	0.00	7.31	0.00	0.00	0.00	5.57	0.00	0.00	0.00	0.05
1.14	0.00	0.00	0.00	2.61	0.00	0.00	0.00	0.05	0.00	0.00	0.00
0.00	4.97	0.00	0.00	0.00	5.38	0.00	0.00	0.00	0.05	0.00	0.00
0.00	0.00	15.51	0.00	0.00	0.00	10.19	0.00	0.00	0.00	0.05	0.00
0.00	0.00	0.00	12.44	0.00	0.00	0.00	12.50	0.00	0.00	0.00	0.05
0.94	0.00	0.00	0.00	0.83	0.00	0.00	0.00	0.06	0.00	0.00	0.00
0.00	6.58	0.00	0.00	0.00	7.91	0.00	0.00	0.00	0.05	0.00	0.00
0.00	0.00	10.25	0.00	0.00	0.00	9.85	0.00	0.00	0.00	0.05	0.00
0.00	0.00	0.00	9.55	0.00	0.00	0.00	9.50	0.00	0.00	0.00	0.05
0.05	0.00	0.00	0.00	0.05	0.00	0.00	0.00	0.05	0.00	0.00	0.00
0.00	0.05	0.00	0.00	0.00	0.05	0.00	0.00	0.00	0.05	0.00	0.00
0.00	0.00	0.05	0.00	0.00	0.00	0.06	0.00	0.00	0.00	0.05	0.00
0.00	0.00	0.00	0.07	0.00	0.00	0.00	0.05	0.00	0.00	0.00	0.05

Dakota, Δ k_{eff} due to $\Delta\Sigma_{ab}$, max=15.8pcm, L2 norm=40.2pcm

0.00	0.00	0.00	0.00	0.00	0.00	0.00	0.00	0.00	0.00	0.00	0.00
0.00	0.00	0.00	0.00	0.00	0.00	0.00	0.00	0.00	0.00	0.00	0.00
0.00	0.00	0.00	0.00	0.00	0.00	0.00	0.00	0.00	0.00	0.00	0.00
0.00	0.00	0.00	0.00	0.00	0.00	0.00	0.01	0.00	0.00	0.00	0.00
1.96	0.00	0.00	0.00	1.02	0.00	0.00	0.00	0.00	0.00	0.00	0.00
0.00	4.47	0.00	0.00	0.00	7.44	0.00	0.00	0.00	0.00	0.00	0.00
0.00	0.00	9.57	0.00	0.00	0.00	11.25	0.00	0.00	0.00	0.00	0.00
0.00	0.00	0.00	7.60	0.00	0.00	0.00	5.80	0.00	0.00	0.00	0.01
0.92	0.00	0.00	0.00	2.59	0.00	0.00	0.00	0.00	0.00	0.00	0.00
0.00	5.01	0.00	0.00	0.00	5.50	0.00	0.00	0.00	0.00	0.00	0.00
0.00	0.00	15.76	0.00	0.00	0.00	10.22	0.00	0.00	0.00	0.01	0.00
0.00	0.00	0.00	12.65	0.00	0.00	0.00	12.86	0.00	0.00	0.00	0.02
0.86	0.00	0.00	0.00	0.73	0.00	0.00	0.00	0.01	0.00	0.00	0.00
0.00	6.51	0.00	0.00	0.00	7.79	0.00	0.00	0.00	0.00	0.00	0.00
0.00	0.00	10.27	0.00	0.00	0.00	9.73	0.00	0.00	0.00	0.00	0.00
0.00	0.00	0.00	9.50	0.00	0.00	0.00	9.38	0.00	0.00	0.00	0.00
0.00	0.00	0.00	0.00	0.00	0.00	0.00	0.00	0.00	0.00	0.00	0.00
0.00	0.00	0.00	0.00	0.00	0.00	0.00	0.00	0.00	0.00	0.00	0.00
0.00	0.00	0.00	0.00	0.00	0.00	0.00	0.00	0.00	0.00	0.00	0.00
0.00	0.00	0.00	0.01	0.00	0.00	0.00	0.00	0.00	0.00	0.00	0.00

Fig. 3.12: k_{eff} uncertainty contributed from $\Delta_{\Sigma_{ab}}$, 4-group case

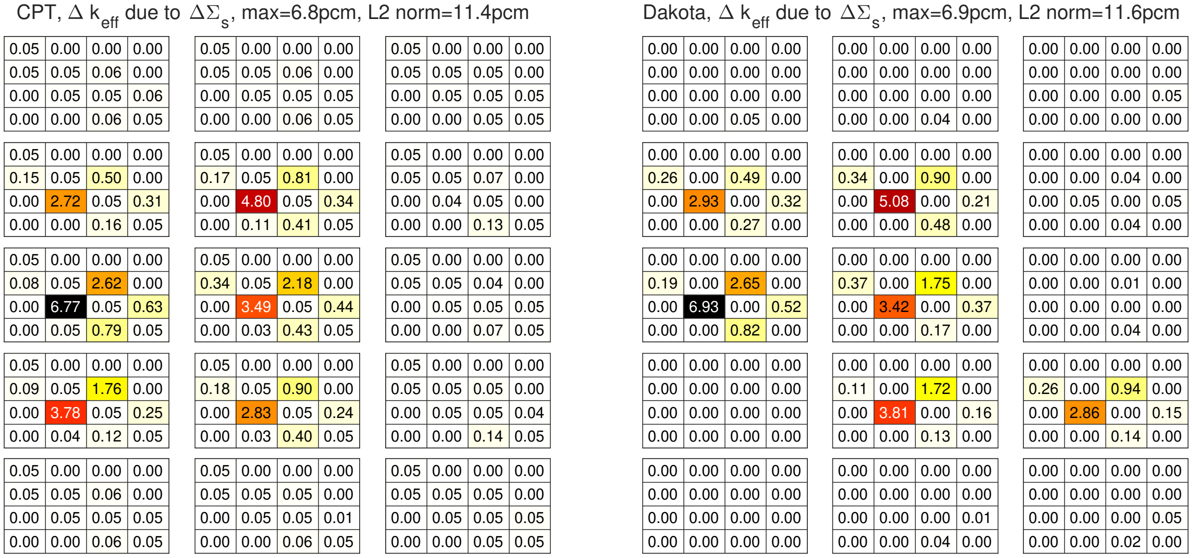

CPT, Δ k_{eff} due to $\Delta\Sigma_s$, max=6.8pcm, L2 norm=11.4pcm

0.05	0.00	0.00	0.00	0.05	0.00	0.00	0.00	0.05	0.00	0.00	0.00
0.05	0.05	0.06	0.00	0.05	0.05	0.06	0.00	0.05	0.05	0.05	0.00
0.00	0.05	0.05	0.06	0.00	0.05	0.05	0.05	0.00	0.05	0.05	0.05
0.00	0.00	0.06	0.05	0.00	0.00	0.06	0.05	0.00	0.00	0.05	0.05

0.05	0.00	0.00	0.00	0.05	0.00	0.00	0.00	0.05	0.00	0.00	0.00
0.15	0.05	0.50	0.00	0.17	0.05	0.81	0.00	0.05	0.05	0.07	0.00
0.00	2.72	0.05	0.31	0.00	4.80	0.05	0.34	0.00	0.04	0.05	0.00
0.00	0.00	0.16	0.05	0.00	0.11	0.41	0.05	0.00	0.00	0.13	0.05

0.05	0.00	0.00	0.00	0.05	0.00	0.00	0.00	0.05	0.00	0.00	0.00
0.08	0.05	2.62	0.00	0.34	0.05	2.18	0.00	0.05	0.05	0.04	0.00
0.00	6.77	0.05	0.63	0.00	3.49	0.05	0.44	0.00	0.05	0.05	0.05
0.00	0.05	0.79	0.05	0.00	0.03	0.43	0.05	0.00	0.00	0.07	0.05

0.05	0.00	0.00	0.00	0.05	0.00	0.00	0.00	0.05	0.00	0.00	0.00
0.09	0.05	1.76	0.00	0.18	0.05	0.90	0.00	0.05	0.05	0.05	0.00
0.00	3.78	0.05	0.25	0.00	2.83	0.05	0.24	0.00	0.05	0.05	0.04
0.00	0.04	0.12	0.05	0.00	0.03	0.40	0.05	0.00	0.00	0.14	0.05

0.05	0.00	0.00	0.00	0.05	0.00	0.00	0.00	0.05	0.00	0.00	0.00
0.05	0.05	0.06	0.00	0.05	0.05	0.05	0.00	0.05	0.05	0.05	0.00
0.00	0.05	0.05	0.05	0.00	0.05	0.05	0.01	0.00	0.05	0.05	0.05
0.00	0.00	0.06	0.05	0.00	0.00	0.06	0.05	0.00	0.00	0.05	0.05

Dakota, Δ k_{eff} due to $\Delta\Sigma_s$, max=6.9pcm, L2 norm=11.6pcm

0.00	0.00	0.00	0.00	0.00	0.00	0.00	0.00	0.00	0.00	0.00	0.00
0.00	0.00	0.00	0.00	0.00	0.00	0.00	0.00	0.00	0.00	0.00	0.00
0.00	0.00	0.00	0.00	0.00	0.00	0.00	0.00	0.00	0.00	0.00	0.05
0.00	0.00	0.05	0.00	0.00	0.00	0.04	0.00	0.00	0.00	0.00	0.00

0.00	0.00	0.00	0.00	0.00	0.00	0.00	0.00	0.00	0.00	0.00	0.00
0.26	0.00	0.49	0.00	0.34	0.00	0.90	0.00	0.00	0.00	0.04	0.00
0.00	2.93	0.00	0.32	0.00	5.08	0.00	0.21	0.00	0.05	0.00	0.05
0.00	0.00	0.27	0.00	0.00	0.00	0.48	0.00	0.00	0.00	0.04	0.00

0.00	0.00	0.00	0.00	0.00	0.00	0.00	0.00	0.00	0.00	0.00	0.00
0.19	0.00	2.65	0.00	0.37	0.00	1.75	0.00	0.00	0.00	0.01	0.00
0.00	6.93	0.00	0.52	0.00	3.42	0.00	0.37	0.00	0.00	0.00	0.00
0.00	0.00	0.82	0.00	0.00	0.00	0.17	0.00	0.00	0.00	0.04	0.00

0.00	0.00	0.00	0.00	0.00	0.00	0.00	0.00	0.00	0.00	0.00	0.00
0.00	0.00	0.00	0.00	0.11	0.00	1.72	0.00	0.26	0.00	0.94	0.00
0.00	0.00	0.00	0.00	0.00	3.81	0.00	0.16	0.00	2.86	0.00	0.15
0.00	0.00	0.00	0.00	0.00	0.00	0.13	0.00	0.00	0.00	0.14	0.00

0.00	0.00	0.00	0.00	0.00	0.00	0.00	0.00	0.00	0.00	0.00	0.00
0.00	0.00	0.00	0.00	0.00	0.00	0.00	0.00	0.00	0.00	0.00	0.00
0.00	0.00	0.00	0.00	0.00	0.00	0.00	0.01	0.00	0.00	0.00	0.05
0.00	0.00	0.00	0.00	0.00	0.00	0.04	0.00	0.00	0.00	0.02	0.00

Fig. 3.13: k_{eff} uncertainty contributed from Δ_{Σ_s}, 4-group case

For the contribution from $\Delta_{\nu\Sigma_f}$ and $\Delta_{\Sigma_{ab}}$, the fuel regions contribute more than the reflector regions and the thermal groups contribute more than the fast groups.

3.3.4 Factors Affecting Uncertainty

3.3.4.1 Number of Groups

In this demonstration problem, five different energy group structures were used. The relation between the total $\Delta_{k_{\text{eff}}}$ and the number of groups is plotted in Fig. 3.14. By comparing the results of different group structures in Table 3.6, it shows that if the total number of neutron histories in Serpent calculation remains unchanged, the $\mathcal{L}$-2 norm estimated total uncertainty of AGREE k_{eff} due to the uncertainty of MC cross section data remain essentially unchanged, regardless of the number of energy groups used for generating the cross section data.

According to Fig. 3.2, when the total number of neutron histories is fixed in Monte Carlo calculations, the uncertainty of MC generated cross sections becomes larger as increasing the number of groups. The reason is that when increasing the number of groups, the energy interval becomes smaller, which results a smaller number of statistics in the energy bin. But since the energy bin is narrower, the larger cross section error will not increase the contribution to the uncertainty of k_{eff} . That is the reason why the $\mathcal{L}$-2 norm estimated uncertainty of k_{eff} is insensitive to the number of groups as long as the total number of neutron histories is fixed.

For the $\mathcal{L}$-1 norm estimation and the region-independent estimation, the uncertainty of k_{eff} increases when the number of groups increases. It is because the larger number of groups is used in cross section generation, the more cross section data are generated and the correlations

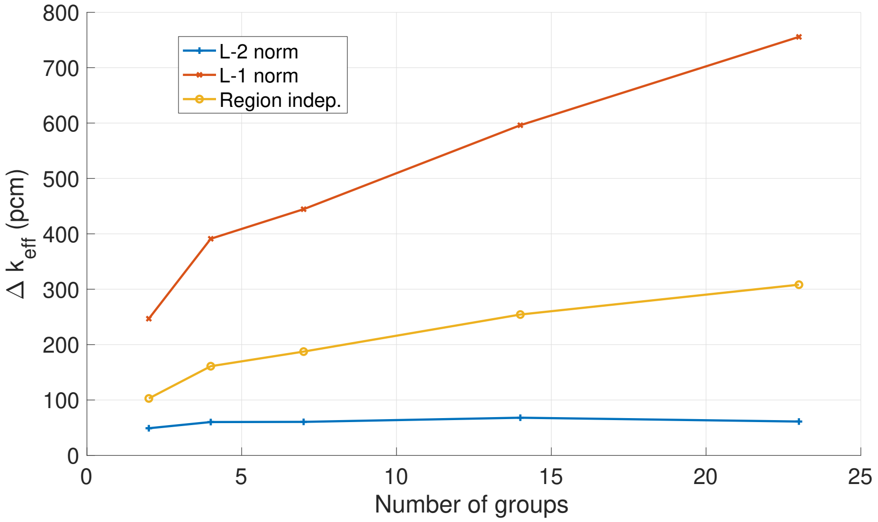

Fig. 3.14: Relation between k_{eff} uncertainty and the number of groups

between them are more significantly overestimated.

3.3.4.2 Number of Neutron Histories

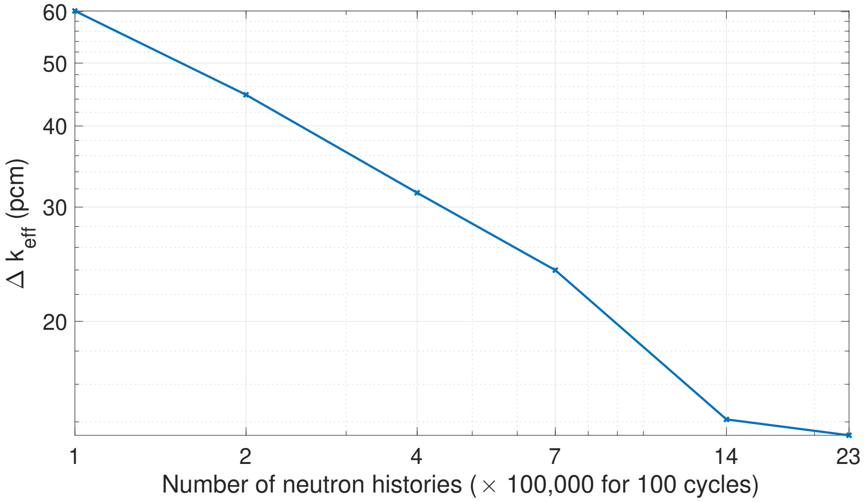

Fig. 3.15: Relation between k_{eff} uncertainty and the number of neutron histories

When generating cross sections from Monte Corlo calculation, increasing the number of neutron histories can reduce the uncertainty of the cross sections, as shown in Fig. 3.3. In this demonstration problem, the relation between the k_{eff} uncertainty and the number of neutron histories was investigated. The 4-group energy structure was used for this study.

The uncertainty of k_{eff} was calculated from CPT methods. When increasing the number of neutron histories from 100,000 to 2,300,000 for 100 cycles, the total uncertainty of k_{eff} is reduced from 60.2 pcm to 13.4 pcm. The results are plotted in Fig. 3.15. The x-axis and y-axis are in logarithmic scale. It shows that the uncertainty of k_{eff} is inversely proportional to the square root of the number of neutron histories, i.e., $\Delta_{k_{\text{eff}}} \propto \frac{1}{\sqrt{N}}$.

3.3.4.3 Mesh Refinement in Neutron Diffusion Calculation

When using AGREE to perform the neutronics simulation, there are usually two layer of meshes for the spatial discretization. The coarse mesh is used to set up the reactor core geometry. A finer mesh is built in the coarse mesh to accurately predict the flux distribution[47]. Although the cross section data is only applied on the coarse mesh level, conducting a study to learn the effect of mesh refinement on the uncertainty calculation is necessary.

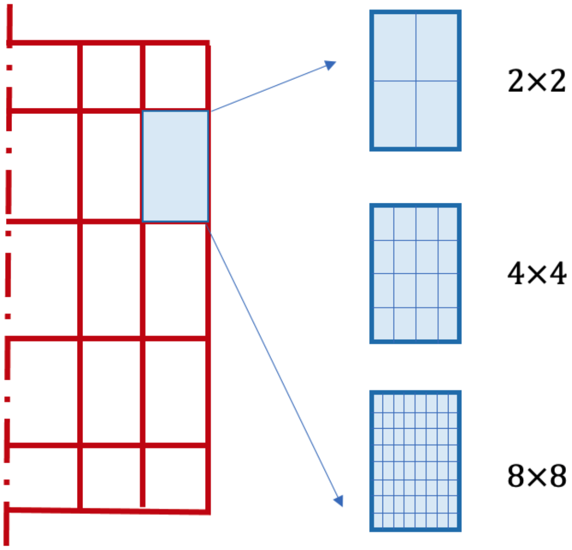

Fig. 3.16: Mesh refinement for the simplified gFHR core AGREE model

In the simplified gFHR core case, the coarse mesh is the 3×5 mesh as shown in Fig. 3.8. The mesh refinement effect is studied by refine the coarse mesh by 2×2, 4×4 and 8×8. This is depicted in Fig. 3.16.

The uncertainty calculations are performed with Dakota random sampling methods. The energy structure used for the study is the 7-group structure. The k_{eff} results and the uncertainties in different mesh refinement cases are list in Table 3.8. It shows that when refining the neutronics mesh, the k_{eff} result becomes closer to the Serpent k_{eff} (1.31377). However, the uncertainty of k_{eff} remains nearly the same. It means that the uncertainty of k_{eff} due to the uncertainty of cross section data does not depend on the mesh refinement in AGREE and is not a primary consideration when calculating the uncertainty of k_{eff} .

Table 3.8: k_{eff} and keff uncertainty with different mesh refinements

Mesh refinement	k_{eff}	$\Delta_{k_{\text{eff}}}$ (pcm)
1×1	1.29955	61.0
2×2	1.30035	59.2
4×4	1.31005	59.1
8×8	1.31579	59.9

In other words, the uncertainty of k_{eff} due to the uncertainty of cross section data only depends on the coarse mesh. In practice, the coarse mesh is usually the same as the homogenized cross section generation mesh. Therefore, when quantifying the k_{eff} uncertainty due to the cross section data uncertainty, the mesh refinement in the AGREE model can be removed to reduce the computational burden, by reducing both the memory usage and run time.

For the multi-physics coupling case, a higher resolution power distribution will be obtained with the mesh refinement, which helps predict the temperature distribution better. In such cases, the mesh refinement is necessary when propagating the cross section data uncertainty.

3.4 Comparison of Analytical and Stochastic UQ Methods for the HTR-10

Both the analytical and stochastic UQ methods developed in Section 3.2 were applied on the HTR-10 benchmark problem. This is considered an important first step in this research since the benchmark provides experimental data with measurement uncertainty which can be used to provide perspective on the relative magnitude of the modeling and simulation uncertainties. This perspective is not possible with the gFHR which is currently still in the design stage. However, since it is an advanced nuclear reactor, it is the application of primary interest in the research performed here. In the benchmark results presented in Section 2.3.2, three few-group structures, 4G, 8G and 14G, are used to generate homogenized cross sections for the AGREE neutron diffusion calculation. According to the results, the differences between the SERPENT k_{eff} result and the AGREE 8G and 14G k_{eff} are smaller compared to the 4G case, which suggests an increased number of energy groups in AGREE more accurately describes the physics of the reactor. However, the computational cost of the 14G is significantly larger than the 8G and 4G cases. So in the actual application, the 8G structure is a reasonable compromise of accuracy versus execution time and the analysis in this section was performed for the HTR-10 benchmark with the 8G structure.

3.4.1 UQ of Benchmark B1

The description and modeling approach of HTR-10 benchmark B1 was presented in Section 2.3.2.1. The results are shown in Table 2.2. Both analytical and stochastic methods are applied to calculate the uncertainty of AGREE k_{eff} due to MC generated cross section uncertainties.

For both methods, the uncertainties of χ, $\nu\Sigma_f$, Σ_{tr}, Σ_{ab} and Σ_s are taken into account. For the analytical method, the cross sections are perturbed independently; while for the stochastic method, all the cross sections in the same homoginized region are perturbed together. 108 random samples are created and evaluated for each perturbation in the stochastic method. The results estimated by $\mathcal{L}$-2 norm are listed in Table 3.9. As indicated, the results of the analytic and stochastic methods are similar which provides confidence in using the stochastic method for a wider range of responses than the restrictive use of CPT analytic methods for only the core k_{eff} .

Table 3.9: HTR-10 B1 $\Delta_{k_{\text{eff}}}$ due to MC generated cross section

Height [cm]	Serpent k_{eff}	AGREE k_{eff} (8-Group)	$\Delta_{k_{\text{eff}}}$ due to MC XS CPT (pcm)	Dakota (pcm)
112.06	0.95949	0.96305	17.0	16.3
118.06	0.98003	0.97770	17.3	16.3
124.06	0.99921	1.00519	16.4	15.8
130.06	1.01694	1.02358	17.4	16.7
136.06	1.03328	1.04333	17.2	16.7

3.4.2 UQ of Benchmark B4

The uncertainty of HTR-10 Benchmark B4 is calculated using the the stochastic method. The results estimated by $\mathcal{L}$-2 norm are shown in Table 3.10. The rod worth calculated by AGREE is $\rho_{cr} = 1649\ \mathrm{pcm}$, which is 180 pcm larger than the benchmark experimental result. The uncertainty of ρ_{cr} can be calculated with Eq. 5.6, which is 20.5 pcm.

Table 3.10: HTR-10 Benchmark B4 $\Delta_{k_{\text{eff}}}$ due to MC generated cross section

Case	Serpent k_{eff} ± std.dev. (pcm)	AGREE k_{eff} (8-Group)	$\Delta_{k_{\text{eff}}}$ due to MC XS (by Dakota, pcm)
Rod in	0.98100 ±7.0	0.98612	14.4
Rod out	0.99680 ±7.1	1.00242	14.2

3.4.3 UQ of Test B2

The uncertainty of HTR-10 Test B2 is calculated using the the stochastic method. The results estimated by $\mathcal{L}$-2 norm are shown in Table 3.10.

Table 3.11: HTR-10 Test B2 $\Delta_{k_{\text{eff}}}$ due to MC generated cross section

Temperature ($^\circ\mathrm{C}$)	Serpent k_{eff} ± std.dev. (pcm)	AGREE k_{eff} (8-Group)	$\Delta_{k_{\text{eff}}}$ due to MC XS (by Dakota, pcm)
20	1.13823 ±7.3	1.14553	18.7
120	1.12712 ±7.4	1.13623	18.4
250	1.10920 ±7.5	1.11780	18.1

3.4.4 UQ of Test B3

The uncertainties of HTR-10 Benchmark B4 k_{eff} are calculated using the the stochastic method. The results estimated by $\mathcal{L}$-2 norm are shown in Table 3.12. The rod worth calculated by AGREE is $\rho_{cr} = 1291\ \mathrm{pcm}$, which is 52 pcm smaller than the Chinese MCNP benchmark result. The uncertainty of ρ_{cr} can be calculated with Eq. 5.6, which is 27.1 pcm.

Table 3.12: HTR-10 Test B3 $\Delta_{k_{\text{eff}}}$ due to MC generated cross section

Case	Serpent k_{eff} ± std.dev. (pcm)	AGREE k_{eff} (8-Group)	$\Delta_{k_{\text{eff}}}$ due to MC XS (by Dakota, pcm)
All rod in	1.136410 ±9.2	1.129690	24.0
All rod out	1.120300 ±9.4	1.146411	25.5

3.5 Summary

In this chapter, the statistical error of Monte Carlo generated cross sections are first assessed. It shows that the statistical error is inversely proportional to the square root of the number of neutron histories. The statistical error introduced from Monte Carlo cross section generation will bring additional uncertainty to the results of the subsequent neutronics and thermo-fluids simulations. Therefore, the quantification of the uncertainty of the subsequent calculations caused by the uncertainty of Monte Carlo generated cross sections are necessary.

Two types of methods are developed to propagate the uncertainty of Monte Carlo generated cross sections. One is the analytical method based on the conventional perturbation theory. The other is the stochastic method based on random sampling. The analytical method is implemented based on AGREE code and the stochastic method is implemented based on the coupling of AGREE code and Dakota code. Both methods are tested using a simplified gFHR fresh core demonstration problem and the results from both methods agree very well with each other which provided confidence in using the stochastic method for a wider range of responses than the restrictive use of CPT analytic methods. Some parametric studies are conducted to investigate the features of the Monte Carlo cross section uncertainty propagation and the factors affecting the uncertainty propagation.

The stochastic method is chosen as the uncertainty propagation method for the subsequent studies in this theis for its universality and extendibility.

Finally, the methods are applied on the HTR-10 benchmark problems. The uncertainties of the hybrid method calculated benchmark results due to Monte Carlo generated cross section were quantified.

CHAPTER 4

Uncertainty Analysis for the FHR: Steady-State Simulation

4.1 Introduction of FHR Steady-State Simulations

In Section 2.4, the description and modeling of gFHR benchmark was introduced. The gFHR benchmarks in Section 2.4 are neutronics simulations performed by Serpent and AGREE.

In this section, the neutronics simulations are coupled with thermo-fluids calculations using the SAM code. The uncertainty analysis methods developed in Chapter 3 are performed on both AGREE code and the SAM code to quantify the uncertainties of interested quantities propagated from the uncertainties of Monte Carlo generated cross section data.

4.1.1 Introduction of SAM Code

The System Analysis Module (SAM) is a system analysis code for the safety analysis developed by Argonne National Laboratory. It focuses on modeling and simulating advanced reactor concepts, including FHRs, Liquid-Metal-cooled fast Reactors (LMR), Molten Salt Reactors (MSR), and High-Temperature Gas-cooled Reactors (HTGR). SAM has the capabilities of modeling and simulating the heat transfer and single-phase fluid dynamics of the non-LWR coolants. SAM also has a reactor point kinetics model to simulate the reactor core neutronics responses.

SAM is being developed under the U.S. Department of Energy (DOE) Nuclear Energy Advanced Modeling and Simulation (NEAMS) program. SAM is a MOOSE-based (Multiphysics Object-Oriented Simulation Environment) code, which utilizes the libMesh library for the meshing and finite-element modeling, utilizes PETSc as the numerical linear and non-linear solvers.

4.1.2 Coupling Scheme for gFHR

The Monte Carlo-deterministic hybrid methods used for gFHR neutronics calculation is the same as what was described in Section 2.1. In addition to the neutronics simulation, the methods of thermo-fluids simulation for gFHR is also developed.

The coupling scheme for the gFHR simulation is shown in Fig. 4.1. For the thermo-fluids simulation of the gFHR in SAM, the core is modeled by a two-dimensional porous medium model and the external loops are represented by one-dimensional models. The internal point kinetics solver is employed for the coupling of neutronics in SAM. The essential neutronics parameters required by the point kinetics solver are provided by Serpent and AGREE. AGREE provides the power distribution in the gFHR core as the heat source in SAM's thermo-fluids calculations. The temperature coefficients and control rod worth are used for transient analysis. The delayed neutron parameters, including the delayed neutron fraction and the precursor decay constants, are provided by Serpent for the modeling of the point kinetics equations. The xenon cross sections and related parameters are provided by Serpent as well.

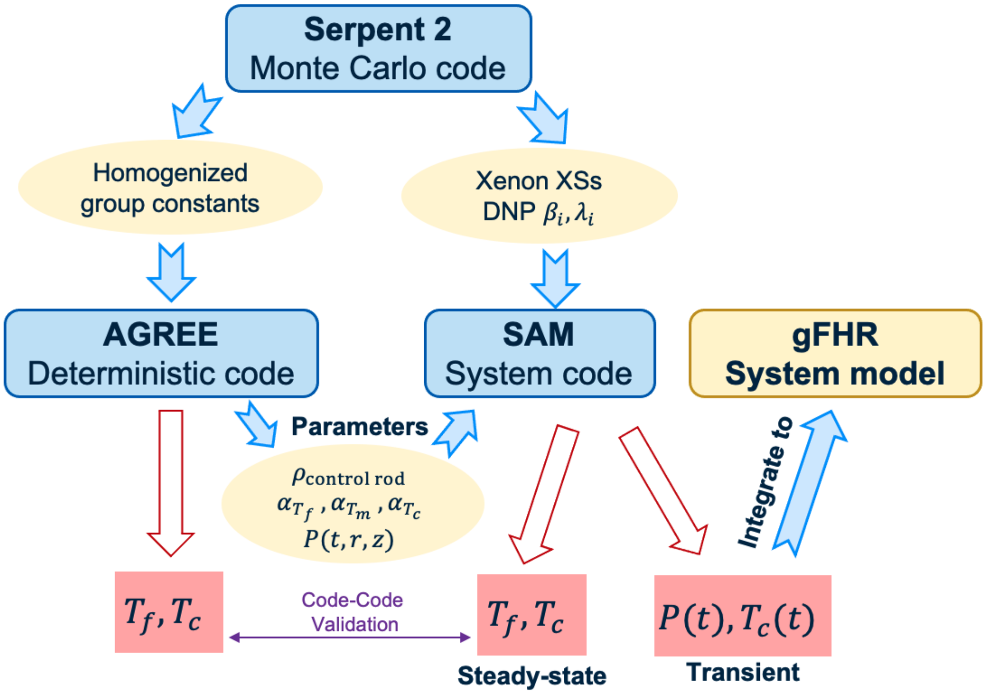

Fig. 4.1: The coupling scheme of Serpent-AGREE and SAM

The AGREE code also has the capability to model the thermo-fluids in the core of pebble-bed type reactors based on the porous media approach. Therefore, the fuel temperature and coolant temperature calculated by both codes are consistent and can be used for code-code validation.

4.1.3 Homogenized Cross Section Generation for gFHR

The following analysis will be based on the gFHR equilibrium core at hot full power (HFP) condition, instead of the gFHR fresh core at hot zero power (HZP) condition in Section 3.3. The cross section generation methods used for HFP cores are a little different from the HZP cores.

The homogenized cross section generation for the HFP cores includes three steps.

Step 1 Since the core temperature distributions are unknown, the temperature distributions of fuel, coolant, moderator and reflector are all assumed to be uniform in Serpent modeling. The cross sections are generated based on the uniform temperature by Serpent

Step 2 The cross section generated in Step 1 is used in AGREE to perform the neutronics and thermo-fluids coupling calculation. Then the temperature distributions of fuel, coolant, moderator and reflector are obtained.

Step 3 The temperature distributions obtained in Step 2 are applied to the Serpent model. Then the homogenized cross sections at HFP condition are generated by Serpent.

Above method is depicted in Fig. 4.2. The cross sections are generated twice, one is with uniform temperature distributions at HZP condition and another is with “actual” temperature distributions at HFP condition. The cross sections generated in Step 3 are more accurate since it uses better temperature distributions.

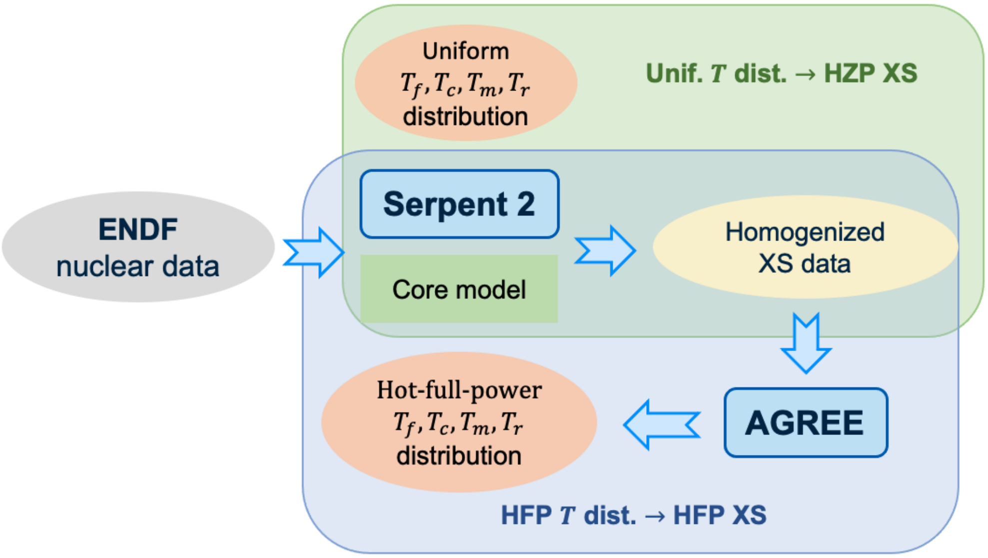

Fig. 4.2: The cross section generation method for HFP cores

To be noted, the temperature distributions in Step 3 is calculated from Step 2, in which the cross sections are not accurate enough. It means that the temperature distributions used in Step 3 are still not the exact HFP temperature distributions. Therefore, the Step 2 and Step 3 can be repeated multiple times to reach a convergence of the exact temperature distributions and cross sections at HFP condition. However, in practice the Step 2 and Step 3 are performed only one time and the cross sections and temperature distributions are accurate enough (See Appendix C).

4.1.4 Calculation of Temperature Distribution

The core temperature distributions discussed in Section 4.1.3 are calculated with AGREE code. A simple single-channel thermo-fluid model is developed based on the porous media approach in AGREE, which is shown in Fig. 4.3. The flibe flow comes from the inlet, goes down the downcomer and flows into the bottom of the active core. The mass flow rate is 1173.0 $\mathrm{kg/s}$. The core inlet temperature is 550 $^{\circ}\mathrm{C}$ (823 K). The outlet temperature is 650 $^{\circ}\mathrm{C}$ (923 K).

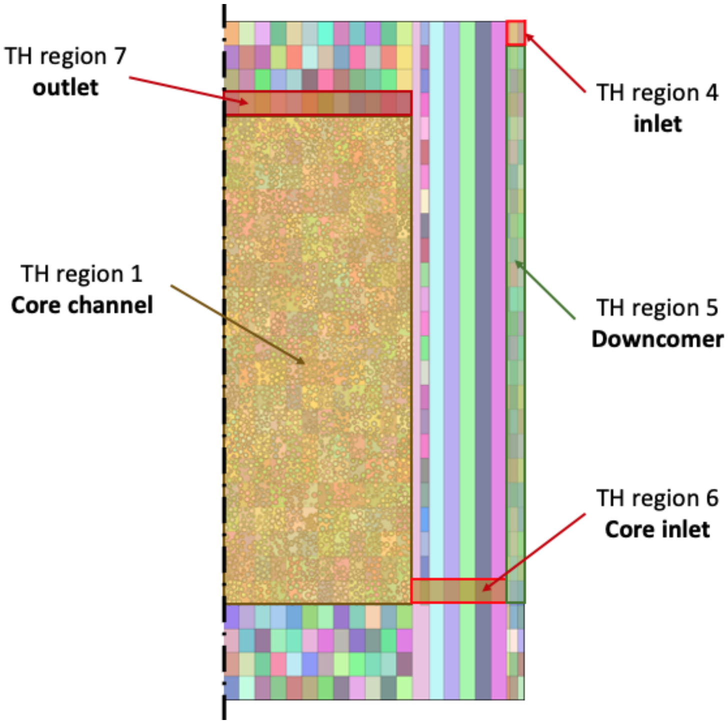

Fig. 4.3: Single-channel thermo-fluid model in AGREE

Using AGREE neutronics and thermo-fluid coupling calculation, the temperature distributions of the gFHR core can be obtained. Fig. 4.4 and Fig. 4.5 show the temperature distribution of fuel, coolant, moderator and reflector, respectively.

According to Fig. 4.4, the hottest region (1031.4 K) in the core is middle upper region at the centerline of the core, which is also the highest power density occurs. The highest coolant temperature (936.2 K) occurs at the outlet of the core centerline.

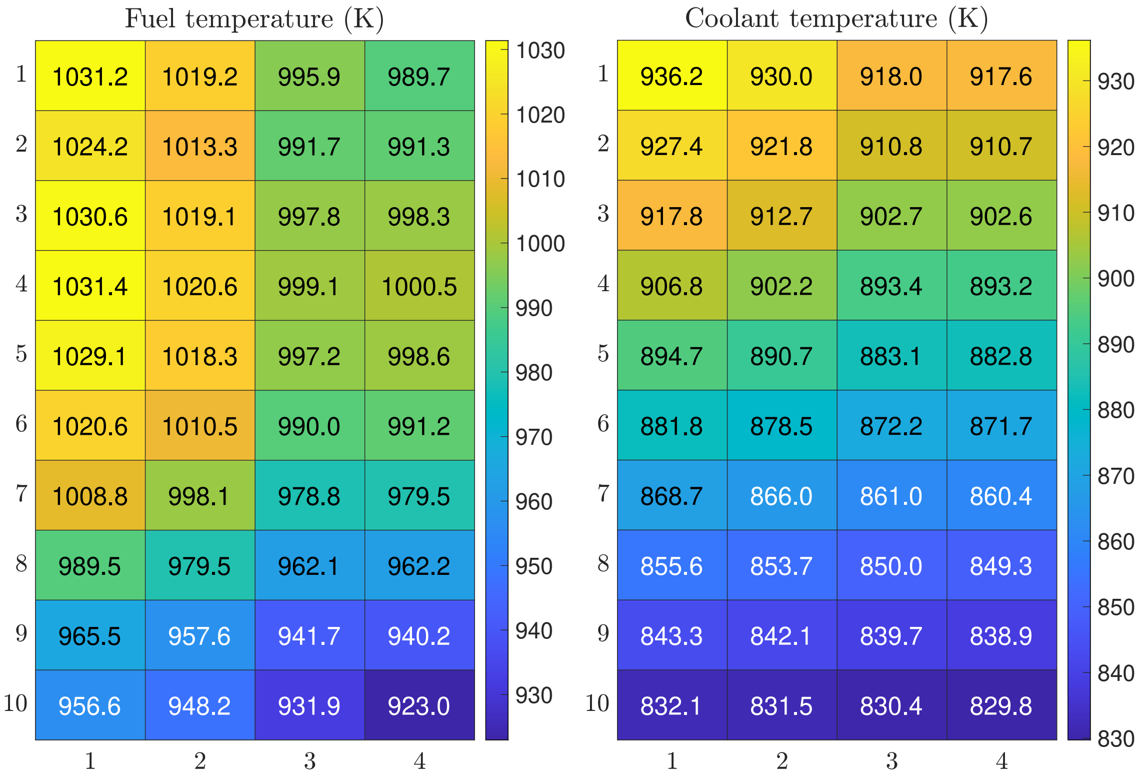

Fuel temperature (K)

	1	2	3	4
1	1031.2	1019.2	995.9	989.7
2	1024.2	1013.3	991.7	991.3
3	1030.6	1019.1	997.8	998.3
4	1031.4	1020.6	999.1	1000.5
5	1029.1	1018.3	997.2	998.6
6	1020.6	1010.5	990.0	991.2
7	1008.8	998.1	978.8	979.5
8	989.5	979.5	962.1	962.2
9	965.5	957.6	941.7	940.2
10	956.6	948.2	931.9	923.0

Coolant temperature (K)

	1	2	3	4
1	936.2	930.0	918.0	917.6
2	927.4	921.8	910.8	910.7
3	917.8	912.7	902.7	902.6
4	906.8	902.2	893.4	893.2
5	894.7	890.7	883.1	882.8
6	881.8	878.5	872.2	871.7
7	868.7	866.0	861.0	860.4
8	855.6	853.7	850.0	849.3
9	843.3	842.1	839.7	838.9
10	832.1	831.5	830.4	829.8

Figure 4.4: Fuel (left) and coolant (right) temperature distributions of the equilibrium core at HFP condition

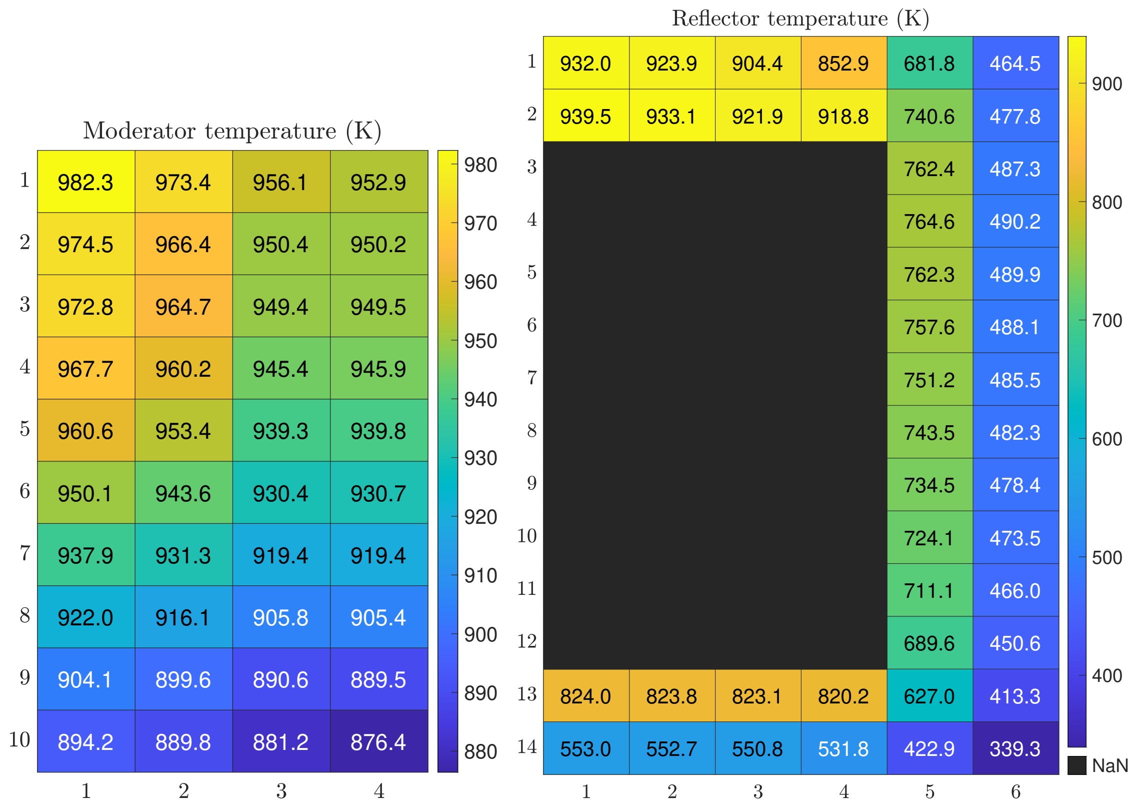

Moderator temperature (K)

	1	2	3	4
1	982.3	973.4	956.1	952.9
2	974.5	966.4	950.4	950.2
3	972.8	964.7	949.4	949.5
4	967.7	960.2	945.4	945.9
5	960.6	953.4	939.3	939.8
6	950.1	943.6	930.4	930.7
7	937.9	931.3	919.4	919.4
8	922.0	916.1	905.8	905.4
9	904.1	899.6	890.6	889.5
10	894.2	889.8	881.2	876.4

Reflector temperature (K)

	1	2	3	4	5	6
1	932.0	923.9	904.4	852.9	681.8	464.5
2	939.5	933.1	921.9	918.8	740.6	477.8
3					762.4	487.3
4					764.6	490.2
5					762.3	489.9
6					757.6	488.1
7					751.2	485.5
8					743.5	482.3
9					734.5	478.4
10					724.1	473.5
11					711.1	466.0
12					689.6	450.6
13	824.0	823.8	823.1	820.2	627.0	413.3
14	553.0	552.7	550.8	531.8	422.9	339.3

Figure 4.5: Moderator (left) and reflector (right) temperature distributions of the equilibrium core at HFP condition

According to Fig. 4.5, the highest moderator temperature (982.3 K) occurs at the outlet of the core centerline, which overlaps with the highest coolant temperature region. The highest reflector temperature (939.5 K) occurs at the region next to the highest coolant temperature region.

4.1.5 Calculation of Local Power

The local power can be calculated from both Serpent and AGREE using the flux and energy release per fission:

$$P_i = \sum_{g=1}^{G} \kappa_i^g \Sigma_{f,i}^g \phi_i^g \quad . \tag{4.1}$$

The radial and axial power profiles calculated by Serpent and AGREE are compared, as plotted in Fig. 4.6. It shows that AGREE and Serpent agree very well on the power distributions. The maximum difference occurs at the boundary of the core, where the neutron leakage is significant.

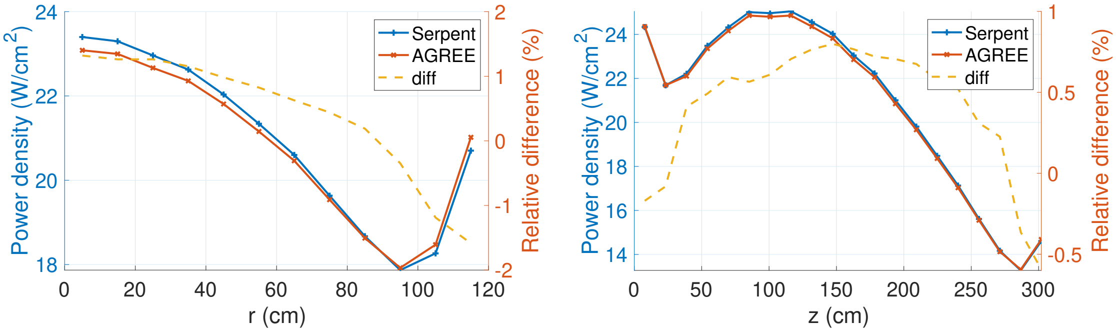

Figure 4.6: Radial (left) and axial (right) power distributions of the equilibrium core

The region-wise power distribution of the gFHR core calculated by AGREE and the relative difference from Serpent results are shown in Fig. 4.7. The average power density is around 20 $\mathrm{W/cm^2}$. The maximum power density occurs at the upper center of the core. The difference between AGREE and Serpent results is less than 1% for most of the core.

4.1.6 Calculation of Region-wise Reactivity Coefficients

The temperature reactivity coefficient is the change of reactivity for a unit change in material temperature:

$$\alpha_T = \frac{\mathrm{d}\rho}{\mathrm{d}T} \quad . \tag{4.2}$$

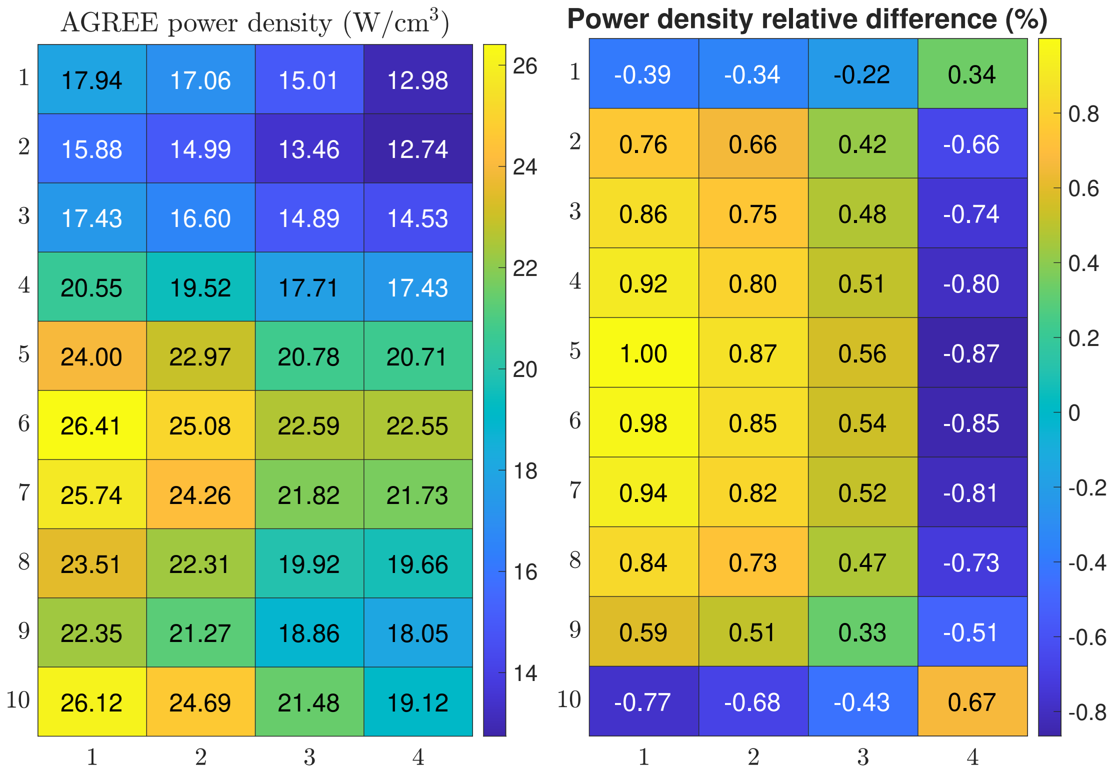

AGREE power density (W/cm^3)

	1	2	3	4
1	17.94	17.06	15.01	12.98
2	15.88	14.99	13.46	12.74
3	17.43	16.60	14.89	14.53
4	20.55	19.52	17.71	17.43
5	24.00	22.97	20.78	20.71
6	26.41	25.08	22.59	22.55
7	25.74	24.26	21.82	21.73
8	23.51	22.31	19.92	19.66
9	22.35	21.27	18.86	18.05
10	26.12	24.69	21.48	19.12

Power density relative difference (%)

	1	2	3	4
1	-0.39	-0.34	-0.22	0.34
2	0.76	0.66	0.42	-0.66
3	0.86	0.75	0.48	-0.74
4	0.92	0.80	0.51	-0.80
5	1.00	0.87	0.56	-0.87
6	0.98	0.85	0.54	-0.85
7	0.94	0.82	0.52	-0.81
8	0.84	0.73	0.47	-0.73
9	0.59	0.51	0.33	-0.51
10	-0.77	-0.68	-0.43	0.67

Figure 4.7: Region-wise power distribution of the gFHR core from AGREE (left) and the relative difference between Serpent and AGREE ($(P_{\text{Serpent}} - P_{\text{AGREE}})/P_{\text{Serpent}}$, right)

The temperature reactivity coefficient is a physical property of the material and therefore different materials have different temperature reactivity coefficients. In the reactor core, the temperature reactivity coefficients of fuel (α_{T_f}), moderator(α_{T_m}), coolant (α_{T_c}) and reflector (α_{T_r}) are typically of most concern for reactor safety analysis.

Since the temperature reactivity coefficients are calculated when the reactor system is at near criticality, i.e., $k_{\text{eff}} \approx 1.0$, Eq. 4.2 can be simplified by

$$\begin{aligned}\alpha_T &= \frac{\mathrm{d}\rho}{\mathrm{d}T} = \frac{\mathrm{d}\left(1-\frac{1}{k_{\text{eff}}}\right)}{\mathrm{d}T} = \frac{1}{k_{\text{eff}}^2}\frac{\mathrm{d}k_{\text{eff}}}{\mathrm{d}T} \\ &\approx \frac{\mathrm{d}k_{\text{eff}}}{\mathrm{d}T} \quad . \end{aligned} \tag{4.3}$$

4.1.6.1 Methods

The temperature reactivity coefficients can be calculated by perturbing the temperature of the corresponding material. In general, there are two ways to perform the calculation:

1. Perturb the temperature in Serpent since the nuclear data libraries are temperature dependent and thus the material temperatures can be specified in Serpent.
2. Generate temperature dependent cross sections first and then perturbing the material temperatures in AGREE. The methods of generating temperature dependent cross sections is called “cross section branching”, which will be introduced in Section 4.2.

Method 1: Direct Subtraction

- Run Serpent at temperature T_1, and get cross section set $\{\Sigma_{T_1}\}$; Run Serpent at temperature T_2, and get cross section set $\{\Sigma_{T_2}\}$.
- Run AGREE with cross section set $\{\Sigma_{T_1}\}$, get $k_{\text{eff},1}$; Run AGREE with cross section set $\{\Sigma_{T_2}\}$, get $k_{\text{eff},2}$.
- Calculate reactivity coefficient:
$$\alpha_T = \frac{k_{\text{eff},1} - k_{\text{eff},2}}{T_1 - T_2}$$

Method 2: Cross section Interpolation

- Run Serpent at temperature T_1, T_2, T_3, $\cdots$, and get cross section set $\{\Sigma_{T_1}\}$, $\{\Sigma_{T_2}\}$, $\{\Sigma_{T_3}\}$, ...

- Interpolate $\{\Sigma_{T_1}\}$, $\{\Sigma_{T_2}\}$, $\{\Sigma_{T_3}\}$, $\cdots$, get temperature-dependent cross section $\{\Sigma(T)\}$.
- Run AGREE at temperature T', get $k_{\text{eff},1}$; Perform a temperature perturbation at T' by ΔT in AGREE, get $k_{\text{eff},1}$.
- Calculate reactivity coefficient:

$$\alpha_T = \frac{k_{\text{eff},1} - k_{\text{eff},2}}{\Delta T}$$

4.1.6.2 Results of lumped reactivity coefficients

The lumped reactivity coefficients of the gFHR core can be calculated with both methods. For the Serpent code, the reactivity coefficients are calculated with Method 1 by perturbing the core temperatures by 100 K (50 K above the nominal temperature and 50 K below the nominal temperature). The nominal temperature is obtained by running AGREE thermo-fluids calculation, as shown in Fig. 4.4 and Fig. 4.5.

For each Serpent run, 500,000 particles are simulated for 100 inactive cycles and 500 active cycles. The standard deviations of Serpent k_{eff} are all between 7 pcm and 9 pcm. The uncertainties of reactivity coefficients calculated by Serpent can be propagated by

$$\Delta_{\alpha_T} = \frac{1}{\Delta T}\sqrt{\Delta^2_{k_{\text{eff},1}} + \Delta^2_{k_{\text{eff},2}}} \quad , \tag{4.4}$$

which are all around $0.12\ \mathrm{pcm/K}$.

Table 4.1: Reactivity coefficients of the gFHR equilibrium core at hot-full-power (HFP)

Reactivity coefficient	Serpent 2 (ref.)	AGREE	Difference (%)
Fuel temperature (pcm/K)	-4.24±0.12	-4.32	-1.9
Coolant temperature (pcm/K)	-1.23±0.12	-1.24	-0.8
Moderator temperature (pcm/K)	-1.07±0.12	-0.92	14.0
Reflector temperature (pcm/K)	+0.99±0.12	+0.85	-14.1

For AGREE code, the lumped reactivity coefficients are calculated with Method 2 with temperature-dependent cross sections. The temperature distribution in the whole core is perturbed by 100 K (50 K above the nominal temperature and 50 K below the nominal temperature).

According to the results in Table 4.1, the temperature reactivity coefficients of fuel, moderator and coolant are all negative, which is significant for the inherent safety of the reactor. However, the temperature reactivity coefficient of reflector is positive, which should be addressed in the reactor safety analysis. The temperature reactivity coefficients of fuel and coolant calculated by Serpent agree well with AGREE results. The differences between the Serpent and AGREE results of other two reactivity coefficients are around 14%, but the differences are still within the allowable range of error.

4.1.6.3 Results of region-wise reactivity coefficients

The region-wise temperature reactivity coefficients of fuel, coolant, moderrator and reflector are calculated based on the Method 2 developed in Section 4.1.6.1. To be noted, in Section 2.4, the gFHR core is discretized into 19 radial regions and 28 axial regions for homogenized cross section generation, in which there are 12×20 fuel regions. The size of each homogenized region is around 10 cm×15 cm, which is relatively very small. For the region-wise temperature reactivity coefficients calculation, a coarser mesh is created by merging 3 radial and 2 axial meshes into one mesh. This is depicted by Fig. 4.8. By merging the meshes, the discretization of the core becomes 7 radial × 14 axial regions, in which there are 4×10 fuel regions.

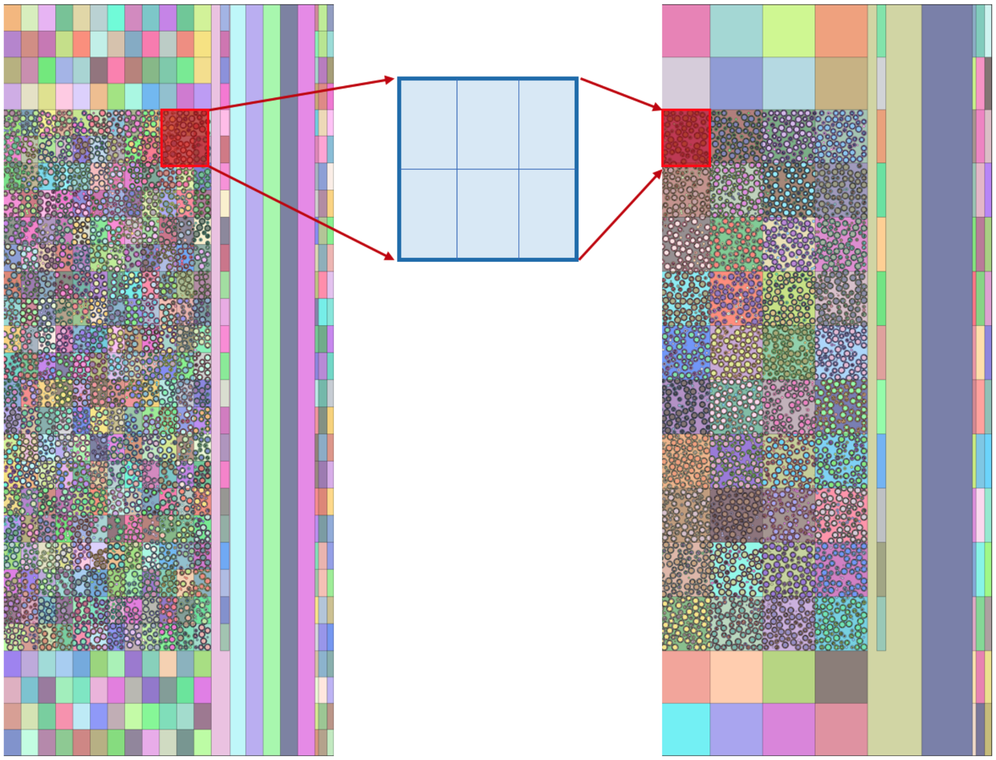

Fig. 4.8: gFHR coarse mesh for region-wise reactivity coefficients calculation

There are several reasons to use a coarser mesh for temperature reactivity coefficients calculation:

1. The region-wise temperature reactivity coefficients are calculated by perturbing the regional material temperature by 50 K above the nominal temperature and 50 K below the nominal

temperature. If the region is too small, the eigenvalue change caused by the temperature perturbation will not be noticeable enough and a large uncertainty will be resulted.

2. In the SAM gFHR model, a four-channel core will be modeled since the runtime of SAM code increases significantly when the number of channels is large. The coarse mesh shown in Fig. 4.8 is compatible to the SAM model.
3. In the gFHR benchmark specification document[46], the active core is discretized into 4×10 fuel regions, which is the same as the coarse mesh in Fig. 4.8.

Fig. 4.9 and Fig. 4.10 show the region-wise temperature reactivity coefficients of fuel, coolant, moderator and reflector, respectively. According to Fig. 4.9 and Fig. 4.10, the temperature reactivity coefficients of fuel, coolant and moderator are negative in all the fuel regions, while the temperature reactivity coefficients of reflector are positive in all the reflector regions. The negative fuel temperature reactivity coefficient and the negative coolant temperature reactivity coefficient are relatively easy to explain: the fuel coefficient is negative due to Doppler broadening, while the coolant coefficient is negative due to density changes. It is worth noting the temperature reactivity coefficient of the moderator and the temperature reactivity coefficient of the reflector: even though both the moderator and the reflector are made of graphite, their reactivity temperature coefficients have opposite signs. This is because, for the moderator, an increase in temperature leads to a hardening of the neutron energy spectrum in the active region, resulting in reduced reactivity. On the other hand, for the reflector, an increase in temperature causes an increase in the elastic scattering cross-section of graphite[48], thereby reflecting more neutrons back into the core. The maximum region-wise temperature reactivity coefficients of fuel, coolant and moderator in absolute value all occur at the center of the third radial core channel.

In Section 4.1.6.2, the whole core temperature reactivity coefficients are calculated by perturbing the temperature distributions of the whole core. On the other side, the whole core temperature reactivity coefficients can be calculated by summing up the region-wise ones. The whole core temperature reactivity coefficients obtained from both methods are summerized in Table 4.2. The differences between the results are all below 5%, which shows that the temperature reactivity coefficients calculated from both methods are consistent with each other.

4.2 Uncertainty in Branch Cross Section Generation

The methods of generating temperature-dependent and control rod-dependent cross sections from Serpent cases are generally referred to as cross section branching. The methodology is described in GenPMAXS theory manual[49], but a brief overreview of the methods will be provided in this section.

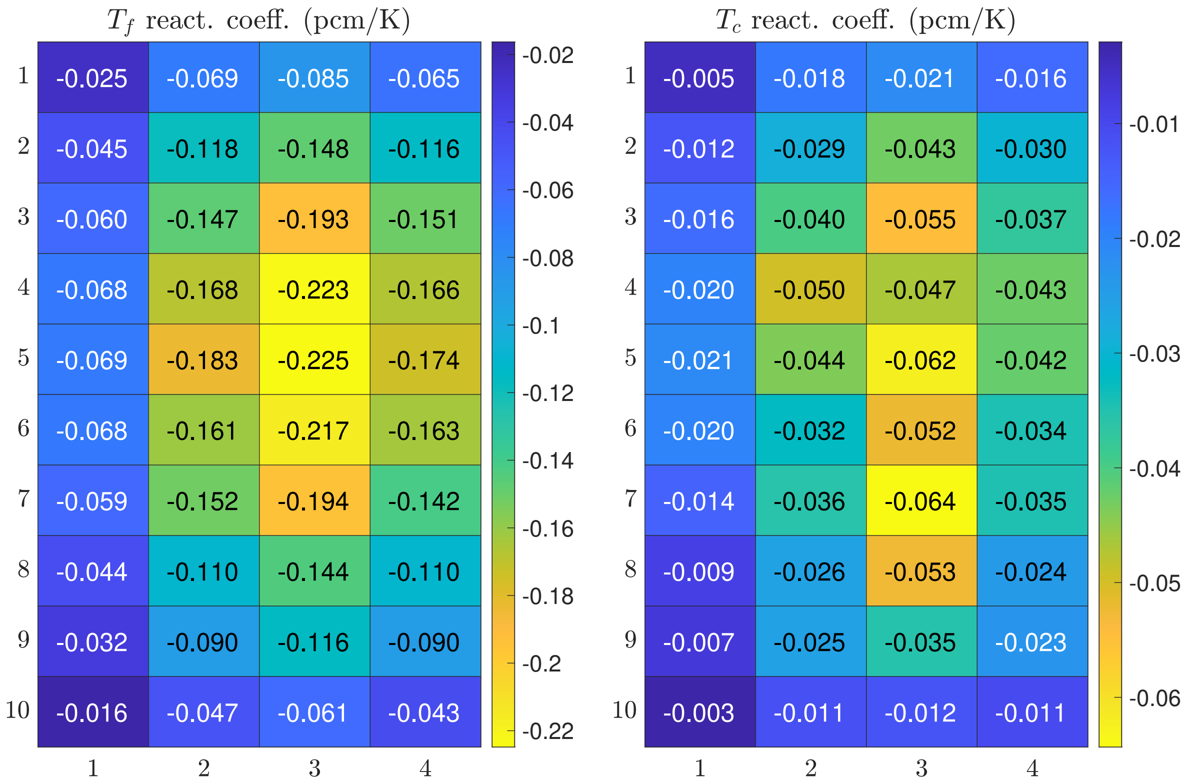

Figure 4.9: Fuel (left) and coolant (right) temperature reactivity coefficients of gFHR

Table 4.2: Whole core reactivity coefficients of the gFHR from two methods

Reactivity coefficient	AGREE lumped	AGREE region-wise sum	Difference (%)
Fuel temperature (pcm/K)	-4.324	-4.320	0.1
Coolant temperature (pcm/K)	-1.239	-1.235	0.3
Moderator temperature (pcm/K)	-0.918	-0.897	2.3
Reflector temperature (pcm/K)	+0.852	+0.888	4.2

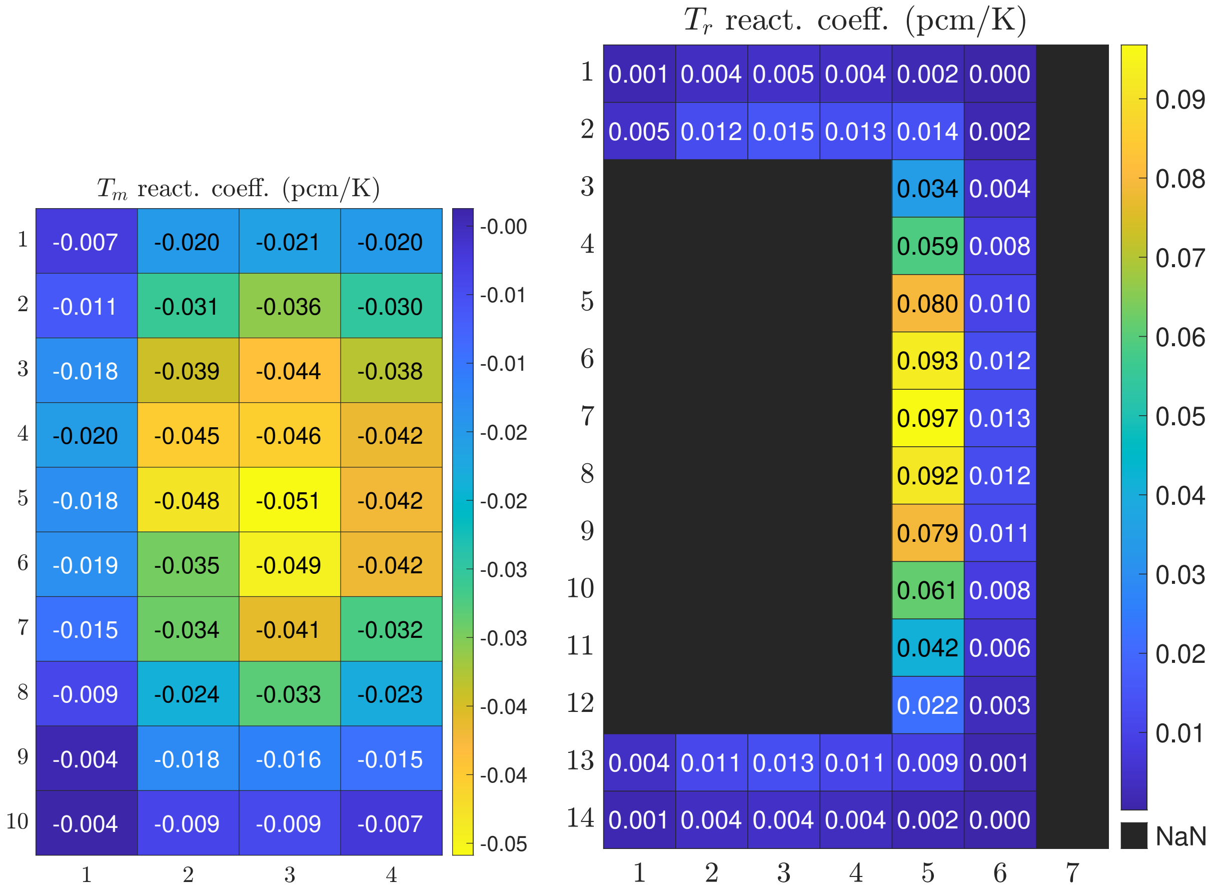

	1	2	3	4
1	-0.007	-0.020	-0.021	-0.020
2	-0.011	-0.031	-0.036	-0.030
3	-0.018	-0.039	-0.044	-0.038
4	-0.020	-0.045	-0.046	-0.042
5	-0.018	-0.048	-0.051	-0.042
6	-0.019	-0.035	-0.049	-0.042
7	-0.015	-0.034	-0.041	-0.032
8	-0.009	-0.024	-0.033	-0.023
9	-0.004	-0.018	-0.016	-0.015
10	-0.004	-0.009	-0.009	-0.007

	1	2	3	4	5	6	7
1	0.001	0.004	0.005	0.004	0.002	0.000	
2	0.005	0.012	0.015	0.013	0.014	0.002	
3					0.034	0.004	
4					0.059	0.008	
5					0.080	0.010	
6					0.093	0.012	
7					0.097	0.013	
8					0.092	0.012	
9					0.079	0.011	
10					0.061	0.008	
11					0.042	0.006	
12					0.022	0.003	
13	0.004	0.011	0.013	0.011	0.009	0.001	
14	0.001	0.004	0.004	0.004	0.002	0.000	

Figure 4.10: Moderator (left) and reflector (right) temperature reactivity coefficients of gFHR

4.2.1 Cross Section Interpolation

The cross section at a certain temperature is obtained by interpolating in AGREE. The cross section interpolation is performed using Eq. (4.5):

$$\Sigma_x^T = \mathcal{D}(T - T_{ref}) + \Sigma_x^{T_{ref}} \quad , \tag{4.5}$$

where T_{ref} is the temperature of the reference branch. $\mathcal{D}$ is defined as:

$$\mathcal{D} = w_l \mathcal{D}_l + w_h \mathcal{D}_h \quad , \tag{4.6}$$

where $\mathcal{D}_l$ and $\mathcal{D}_h$ are the two closest partial derivatives of the cross section with respect to the material temperature, w_l and w_h are the weights of the two partial derivatives. They are calculated by GenPMAXS based on Serpent generated cross section data using following formulas:

$$\mathcal{D}_l = \left.\frac{\partial \Sigma_x}{\partial T}\right|_{T_l} = \frac{\Sigma_x^{T_l} - \Sigma_x^{T_{ref}}}{T_l - T_{ref}} \quad , \tag{4.7}$$

$$\mathcal{D}_h = \left.\frac{\partial \Sigma_x}{\partial T}\right|_{T_h} = \frac{\Sigma_x^{T_h} - \Sigma_x^{T_{ref}}}{T_h - T_{ref}} \quad . \tag{4.8}$$

The weights are determined by

$$w_l = \frac{T - T_l}{T_h - T_l} \quad , \tag{4.9}$$

$$w_h = \frac{T_h - T}{T_h - T_l} = 1 - w_l \quad . \tag{4.10}$$

Fig. 4.5 is a demonstration of how the absorption cross section of a reflector region at 500 K is interpolated. There are five branches used for the interpolation, including one reference branch and four reflector temperature branches. The reference branch is at 900 K. The closest two branches to 500 K are at 294 K and 615.9 K.

4.2.2 Cross Section Branches

In the gFHR simulations, the branches for fuel temperature, moderator temperature, coolant temperature, reflector temperature and control rod fraction are considered. The cross section at a certainty state (T_f, T_m, T_c, T_r, control rod position) can be obtained by doing multi-dimensional interpolation. A two dimensional interpolation case is depicted in Fig. 4.12.

It should be noted that for the moderator temperature, coolant temperature and reflector temperature branches, the partial derivatives are with respect to the temperatures. However, for the

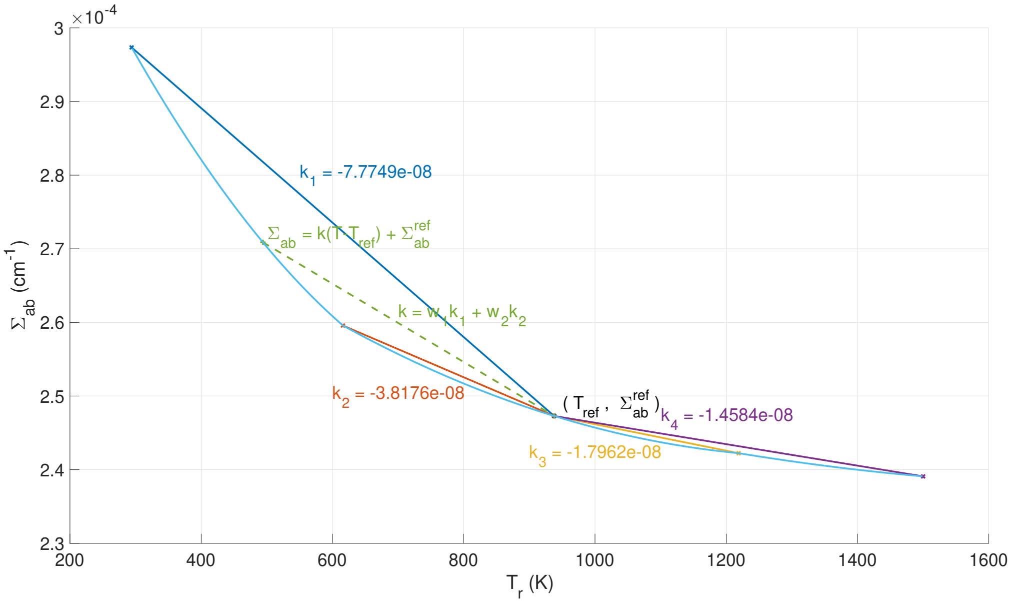

Fig. 4.11: Demonstration of the cross section interpolation in AGREE

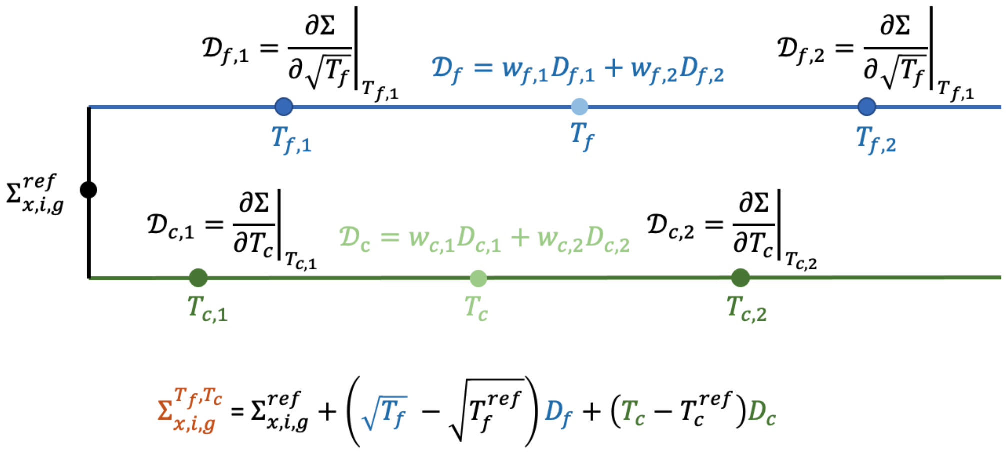

Fig. 4.12: Illustration of a two-dimensional cross section interpolation case

fuel temperature branches, the partial derivatives are with respect to the square root of the fuel temperature since it more accurately describes the physics of the fuel temperature doppler effect, i.e.,

$$\mathcal{D}_{T_f} = \frac{\partial \Sigma_x}{\partial \sqrt{T_f}} \quad . \tag{4.11}$$

4.2.3 Evaluation of Cross Section Interpolation Error

In most cases, five branches are used to generate the temperature dependent cross sections for a certain material. For example, when generating the fuel temperature dependent cross sections, T_f^{low}, $T_f^{\text{mid-low}}$, T_f^{ref}, $T_f^{\text{mid-high}}$ and T_f^{high} are used as fuel temperature branches, where

- T_f^{ref} is the nominal fuel temperature;
- T_f^{low} is the lowest possible fuel temperature, which is equal to the fluoride salt freezing temperature;
- T_f^{high} is the highest possible temperature in the simulation, which is 1500 K;
- $T_f^{\text{mid-low}} = \frac{1}{2}(T_f^{\text{low}} + T_f^{\text{ref}})$;
- $T_f^{\text{mid-high}} = \frac{1}{2}(T_f^{\text{high}} + T_f^{\text{ref}})$.

Since the temperature range is from 300 K to 1500 K, it means the spacing for fuel temperature interpolating is 300 K, which is somewhat sparse. However, the interpolation with 300 K spacing can actually give very accurate results. This will be illustrated by a study of evaluating the interpolation error.

The study is motivated by the cross section interpolation error introduced in reactor safety analysis codes using reactivity coefficients. The methods for the reactivity interpolation error were previously discussed in [50].

4.2.3.1 Grid Spacing

In the research performed here, the cross sections for temperature interpolation are generated using a Monte Carlo code. The idea for evaluating the interpolation error is similar to the method used for reactivity coefficients with a deterministic code. Here a sparse grid and a dense grid are used to interpolate the $\nu\Sigma_f$ cross section for the fuel temperature range from 300 K to 1500 K. For the sparse grid, the grid spacing is 300 K, which means there are 5 branches as the reference points. While for the dense grid, the grid spacing is 40 K, which means there are 31 branches as

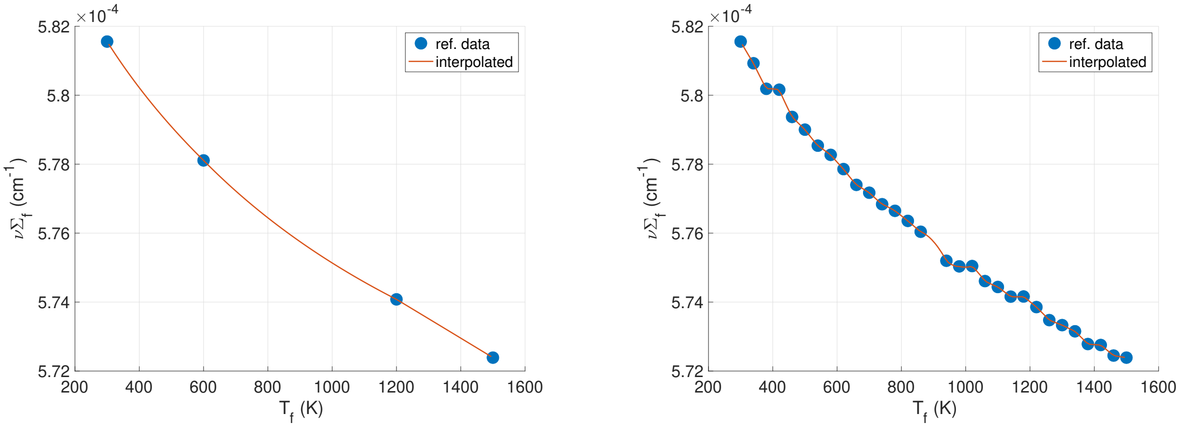

(a) $h = 300$ K (5-branch) (b) $h = 40$ K (31-branch)

Fig. 4.13: MC XS interpolation for different grid spacing

the reference points. The cross section is interpolated for the fuel temperatures every 5 K. The interpolation results are shown in Fig. 4.13.

To evaluate the accuracy of the interpolations, the "true" cross sections at the interpolated temperature points (every 5 K) are generated using Serpent code. The "true" value of the cross section and the standard deviation are shown in Fig. 4.14.

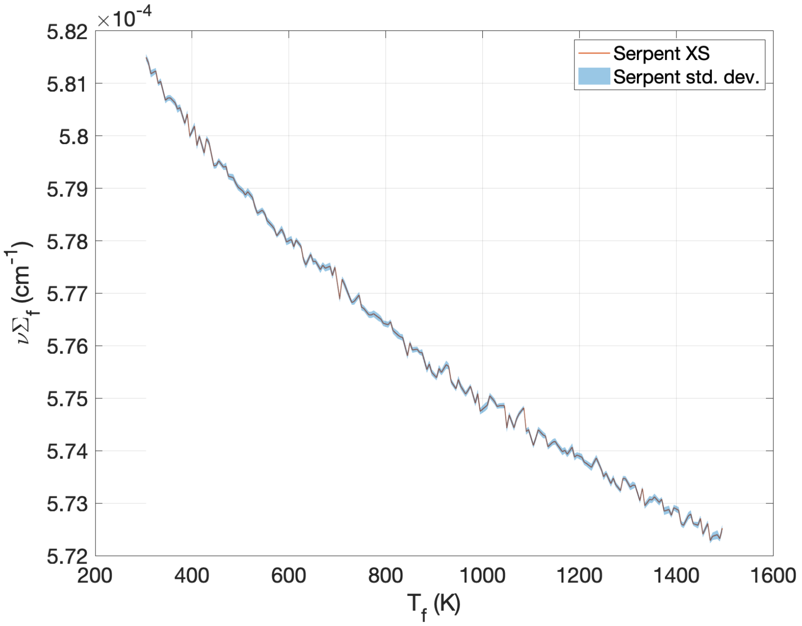

Fig. 4.14: Serpent generated $\nu\Sigma_f$ XS with standard deviation

The interpolation error is obtained by comparing the interpolated value with the "true" value.

The error of the interpolation is shown in Fig. 4.13. The interpolation error is converted to $\Delta_{k_{\text{eff}}}/k_{\text{eff}}$ in the unit of pcm by applying Eq. 3.15. It shows that the interpolation errors are on the same order of magnitude even the grid spacings are different.

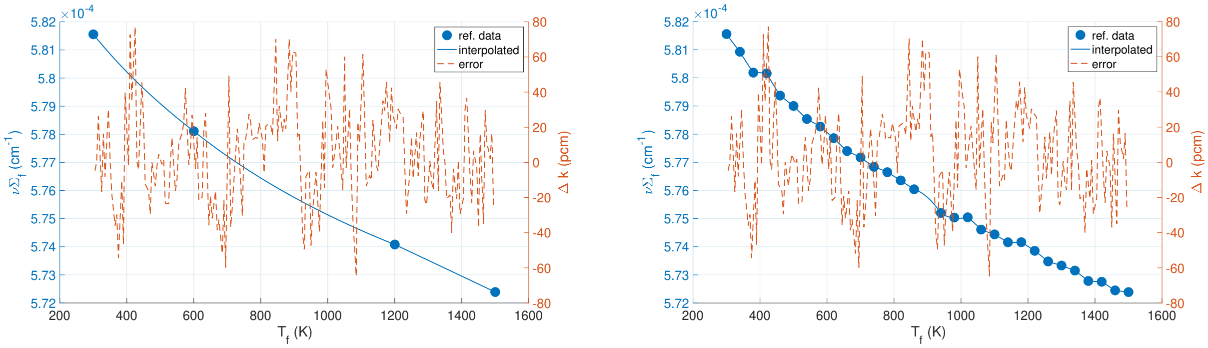

(a) $h = 300$ K (5-branch)

(b) $h = 40$ K (31-branch)

Fig. 4.15: MC XS interpolation error for different grid spacing

Using additional grid spacings ($h = 240\ \text{K},\ 200\ \text{K},\ 80\ \text{K},\ 20\ \text{K}$) to do the cross section interpolation and calculating the root mean square (RMS) of the interpolation error, the results are plotted in Fig. 4.16. Both the x-axis and y-axis are in logarithmic scale. It shows that when the grid spacing is decreasing from 300 K to 20 K, the RMS of interpolation error keeps at the same order of magnitude ($\sim 1.0 \times 10^{-7}\ \text{cm}^{-1}$). Therefore, using dense grid (or more reference data points) does not improve the accuracy of cross section interpolation.

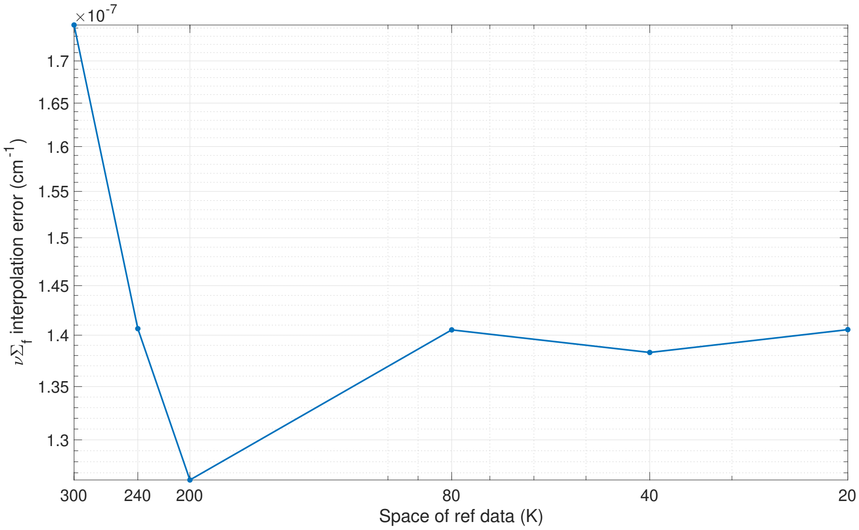

Fig. 4.16: MC XS interpolative error for $\nu\Sigma_f$ XS with different grid spacing

4.2.3.2 Number of Neutron Histories

When generating the cross sections with Serpent in the above study, 100,000 neutrons are simulated in 100 inactive cycles and 500 active cycles. The standard deviation of the $\nu\Sigma_f$ cross section is around 10^{-7} cm^{-1}, i.e., the relative standard deviation is around 0.02%. The accuracy of cross section data can be improved by adding the number of neutron histories in Monte Carlo simulation. Therefore, the number of neutron histories is increased by 10 times for generating the reference data points and the "true" values. The results are shown in Fig. 4.17.

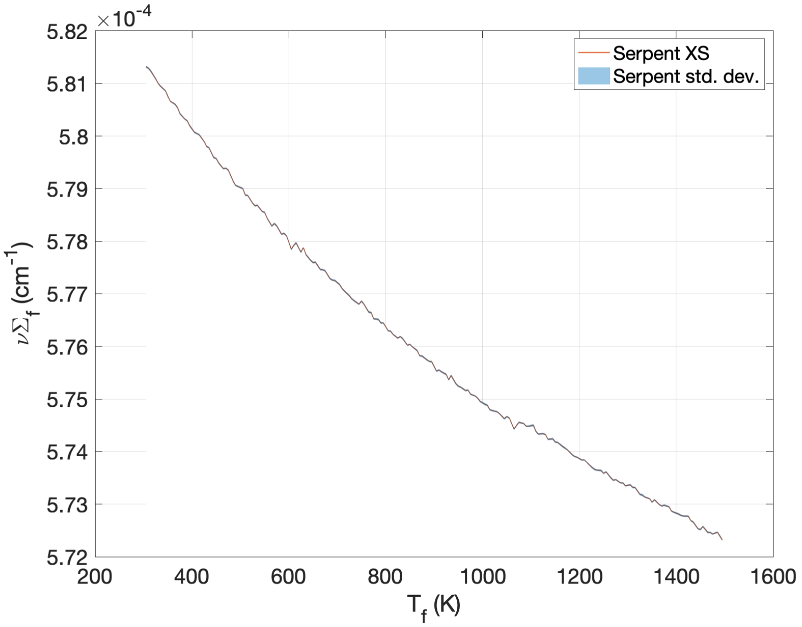

Fig. 4.17: Serpent generated $\nu\Sigma_f$ XS with standard deviation

The standard deviation of the $\nu\Sigma_f$ cross section is reduced to around 4×10^{-8} cm^{-1}, i.e., the relative standard deviation is around 0.007%. The standard deviation of $\nu\Sigma_f$ is reduced by a factor of ~ 3, which is expected since the error of Monte Carlo calculation is inversely proportional to the square root of the number of neutron histories.

Using the new cross section data, the interpolation error for different interpolating grid spacings is calculated again. The RMS of the interpolation error is plotted in Fig. 4.18. It can be observed that the order of magnitude of the error becomes smaller compared to the results in Fig. 4.16. However, there is no benefit to refining the temperature interval to give interpolation error below the cross section standard deviation.

Comparing the results in Fig. 4.16 and Fig. 4.16, the key information is summarized in Table 4.3.

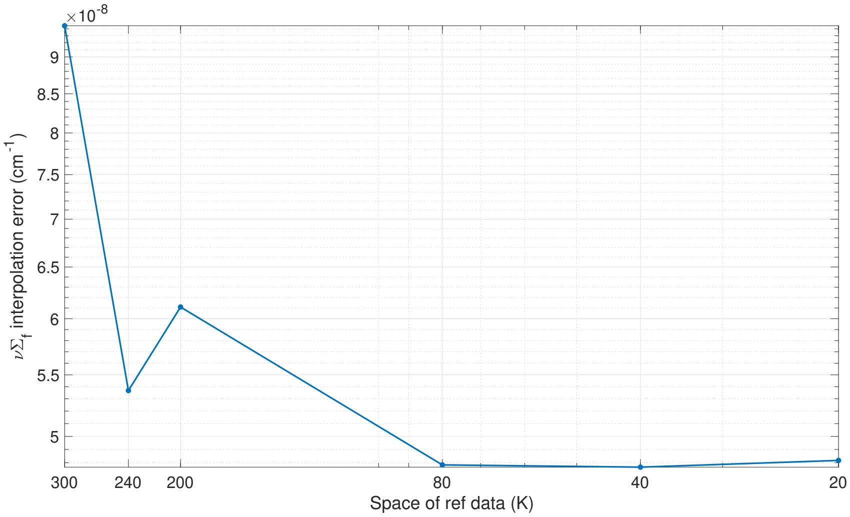

Fig. 4.18: MC XS interpolative error for $\nu\Sigma_f$ XS with different grid spacings, 10 times more neutron histories

Table 4.3: MC number of histories, MC std. dev. and interpolative error

Number of MC histories	MC std.dev. of $\nu\Sigma_f$	RMS of interp. err.
100,000$\times$ 500	$\sim 1 \times 10^{-7}$	$\sim 1.4 \times 10^{-7}$
1,000,000$\times$ 500	$\sim 4 \times 10^{-8}$	$\sim 5 \times 10^{-8}$

4.2.3.3 Summary

Based on the study of interpolation error presented in Section 4.2.3.1 and Section 4.2.3.2, the following conclusions can be drawn:

1. Increasing the number of branches (reference data points) can reduce the interpolation error, but only when grid is very sparse. Therefore, using five branches for temperature dependent cross section interpolation in this thesis is accurate enough.
2. Increasing the number of histories when generating Monte Carlo cross sections can reduce the interpolative error.

4.3 Uncertainty Analysis for the Local Power

4.3.1 Uncertainty of the MC Generated Cross Section Data

The local power in AGREE is calculated using Eq. 4.12. As indicated, the results of the analytic and stochastic methods are similar which provides confidence in using the stochastic method for a wider range of responses than the restrictive use of CPT analytic methods for only the core k_{eff} , where the energy release per fission ($\kappa\Sigma_f$) data is used. Therefore, the uncertainty of $\kappa\Sigma_f$ is required for the uncertainty analysis of the local power. Since κ and Σ_f are reported by Serpent separately, the uncertainty of $\kappa\Sigma_f$ is propagated by

$$\Delta_{\kappa\Sigma_f} = \kappa\Sigma_f \cdot \sqrt{\left(\frac{\Delta_\kappa}{\kappa}\right)^2 + \left(\frac{\Delta_{\Sigma_f}}{\Sigma_f}\right)^2} \quad , \tag{4.12}$$

where $\frac{\Delta_\kappa}{\kappa}$ and $\frac{\Delta_{\Sigma_f}}{\Sigma_f}$ are relative uncertainties and their values are provided in Serpent output directly. Eq. (4.12) is implemented in GenPMAXS.

Except for $\nu\Sigma_f$, other cross section data, including χ, Σ_{tr}, Σ_{ab}, $\nu\Sigma_f$ and Σ_t, are also taken into account for the uncertainty analysis of the local power. The uncertainties of these cross section data are reported by Serpent directly and therefore they are converted to PMAX format by GenPMAXS directly without further processing.

4.3.2 Calculation Scheme

The calculation scheme is depicted in Fig. 4.19. The cross section data and their uncertainties are processed by GenPMAXS and are converted into PMAX format. Then Dakota generates a number of samples by randomly sampling based on the cross section and uncertainty data. The samples are processed by an input processor to generate a set of AGREE cases. All the cases are run by AGREE and the outputs are collected by an output processor. The values of interested responses are extracted from the output files for Dakota. Finally, Dakota calculates the standard deviation of the interested responses by gathering statistics, which are the uncertainties of the interested responses due to the uncertainty of MC generated cross section data.

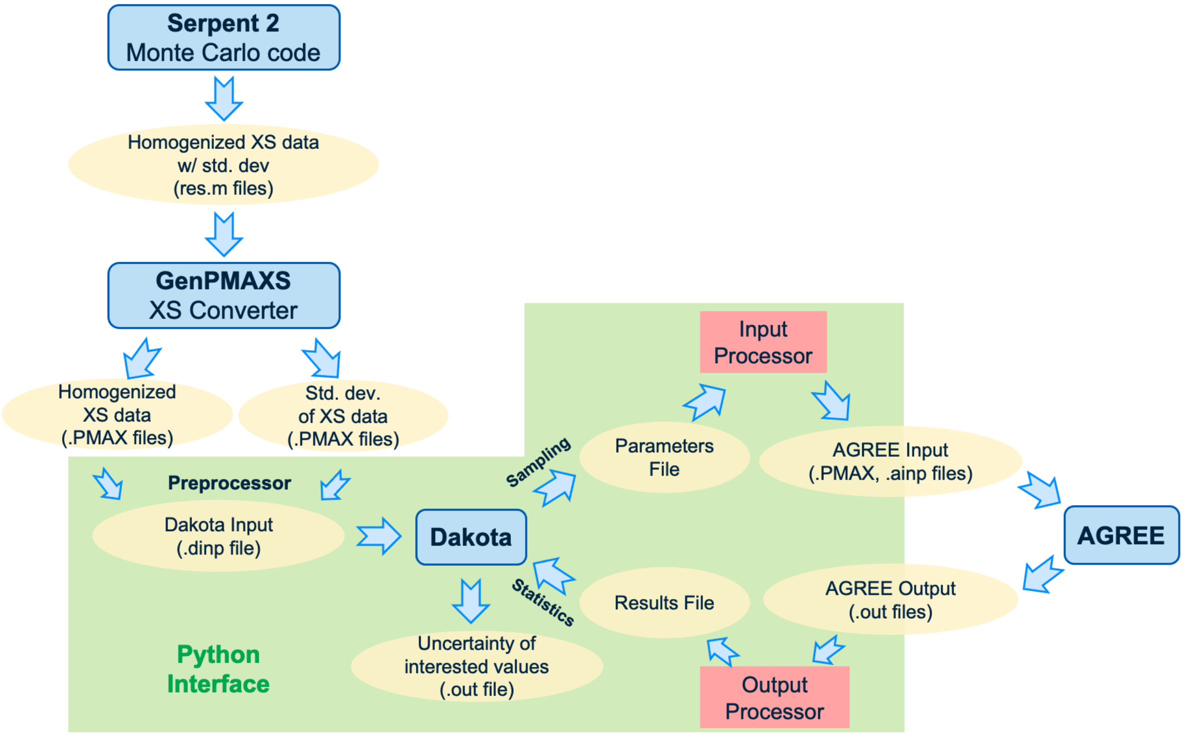

Fig. 4.19: Coupling scheme of AGREE and Dakota for uncertainty calculation

4.3.3 Results

Applying the calculation scheme described above, the uncertainties of the gFHR core power distribution are calculated. The contributions from the branch cross sections are taken into consideration. When generating the branch cross sections, 500,000 particles are simulated for 500 active cycles (100 inactive cycles) in Serpent. The cross section types generated for fuel regions and non-fuel regions are different. Table 4.4 lists the cross section data whose uncertainties are considered in the local power uncertainty calculation.

The uncertainties of the gFHR core local power are shown in Fig. 4.20, along with the power density distribution. In the axial direction, the uncertainties in the central regions are smaller than those in the peripheral regions. Since the neutron flux in the central region is higher, the uncertainty of the cross section data is smaller. Thus the uncertainty of local power is smaller. In the radial

Table 4.4: Cross section data contributed to the power distribution uncertainties

Region type	Cross section	Derivatives
Fuel region	χ	No derivatives
	$\Sigma_{tr}, \Sigma_{ab}, \Sigma_s, \nu\Sigma_f$	$\frac{\partial}{\partial\sqrt{T_f}}, \frac{\partial}{\partial T_c}, \frac{\partial}{\partial T_m}, \frac{\partial}{\partial T_r}$
Non-fuel region	$\Sigma_{tr}, \Sigma_{ab}, \Sigma_s$	$\frac{\partial}{\partial\sqrt{T_f}}, \frac{\partial}{\partial T_c}, \frac{\partial}{\partial T_m}, \frac{\partial}{\partial T_r}$

direction, the uncertainties in the center regions are larger than those in the outer regions. Since the volume of the homogenized region in the central is higher, the uncertainty of the cross section data is smaller. Thus the uncertainty of local power in the outer region is smaller.

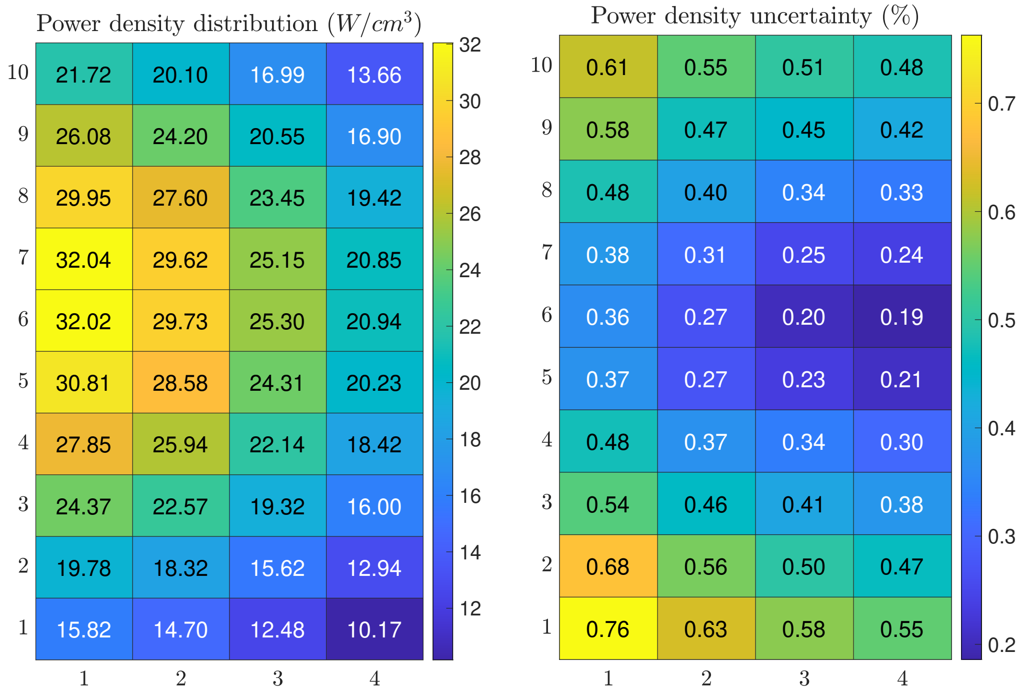

	1	2	3	4
10	21.72	20.10	16.99	13.66
9	26.08	24.20	20.55	16.90
8	29.95	27.60	23.45	19.42
7	32.04	29.62	25.15	20.85
6	32.02	29.73	25.30	20.94
5	30.81	28.58	24.31	20.23
4	27.85	25.94	22.14	18.42
3	24.37	22.57	19.32	16.00
2	19.78	18.32	15.62	12.94
1	15.82	14.70	12.48	10.17

(a) Power density

	1	2	3	4
10	0.61	0.55	0.51	0.48
9	0.58	0.47	0.45	0.42
8	0.48	0.40	0.34	0.33
7	0.38	0.31	0.25	0.24
6	0.36	0.27	0.20	0.19
5	0.37	0.27	0.23	0.21
4	0.48	0.37	0.34	0.30
3	0.54	0.46	0.41	0.38
2	0.68	0.56	0.50	0.47
1	0.76	0.63	0.58	0.55

(b) Relative uncertainty of local power

Fig. 4.20: gFHR core power density distribution and relative uncertainty

The noteworthy results from Fig. 4.20 are summerized into Table 4.5.

Table 4.5: The relative uncertainty of gFHR core power density

Mean P_i (W/cm^3)	RMS of $\frac{\Delta_{P_i}}{P_i}$ (%)	Max of $\frac{\Delta_{P_i}}{P_i}$ (%)	Min of $\frac{\Delta_{P_i}}{P_i}$ (%)
21.92	0.44	0.76	0.19

4.4 Uncertainty Analysis of Reactivity Coefficients

4.4.1 Uncertainty Analysis for the Total Core Reactivity Coefficients

The core total temperature reactivity coefficients are calculated with Method 1 (Section 4.1.6.1). The uncertainty can be calculated by

$$\Delta_{\alpha_T} = \frac{1}{2\Delta T}\sqrt{\Delta^2_{k_{\text{eff},1}} + \Delta^2_{k_{\text{eff},2}}} \tag{4.13}$$

The methods for the calculation of the uncertainty of k_{eff} is introduced in Chapter 3. Applying the random sampling methods to calculate $\Delta_{k_{\text{eff},1}}$ and $\Delta_{k_{\text{eff},2}}$, the uncertainty of the lumped temperature reactivity coefficients can be calculated subsequently using Eq. 4.13. The uncertainties of k_{eff} are all in a range of 23 pcm to 28 pcm. Therefore, the uncertainties of the reactivity coefficients are all in a range of 32 pcm to 40 pcm. The uncertainties and the relative value to the reactivity coefficients are listed in Table 4.6. It shows that the absolute values of the uncertainty are on the same level, but the relative value varies a lot because of the varying of the reactivity coefficients values. The fuel temperature reactivity coefficients has the smallest relative uncertainty while the reflector temperature reactivity coefficients has the largest relative uncertainty. Since the absolute values of the uncertainty are nearly the same, the larger the reactivity coefficient is, the smaller the relative uncertainty becomes.

Table 4.6: Uncertainty of lumped temperature reactivity coefficients of the gFHR

Reactivity coefficient	AGREE (lumped)	Uncertainty	Relative (%)
Fuel temperature (pcm/K)	-4.324	0.367	8.7
Moderator temperature (pcm/K)	-0.918	0.344	37.5
Coolant temperature (pcm/K)	-1.239	0.373	30.5
Reflector temperature (pcm/K)	+0.852	0.365	44.3

4.4.2 Uncertainty Analysis for the Region-wise Reactivity Coefficients

4.4.2.1 Uncertainty of MC Generated Cross Section Data

The region-wise temperature reactivity coefficients are calculated with Method 2. To calculate the uncertainty of region-wise temperature reactivity coefficients, the uncertainty of temperature-dependent cross sections must be evaluated properly first.

In the gFHR neutronics calculation, the cross section data include χ, Σ_{ab}, Σ_{tr}, $\nu\Sigma_f$ and Σ_s. The fission spectrum χ is independent of the material temperatures. So there are no derivatives calculated for χ. For other cross sections, the derivative of every branch is calculated:

$$\mathcal{D}_{x,i,g,br} = \left.\frac{\partial \Sigma_{x,i,g}}{\partial T}\right|_{T_{br}} = \frac{\Sigma_{x,i,g}^{T_{br}} - \Sigma_{x,i,g}^{T_{ref}}}{T_{br} - T_{ref}} \quad , \qquad \text{for } T_{br} = T_m, T_c \text{ or } T_r \quad ; \tag{4.14}$$

$$\mathcal{D}_{x,i,g,br} = \left.\frac{\partial \Sigma_{x,i,g}}{\partial \sqrt{T}}\right|_{T_{br}} = \frac{\Sigma_{x,i,g}^{T_{br}} - \Sigma_{x,i,g}^{T_{ref}}}{\sqrt{T_{br}} - \sqrt{T_{ref}}} \quad , \qquad \text{for } T_{br} = T_f \quad . \tag{4.15}$$

where x, i, g, br represent cross section type, homogenized region ID, group ID and branch ID, respectively.

According to Eq. (4.14) and Eq. (4.15), the uncertainty of the derivative data can be propagated from the uncertainty of $\Sigma_{x,i,g}^{T_{br}}$ and $\Sigma_{x,i,g}^{T_{ref}}$:

$$\Delta_{\mathcal{D}_{x,i,g,br}} = \frac{1}{|T_{br} - T_{ref}|}\sqrt{\Delta^2_{\Sigma_{x,i,g}^{T_{br}}} + \Delta^2_{\Sigma_{x,i,g}^{T_{ref}}}} \quad , \qquad \text{for } T_{br} = T_m, T_c \text{ or } T_r \quad ; \tag{4.16}$$

$$\Delta_{\mathcal{D}_{x,i,g,br}} = \frac{1}{\left|\sqrt{T_{br}} - \sqrt{T_{ref}}\right|}\sqrt{\Delta^2_{\Sigma_{x,i,g}^{T_{br}}} + \Delta^2_{\Sigma_{x,i,g}^{T_{ref}}}} \quad , \qquad \text{for } T_{br} = T_f \quad . \tag{4.17}$$

The uncertainties of branch cross section data, including the cross sections and the derivatives, are preprocessed by GenPMAXS code and output to PMAX files.

4.4.2.2 Calculation Scheme

The algorithm for calculating the uncertainty of region-wise reactivity is shown in Fig. 4.21, which is similar to Fig. 4.19. There are three modifications compared to the coupling scheme for calculating the uncertainty of local power:

1. The derivatives of the cross section data and their uncertainties are considered when generate PMAX files, since temperature-dependent cross sections are utilized in region-wise reactivity calculation. Eq. (4.16) and Eq. (4.17) are implemented in GenPMAXS to obtain the uncertainties of the cross section derivatives.
2. A driver script is developed in Python for calculating all the region-wise reactivity coefficients.
3. The input and output files for the Python driver are generated and processed by the input and output processors.

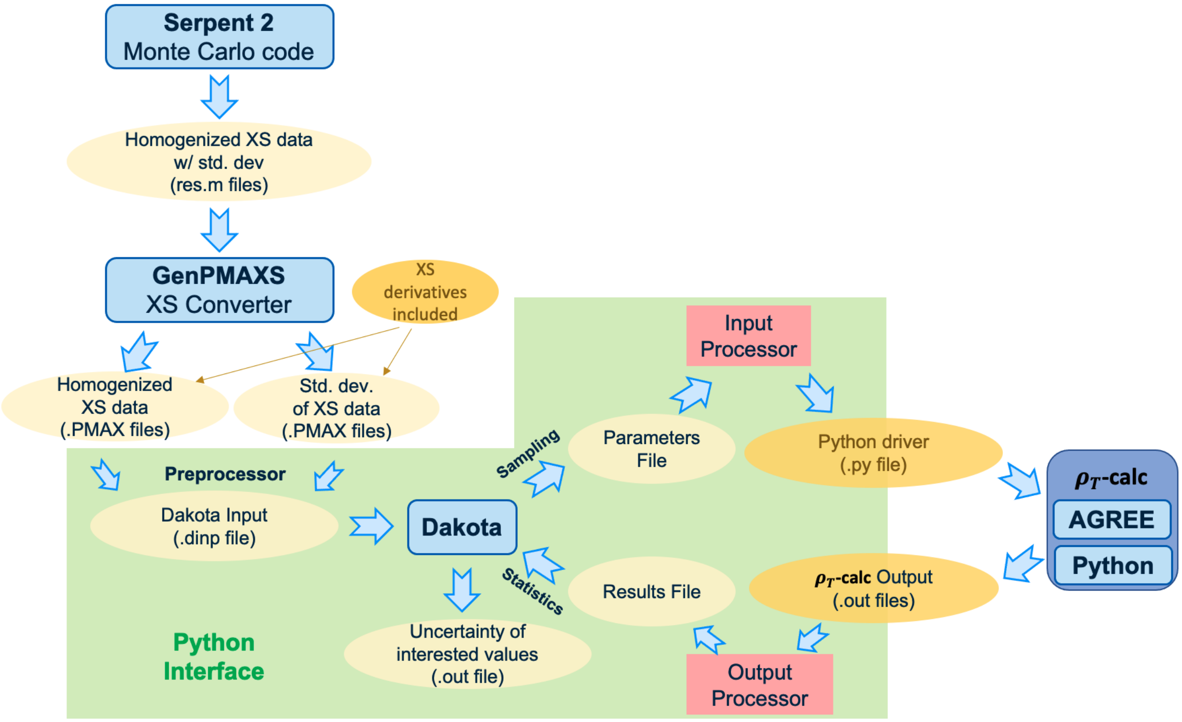

Fig. 4.21: Coupling scheme for calculating the uncertainty of region-wise reactivity coefficients

4.4.2.3 Results

Applying the calculation scheme developed above, the relative uncertainties of the region-wise temperature reactivity coefficients (Fig. 4.9 and Fig. 4.10) are calculated. The branch cross sections are generated by Serpent with simulating 500,000 particles for 500 active cycles (100 inactive cycles). The types of cross sections and their derivatives taken into account for the uncertainty calculation are the same as those in local power uncertainty calculation, which are listed in Table 4.4. The results are shown in Fig. 4.22 to Fig. 4.25, along with the region-wise temperature reactivity coefficients for comparison.

Fig. 4.22 shows that the relative uncertainties of the fuel temperature reactivity coefficients in most regions are smaller than 10%. However, the uncertainties in the centerline regions (Radial Channel 1) and at the bottom regions are higher than 10%. The largest uncertainty occurs at the bottom of the centerline, which is as high as 33.1%. Comparing the relative uncertainty distribution with the reactivity coefficient distribution, it can be observed that the uncertainty of the regions that the reactivity coefficients are larger are smaller, and vice versa.

For the uncertainties of coolant and moderator temperature reactivity coefficients shown in Fig. 4.23 and Fig. 4.24, the similar distributions can be observed, except that the uncertainties of α_{T_c} and α_{T_m} are larger than the uncertainties of α_{T_f}. The reason is that absolute values of the uncertainty are on the same level, however, the values of α_{T_c} and α_{T_m} are smaller than the values

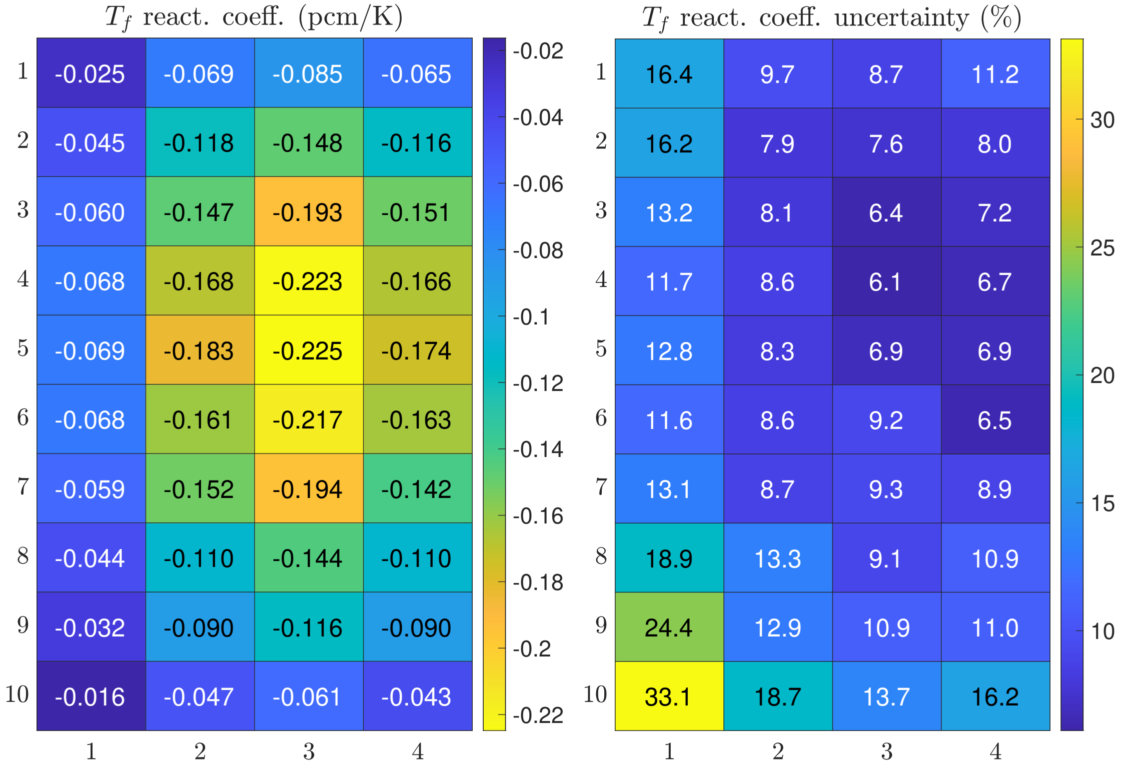

	1	2	3	4
1	-0.025	-0.069	-0.085	-0.065
2	-0.045	-0.118	-0.148	-0.116
3	-0.060	-0.147	-0.193	-0.151
4	-0.068	-0.168	-0.223	-0.166
5	-0.069	-0.183	-0.225	-0.174
6	-0.068	-0.161	-0.217	-0.163
7	-0.059	-0.152	-0.194	-0.142
8	-0.044	-0.110	-0.144	-0.110
9	-0.032	-0.090	-0.116	-0.090
10	-0.016	-0.047	-0.061	-0.043

	1	2	3	4
1	16.4	9.7	8.7	11.2
2	16.2	7.9	7.6	8.0
3	13.2	8.1	6.4	7.2
4	11.7	8.6	6.1	6.7
5	12.8	8.3	6.9	6.9
6	11.6	8.6	9.2	6.5
7	13.1	8.7	9.3	8.9
8	18.9	13.3	9.1	10.9
9	24.4	12.9	10.9	11.0
10	33.1	18.7	13.7	16.2

Figure 4.22: Region-wise α_{T_f} and the relative uncertainty

of α_{T_f}. Therefore, the relative uncertainties of α_{T_c} and α_{T_m} become larger.

For the uncerainties of reflector temperature reactivity coefficients, Fig. 4.25 shows that they are smaller than that of α_{T_f}, α_{T_c} and α_{T_m}. The uncertainties of α_{T_r} in most of the regions are smaller than 5%. The largest uncertainties occur at the outer region of the top and bottom reflectors, which are over 60%. However, these large uncertainties will not affect subsequent simulations, since the reactivity coefficients at those regions are very small (less than 0.001 $\mathrm{pcm/K}$).

The noteworthy data in Fig. 4.22 to Fig. 4.25 are summarized in Table 4.7.

Table 4.7: The relative uncertainty of gFHR core region-wise temperature reactivity coefficients

Reactivity Coefficient	Mean of α_T $(\mathrm{pcm/K})$	Mean of $\frac{\Delta_{\alpha_T}}{\alpha_T}$ (%)	RMS of $\frac{\Delta_{\alpha_T}}{\alpha_T}$ (%)	Max of $\frac{\Delta_{\alpha_T}}{\alpha_T}$ (%)	Min of $\frac{\Delta_{\alpha_T}}{\alpha_T}$ (%)
α_{T_f}	-0.108	11.4	12.6	33.1	6.1
α_{T_c}	-0.031	41.4	52.6	197.1	13.6
α_{T_m}	-0.022	29.5	35.6	102.6	13.0
α_{T_r}	+0.022	8.2	16.5	74.0	0.3

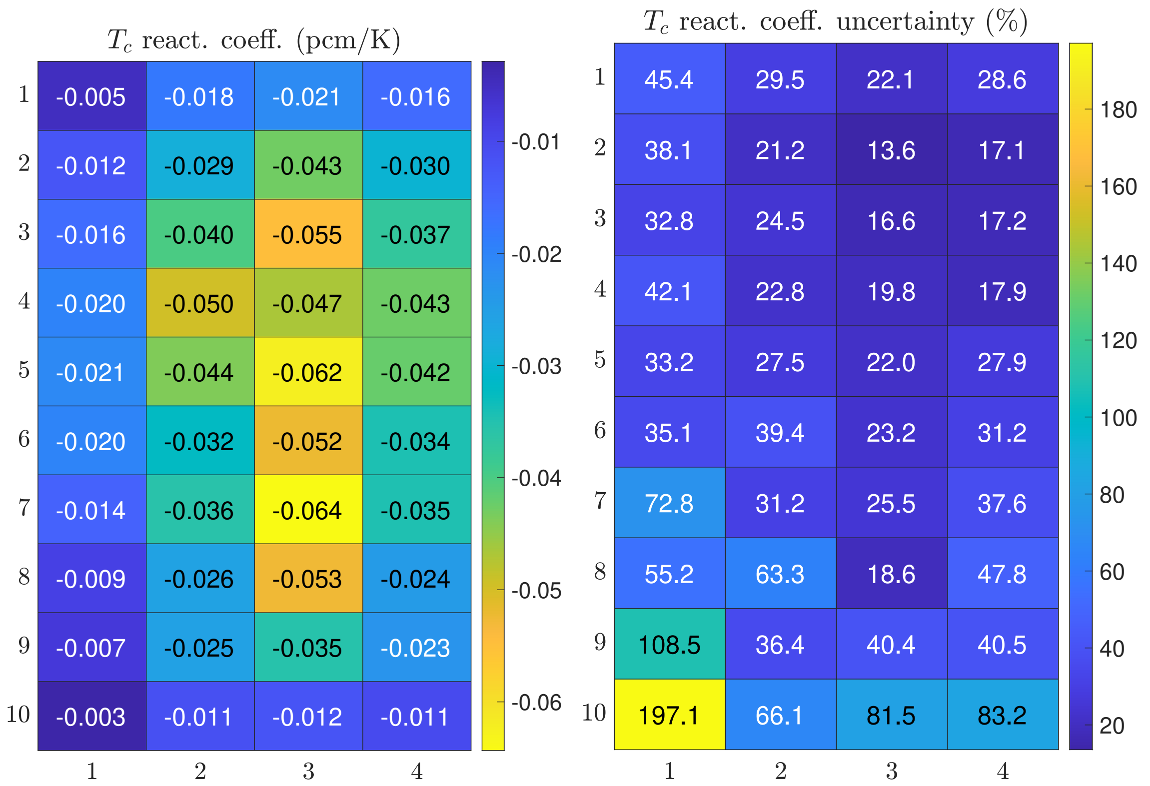
T_c react. coeff. (pcm/K)

	1	2	3	4
1	-0.005	-0.018	-0.021	-0.016
2	-0.012	-0.029	-0.043	-0.030
3	-0.016	-0.040	-0.055	-0.037
4	-0.020	-0.050	-0.047	-0.043
5	-0.021	-0.044	-0.062	-0.042
6	-0.020	-0.032	-0.052	-0.034
7	-0.014	-0.036	-0.064	-0.035
8	-0.009	-0.026	-0.053	-0.024
9	-0.007	-0.025	-0.035	-0.023
10	-0.003	-0.011	-0.012	-0.011

T_c react. coeff. uncertainty (%)

	1	2	3	4
1	45.4	29.5	22.1	28.6
2	38.1	21.2	13.6	17.1
3	32.8	24.5	16.6	17.2
4	42.1	22.8	19.8	17.9
5	33.2	27.5	22.0	27.9
6	35.1	39.4	23.2	31.2
7	72.8	31.2	25.5	37.6
8	55.2	63.3	18.6	47.8
9	108.5	36.4	40.4	40.5
10	197.1	66.1	81.5	83.2

Figure 4.23: Region-wise α_{T_c} and the relative uncertainty

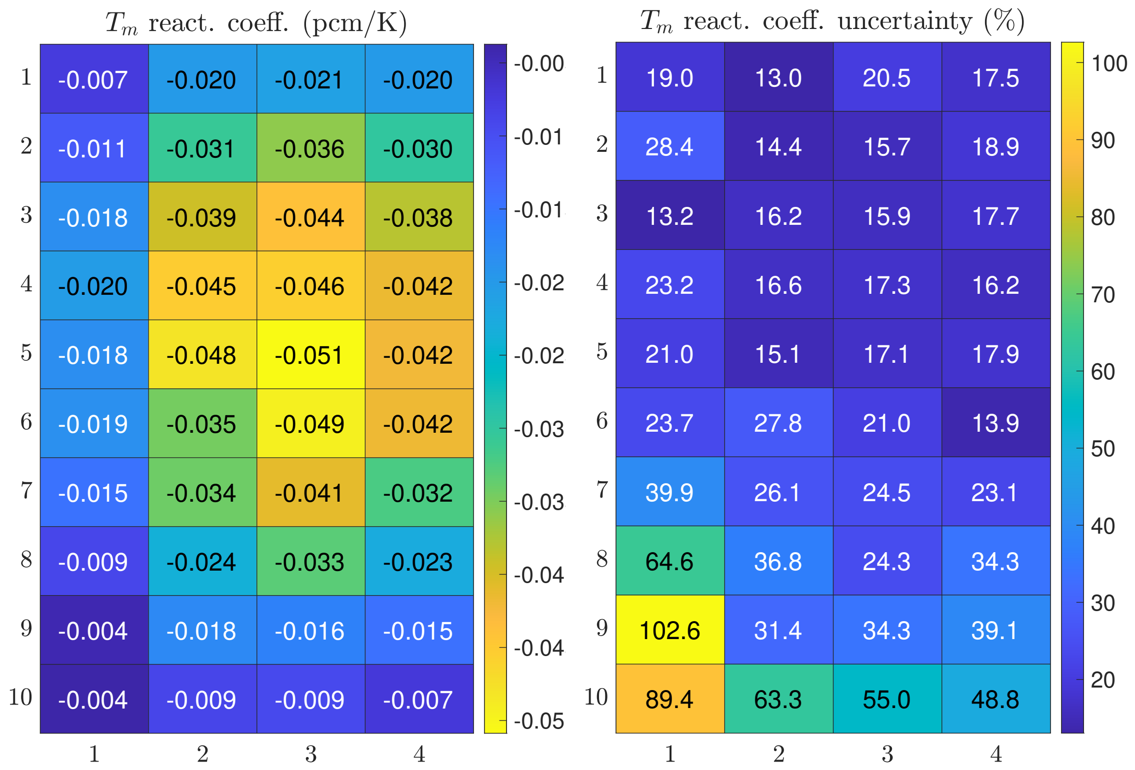
T_m react. coeff. (pcm/K)

	1	2	3	4
1	-0.007	-0.020	-0.021	-0.020
2	-0.011	-0.031	-0.036	-0.030
3	-0.018	-0.039	-0.044	-0.038
4	-0.020	-0.045	-0.046	-0.042
5	-0.018	-0.048	-0.051	-0.042
6	-0.019	-0.035	-0.049	-0.042
7	-0.015	-0.034	-0.041	-0.032
8	-0.009	-0.024	-0.033	-0.023
9	-0.004	-0.018	-0.016	-0.015
10	-0.004	-0.009	-0.009	-0.007

T_m react. coeff. uncertainty (%)

	1	2	3	4
1	19.0	13.0	20.5	17.5
2	28.4	14.4	15.7	18.9
3	13.2	16.2	15.9	17.7
4	23.2	16.6	17.3	16.2
5	21.0	15.1	17.1	17.9
6	23.7	27.8	21.0	13.9
7	39.9	26.1	24.5	23.1
8	64.6	36.8	24.3	34.3
9	102.6	31.4	34.3	39.1
10	89.4	63.3	55.0	48.8

Figure 4.24: Region-wise α_{T_m} and the relative uncertainty

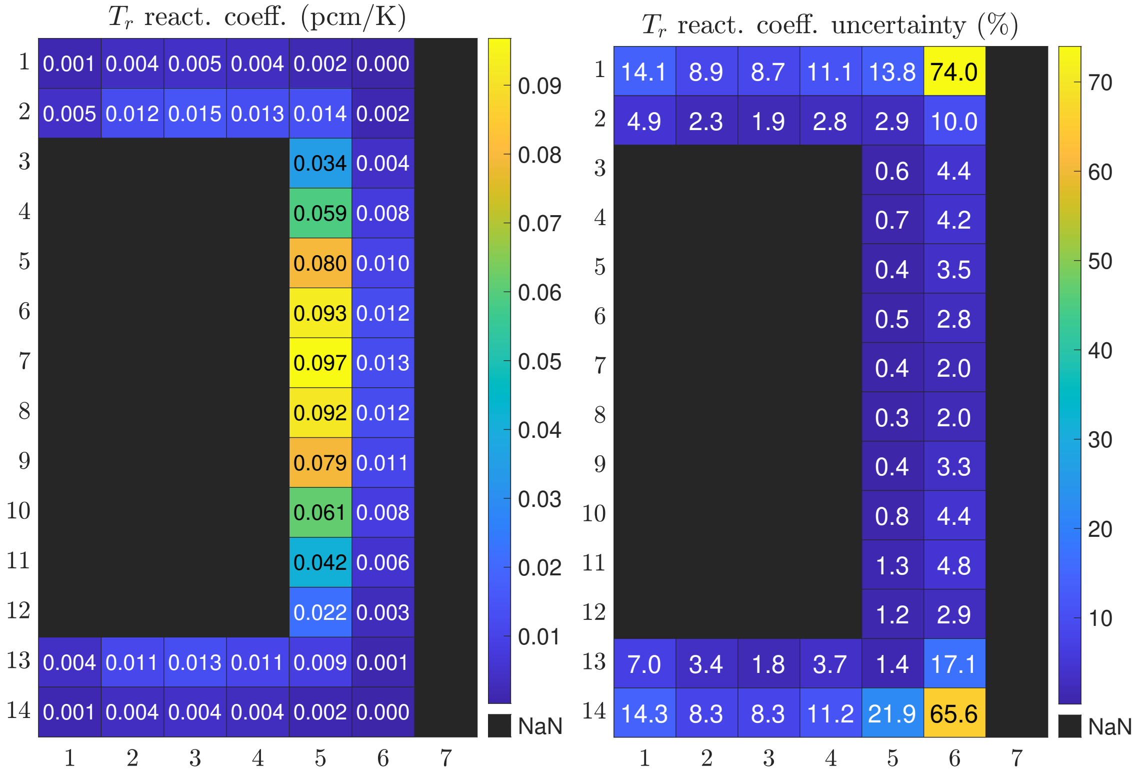

T_r react. coeff. (pcm/K)

	1	2	3	4	5	6	7
1	0.001	0.004	0.005	0.004	0.002	0.000	
2	0.005	0.012	0.015	0.013	0.014	0.002	
3					0.034	0.004	
4					0.059	0.008	
5					0.080	0.010	
6					0.093	0.012	
7					0.097	0.013	
8					0.092	0.012	
9					0.079	0.011	
10					0.061	0.008	
11					0.042	0.006	
12					0.022	0.003	
13	0.004	0.011	0.013	0.011	0.009	0.001	
14	0.001	0.004	0.004	0.004	0.002	0.000	

T_r react. coeff. uncertainty (%)

	1	2	3	4	5	6	7
1	14.1	8.9	8.7	11.1	13.8	74.0	
2	4.9	2.3	1.9	2.8	2.9	10.0	
3					0.6	4.4	
4					0.7	4.2	
5					0.4	3.5	
6					0.5	2.8	
7					0.4	2.0	
8					0.3	2.0	
9					0.4	3.3	
10					0.8	4.4	
11					1.3	4.8	
12					1.2	2.9	
13	7.0	3.4	1.8	3.7	1.4	17.1	
14	14.3	8.3	8.3	11.2	21.9	65.6	

Figure 4.25: Region-wise α_{T_r} and the relative uncertainty

4.4.3 Correlations between Region-wise Neutronics Parameters

The uncertainties of the local power and region-wise reactivity coefficients, as well as the correlations between them are calculated by AGREE-Dakota. The correlation matrix is shown in Fig. 4.26.

As indicated in Fig. 4.26, the correlations within local power and within the reflector temperature reactivity coefficients are strong. The local power and the region-wise reflector temperature reactivity coefficients are mildly correlated, however, the correlations between other parameters are negligible. The correlation matrix will be applied to propagate the uncertainty of neutronics parameters to SAM transient simulations in Chapter 5.

4.5 Uncertainty Analysis for SAM Steady-State Results

4.5.1 SAM Model of gFHR

A SAM model was developed for the gFHR reactor based on the generic Pebble-Bed Fluoride-salt-cooled High-temperature Reactor (PB-FHR) primary loop model developed by ANL[9]. The SAM generic PB-FHR model is mainly created based on the UC Berkeley Mk1 FHR design as

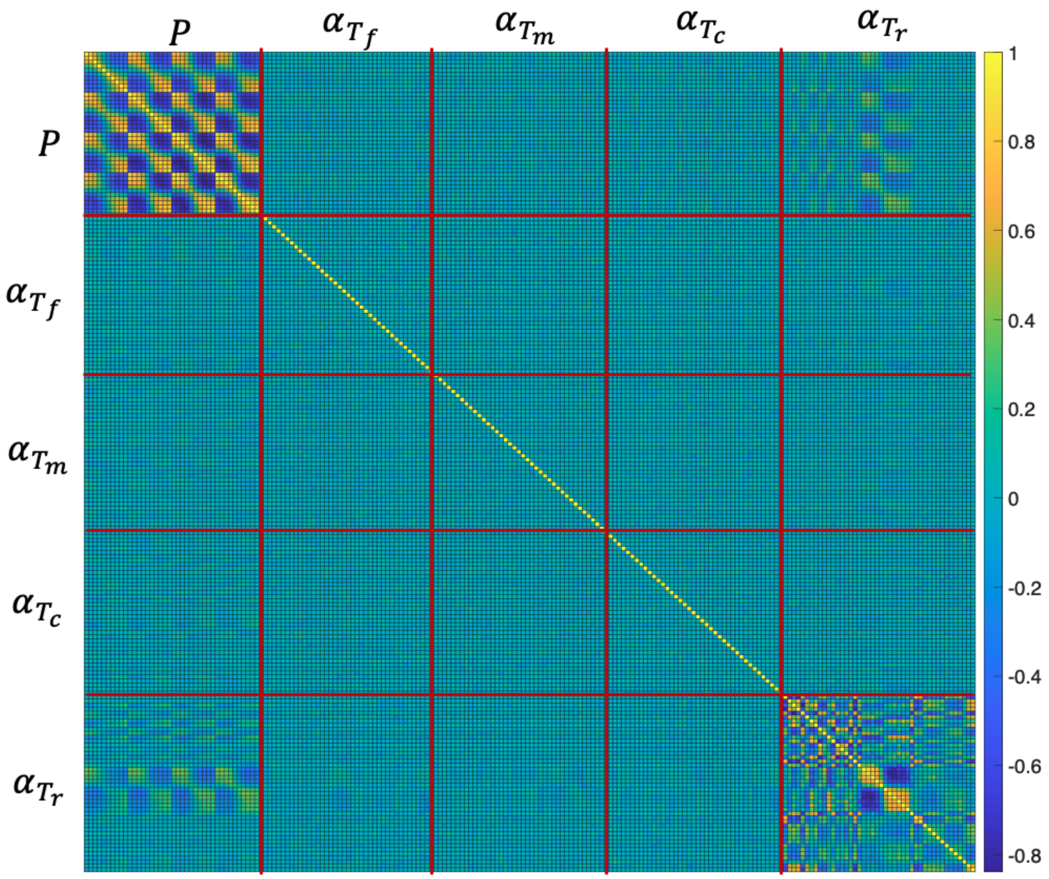

Fig. 4.26: Correlation matrix between the local power and region-wise reactivity coefficients

well as some features from Kairos Power's KP-FHR design.

A 3D-1D flow coupling scheme is applied for modeling the PB-FHR core and the primary loop. The reactor core is modeled in 3-D with the active pebble-bed core, fueling chute, defueling chute, expansion section, contraction section and the reflectors, while the primary loop is modeled in 1-D. The model is shown in Fig. 4.1. The 3-D and 1-D model are coupled by exchanging the boundary condition data at the inlet and outlet of the core (Location 1 and Location 2 in Fig. 4.1). The flow velocity or the mass flow rate, the flow temperature and pressure are transferred at the inlet and outlet.

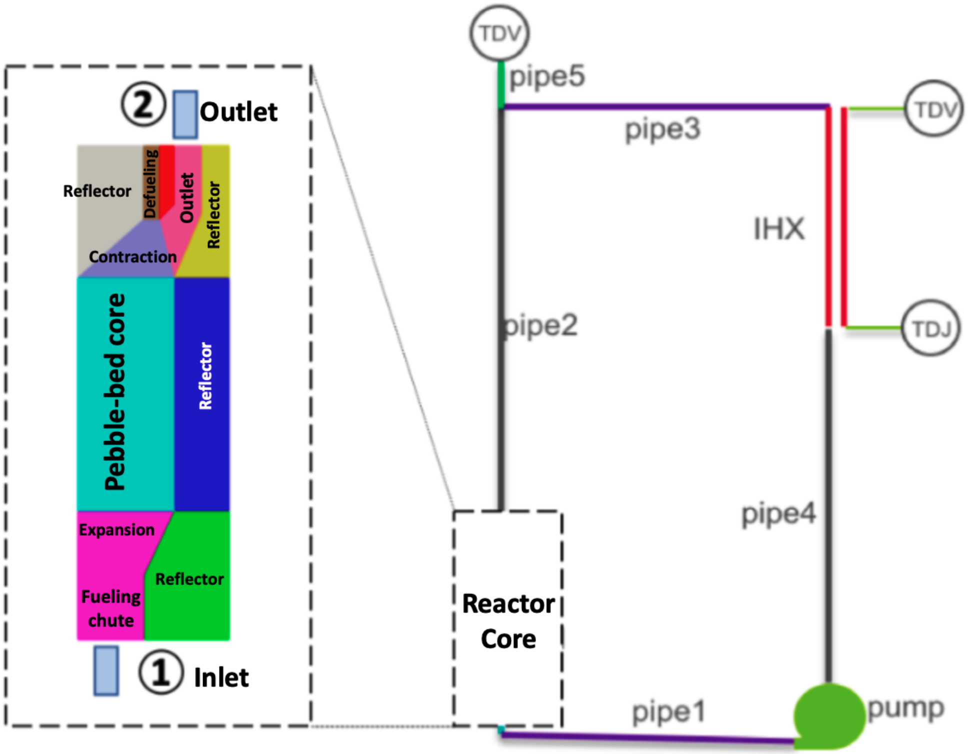

Fig. 4.27: SAM 3D-1D flow coupling model of generic PB-FHR

For the gFHR benchmark problem, the reactor is simplified by removing the fueling and defueling chute, expansion and contraction section, only keeping the active pebble-bed core and graphite reflector. Here the generic PB-FHR SAM model is adapted for the gFHR modeling by replace the pebble-bed core with the gFHR active core parameters. This is depicted by Fig. 4.28. The reactor core is modeled with porous media a approach and the average porosity is 0.4. The heat source in the core is represented by specifying a power shape function.

In this study, both a single-channel core model and a multi-channel core model are created. For the single-channel core model, the core is represented by an vertical pebble-bed channel with 10 axial nodes. The radial power distribution is integrated into one value at each axial position. For

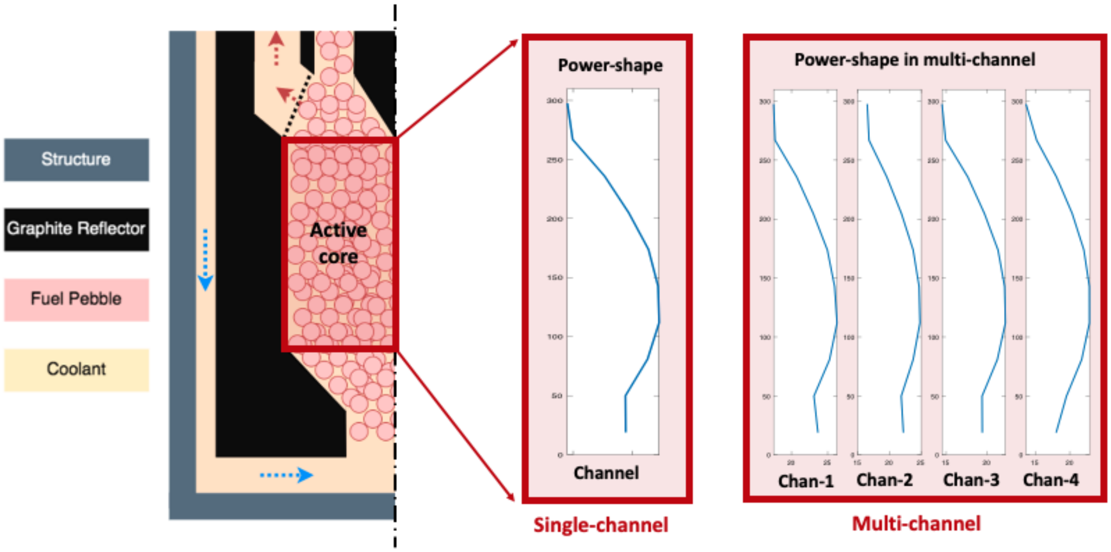

Fig. 4.28: SAM gFHR model with single-channel core and multi-channel core

the multi-channel core model, the core is represented by 4 vertical channels, which is consistent with the 4×10 model shown in Fig. 4.8. The power distribution shown in Fig. 4.7 is specified as the power shape function after normalization.

To be noted, in the multi-channel core model, the four channels have different flow areas and power fractions. The flow area fractions and the power fractions of the four channels are listed in Table 4.8. The flow area fractions are calculated based on the channel volumes, while the power fractions are calculated based on the power density distribution and the channel volumes. The fuel pebble packing fraction is assumed to be uniformly 60% in the core, which neglects the local non-uniformity caused by the Monte Carlo generated pebble locations. The assumption is reasonable since the channels are large enough and the local non-uniformity can be averaged.

Table 4.8: Flow area fraction and power fraction of the SAM multi-channel core model

Channel number	1	2	3	4
Flow area fraction (%)	6.25	18.75	31.25	43.75
Power fraction (%)	8.14	22.64	32.10	37.11

4.5.2 SAM Steady-state Results

4.5.2.1 SAM Single-channel Core Model

For the single-channel SAM model, the axial temperature distribution of fuel and coolant are shown in Fig. 4.29. The results calculated by AGREE are plotted on the same figure for comparison. For the AGREE results, the temperature of each node is the average temperature of the node; while for the SAM results, the temperatures are the temperatures at the boundaries of each node. So there are 10 temperature points on the AGREE result curves while there are 11 points on the SAM result curves.

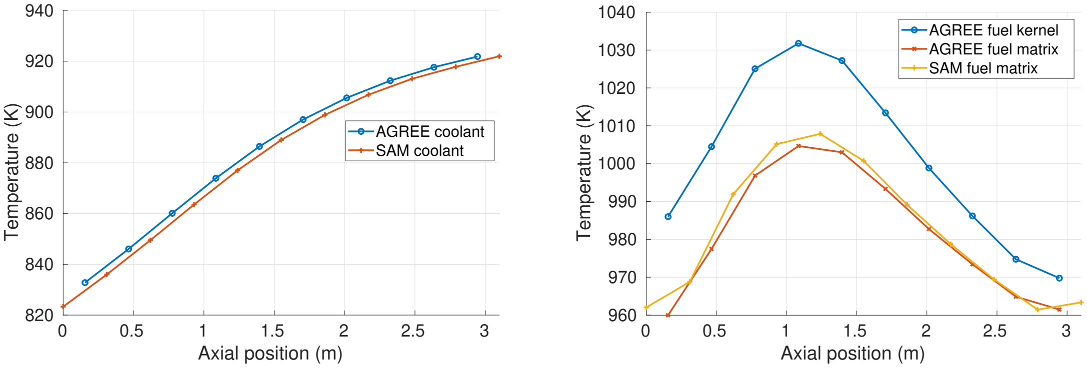

Figure 4.29: The axial T_c (left) and T_f (right) of gFHR SAM single channel model

For the coolant temperature, SAM results and AGREE results are consistent with each other. The differences between SAM and AGREE are below 3 K for all the axial nodes.

For the fuel temperature, the fuel matrix temperatures calculated by SAM AGREE well with AGREE. The maximum difference between SAM and AGREE results is smaller than 10 K. The differences at the bottom and the top of the core are larger than that at the center of the core. The maximum fuel matrix temperature is around 1010 K, which occurs at the lower center of the reactor. The highest temperature point of the fuel corresponds to the location of maximum power density. Except for the fuel matrix temperature, the fuel kernel temperature is also calculated by assuming that the temperature difference between the kernel and the matrix is proportional to the power density.

4.5.2.2 SAM Multi-channel Core Model

In the SAM multi-channel core model, there are four vertical channels. The axial temperature distributions of fuel and coolant for the four channels are shown in Fig. 4.30.

For the coolant temperature, the inlet temperatures are the same for the all four channels. The outlet temperatures are different since the power fractions of the channels are different. The maximum coolant temperature is 949.4 K, which occurs at the outlet of Channel 1 (the inner-most channel).

For the fuel temperature, the axial shapes of the fuel temperature for the four channels are similar. The maximum fuel temperature points of the four channels are at the same axial position. The maximum fuel temperature is 1049.8 K, which is at the lower center of Channel 1.

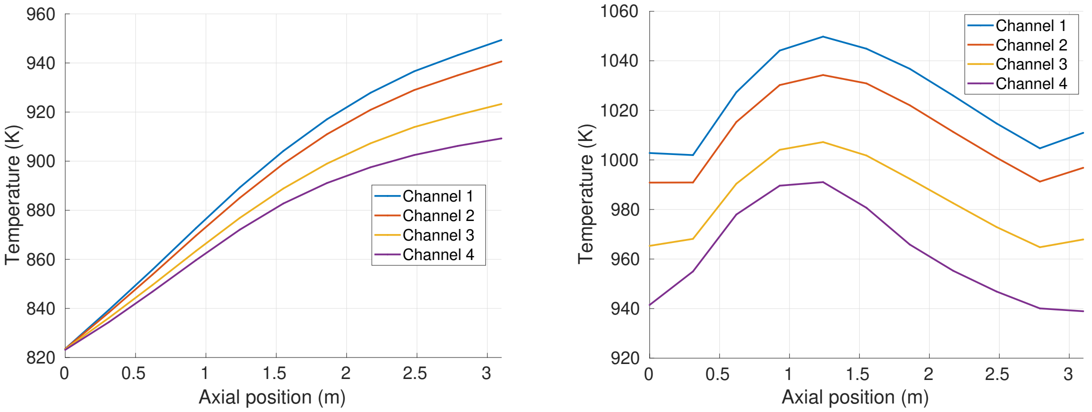

Figure 4.30: The axial T_c (left) and T_f (right) of gFHR SAM multi-channel model

The outlet and maximum fuel temperatures of each channel are listed in Table 4.9. Comparing to the results of the single-channel model, it can be observed that the maximum fuel temperature and the fuel outlet temperature predicted by the multi-channel model are about 40 K and 27 K higher, respectively, which is notable difference in the reactor safety analysis. Therefore, a multi-channel model is necessary for a better prediction of the maximum fuel temperature and the core outlet temperature.

Table 4.9: Channel temperatures calculated by the SAM multi-channel model

Channel number	1	2	3	4
T_{outlet} (K)	949.6	940.6	923.3	909.2
$T_{f,max}$ (K)	1049.8	1034.3	1007.2	989.6

Table 4.10 lists the computational resources used for the SAM single-channel model and multi-channel model in the steady-state simulation. The multi-channel model consumes more memory and converges slower than the single-channel model. However, the computation resource consumption is not proportional to the number of channels because of the overhead.

Table 4.10: Computational resource for the SAM single-channel model and multi-channel model

Model	Run time (s)	Memory (MB)
Single-channel	58	119
Multi-channel	139	200

4.5.3 SAM-Dakota Coupling Scheme for Uncertainty Analysis

The calculation scheme is depicted in Fig. 4.31, which is similar to the AGREE-Dakota coupling scheme introduced in Section 4.3.2. There are three modifications compared to the Dakota-AGREE coupling scheme:

1. The input values and uncertainties are for neutronics parameters, which are the power profile and reactivity coefficients data. The values are from AGREE and the uncertainties are from Dakota-AGREE coupling calculation.
2. The coupling with the DAKOTA code is with SAM instead of AGREE.
3. The input and output files for SAM are generated and processed by the input and output processors.

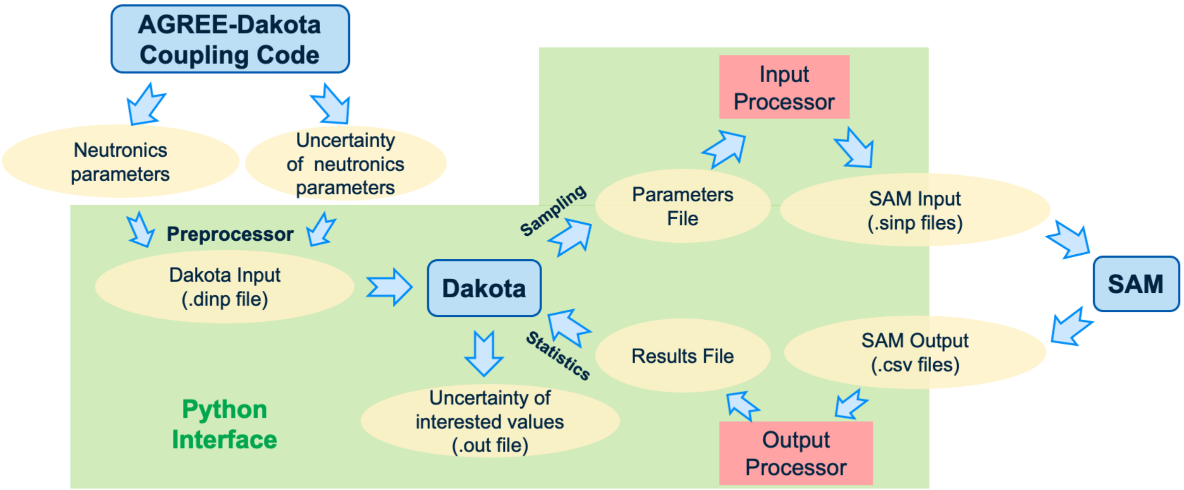

Fig. 4.31: Coupling scheme of SAM and Dakota for uncertainty calculation

4.5.4 Results of SAM-Dakota Calculation

The calculation scheme developed in Section 4.5.3 is applied on calculating the uncertainty of the SAM multi-channel temperatures. Since in the SAM steady-state calculation, only the local power data are obtained from Serpent/AGREE neutronics calculation. Therefore, the uncertainties of the local power are taken into account for calculating the uncertainties of SAM results. The local power data and their uncertainties are from Section 4.3.3 (shown in Fig. 4.20). The interested responses from SAM are the temperatures listed in Table 4.9. The uncertainty results are listed in Table 4.11 and Table 4.12.

Table 4.11: Uncertainty of channel outlet temperatures in the SAM multi-channel model

Parameter	$T_{out,1}$	$T_{out,2}$	$T_{out,3}$	$T_{out,4}$
Value (K)	949.6	940.6	923.3	909.2
Uncertainty (K)	0.0004	0.0002	0.0001	0.0001

Table 4.11 shows that the uncertainties of the coolant outlet temperature of the four channels due to the uncertainties of the local power calculated by AGREE are negligible. There are two reasons: one is that the uncertainties of local power data are very small (the RMS is only 0.44%, see Fig. 4.20), the other is that the power shape specified in SAM multi-channel model are normalized during the steady-state simulation. Since the coolant outlet temperature is only depend on the inlet coolant enthalpy and the core total power, the coolant outlet temperature is almost fixed after the power shape normalization, despite the perturbations on the local power data.

Table 4.12: Uncertainty of channel maximum fuel temperatures in the SAM multi-channel model

Parameter	$T_{f1,max}$	$T_{f2,max}$	$T_{f3,max}$	$T_{f4,max}$
Value (K)	1049.8	1034.3	1007.2	989.6
Uncertainty (K)	0.41	0.28	0.21	0.17

Table 4.12 shows that the uncertainties of the maximum fuel temperature of the four channels due to the uncertainties of the local power calculated by AGREE are very small, among which the largest uncertainty is only 0.41 K. Besides, the uncertainty value decreases from the center channel (Channel 1) to the outer channel (Channel 4). It is because that the uncertainties of local power at the centerline regions are larger than those at outer regions.

4.6 Summary

In this chapter, the stochastic method for Monte Carlo generated cross section uncertainty propagation based on AGREE-Dakota coupling is applied to the steady-state neutronics and thermo-fluids simulations of the gFHR reactor. The methods used in gFHR steady-state simulations, including the Serpent-AGREE code coupling, the branch cross section generation, the local power and region-wise reactivity coefficients calculation, the neutronics and thermo-fluids coupling in SAM code, are introduced first. The issues in the temperature dependent cross section interpolation are addressed by conducting a study of the interpolative error in Monte Carlo generated branch cross sections.

The stochastic method based on AGREE-Dakota coupling developed in Chapter 3 is further extended for the uncertainty quantification of the local power distribution and the region-wise reactivity coefficient distributions. The results show that the uncertainties of the local power distribution due to the uncertainty of Monte Carlo generated cross sections are in a small level, while the uncertainties of the region-wise reactivity coefficients are larger.

A stochastic method based on SAM-Dakota coupling is developed to propagate the uncertainty of Serpent/AGREE calculated neutronics parameters to SAM simulations. The method is then applied to the SAM simulation of the gFHR steady-state case. The results show that the uncertainties of the maximum coolant and fuel temperatures in the SAM multi-channel steady-state simulation propagated from the uncertainty of Serpent/AGREE calculated neutronics parameters are all at a very low level.

CHAPTER 5

Uncertainty Analysis of the gFHR: Transient Simulations

5.1 Methods of gFHR Transient Analysis

The capability of both steady-state and transient analysis are essential for licensing new reactor designs. Transient analysis enhances the understanding of the fundamental physics of the reactors and provides guidance for both the operational and safety analysis of the reactor. Both the AGREE and SAM codes have the capability of performing transient simulations, however the AGREE code is primarily focused on the neutronics and thermo-fluids coupling simulation of the reactor core, whereas the SAM code is a reactor system code which can model the primary loop, secondary loop and all the key reactor system components. In this section, the methods used for the gFHR transient analysis in the AGREE code and in the SAM code will be briefly introduced.

5.1.1 gFHR Transient Simulation in AGREE

For simulation of the transient cases using the AGREE code, the control rods in the gFHR are of primary importance. The gFHR control rod system design was released by Kairos Power [51], and is included in the Kairos Power's gFHR benchmark model (Section 2.4). There are 10 control rods inserted in the side reflector region surrounding the active core, as illustrated in Fig. 5.1.

The control rods are used for reactivity management during normal operation and transient conditions. The total worth of the 10 rods must also be capable of shutting down the reactor at any time. The fully inserted position of the rod is aligned with the bottom of the pebble bed active core, and the fully withdrawn position is aligned with the top of the top reflector. The detailed design parameters of the control rods are listed in Table 5.1.

The gFHR core with the control rod system was modeled in Serpent by homogenizing each control rod into the cross sections of the adjacent side reflector region. A control rod branch was then used in GenPMAXS to generate control rod dependent cross sections for the AGREE code.

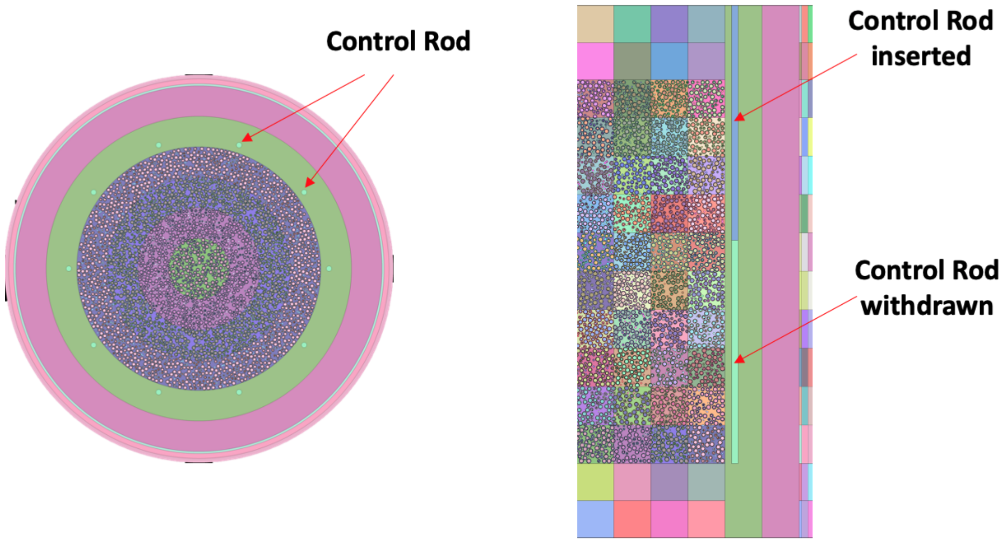

Fig. 5.1: Control rod system design in the gFHR core, axial (left) and radial (right) cross section views

Table 5.1: Design parameters of the gFHR control rod system

Parameter	Value
Absorber Material	B_4C
Boron Enrichment	100% ^{10}B
Absorber Density	$1.76\ \mathrm{g/cm^3}$
Number of Rods	10
Diameter of Rods	$5.2\ \mathrm{cm}$
Centroid of Rods	$7.9\ \mathrm{cm}$ from the core-reflector interface
Azimuthal Distribution	Equidistantly distributed
Un-roded Material	Flibe
Cladding	None cladded

In AGREE, the region absorption cross section was determined based on the control rod insertion depth.

For the transient analysis in AGREE, two ways were considered for modeling the rate of reactivity insertion and removal because of control rod movement. One is through a user-defined time-dependent external reactivity insertion function, and the other is through a user-defined time-dependent control rod movement function.

The reactivity feedback during the transient was calculated based on the neutronics/thermo-fluids coupling and temperature-dependent cross sections. During a transient simulation, the total power at a certain transient time step can be calculated either by the point kinetics or spatial kinetics solver in AGREE. The temperature distributions of the core materials are then calculated by the thermo-fluids solver. The cross sections are then updated based on the new temperature distributions and the feedback reactivities are then calculated.

5.1.2 gFHR Transient Simulation in SAM

In the SAM code a Point Kinetics Equation (PKE) solver was implemented for the simulation of transient cases [7]. In the point kinetics equation solver, the feedback from fuel axial expansion, core radial expansion, fuel Doppler, coolant density, moderator temperature and xenon concentration are modeled. In the transient analysis of the gFHR core, the fuel axial expansion and core radial expansion reactivity feedback are not considered because the data was not included in the benchmark. Only the reactivity feedback from fuel Doppler, coolant density and moderator temperature are considered based on the results calculated in Section 4.1.6. The xenon feedback reactivity is modeled with a lumped iodine/xenon decay solver.

The PKE model in SAM relies on the kinetics parameters calculated from Serpent code and AGREE codes. Table 5.2 lists the source of kinetics parameters used in SAM.

Table 5.2: Kinetics parameters calculated by Serpent and AGREE that are used as input in SAM

Code	Parameters
Serpent	Xe-135/I-135 constants, total flux, lumped fission XS, rod worth
AGREE	Power shape, region-wise reactivity coefficients

5.1.3 gFHR Reactivity Coefficients Conversion in SAM

There are several types of reactivity feedback models implemented in SAM code, including the linear temperature feedback model, linear density feedback model, logarithmic temperature feedback model, linear expansion feedback model and lumped xenon feedback model[52]. In the gFHR SAM model, the linear temperature feedback model is chosen for moderator and reflector reactivity feedback, while the linear density feedback model is used for coolant reactivity feedback. For fuel temperature feedback, both the logarithmic temperature feedback model and the linear temperature feedback model are tested, the results show that the linear feedback model achieves better agreement with AGREE result. Therefore, the linear temperature feedback model is chosen for fuel reactivity feedback.

For the linear temperature reactivity feedback model, the feedback reactivity is calculated by

$$\rho_x(t) = \sum_{i=1}^{N} \alpha_{T_x,i} \left(\overline{T}_{x,i}(t) - \overline{T}_{x,i}^{ss} \right) \quad , \tag{5.1}$$

where i denotes the region ID; x denotes the material type including fuel, moderator and reflector; $\overline{T}_{x,i}^{ss}$ is the steady-state average material temperature at region i. For the fuel and moderator, the reactivity coefficients $\alpha_{T_x,i}$ are the region-wise ones calculated in Chapter 4 Section 4.1.6.3. For the reflectors, since they are modelled in five parts separately (see Fig. 4.27), the region-wise reflector temperature reactivity coefficients shown in Fig. 4.10 are summed into five lumped values. Note that the values in Fig. 4.9 and Fig. 4.10 are calculated by Eq. (4.3) in unit of $\mathrm{pcm/K}$. There is an approximation by neglecting the $1/k_{\text{eff}}^2$ term in Eq. (4.3). This approximation is eliminated by multiplying $1/k_{\text{eff}}^2$ to the values when they are converted to $\Delta k/k$ per K in SAM model.

For the linear density reactivity feedback model, the feedback reactivity is calculated by

$$\rho_x(t) = \sum_{i=1}^{N} \alpha_{d_x,i} \left(d_{x,i}(t) - d_{x,i}^{ss} \right) V_{x,i} \quad , \tag{5.2}$$

where i denotes the region ID; x denotes the material type, which is coolant; $d_{x,i}^{ss}$ is the steady-state coolant density and $V_{x,i}$ is the volume of coolant in region i. The coolant density $d_{x,i}(t)$ in the transient is calculated based on the coolant temperature. $\alpha_{d_x,i}$ is the density reactivity coefficient in unit of $\Delta k/k$ per kg. Since in Fig. 4.9, the coolant reactivity coefficients $\alpha_{T_c,i}$ are based on coolant temperature, they need to be converted to $\alpha_{d_c,i}$. In gFHR, the coolant is flibe and the density of flibe follows a linear relation to the flibe temperature[53]:

$$d = 2415.6 - 0.49072T \quad , \tag{5.3}$$

where the flibe density d is in unit of $\mathrm{kg/m^3}$ and the flibe temperature T is in unit of K. Then the region-wise coolant temperature reactivity coefficients in Fig. 4.9 can be converted to coolant density reactivity coefficients. The results are shown in Fig. 5.2.

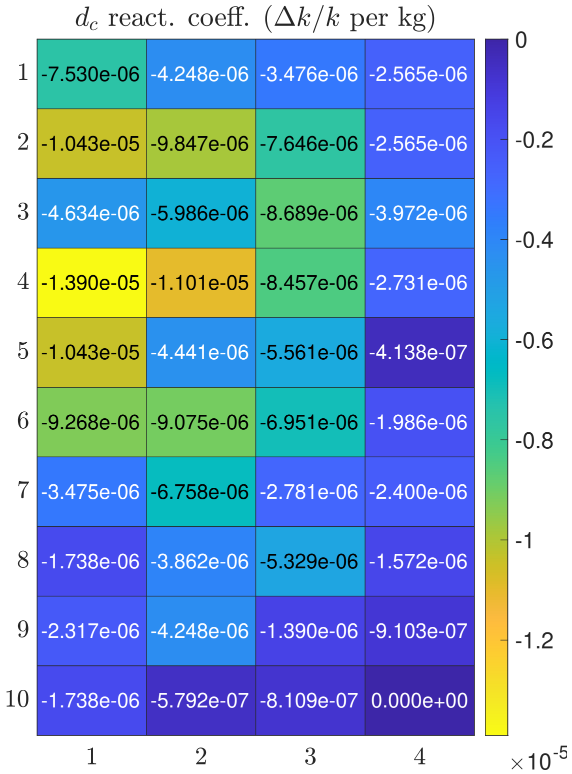

d_c react. coeff. ($\Delta k/k$ per kg)

	1	2	3	4
1	-7.530e-06	-4.248e-06	-3.476e-06	-2.565e-06
2	-1.043e-05	-9.847e-06	-7.646e-06	-2.565e-06
3	-4.634e-06	-5.986e-06	-8.689e-06	-3.972e-06
4	-1.390e-05	-1.101e-05	-8.457e-06	-2.731e-06
5	-1.043e-05	-4.441e-06	-5.561e-06	-4.138e-07
6	-9.268e-06	-9.075e-06	-6.951e-06	-1.986e-06
7	-3.475e-06	-6.758e-06	-2.781e-06	-2.400e-06
8	-1.738e-06	-3.862e-06	-5.329e-06	-1.572e-06
9	-2.317e-06	-4.248e-06	-1.390e-06	-9.103e-07
10	-1.738e-06	-5.792e-07	-8.109e-07	0.000e+00

Fig. 5.2: Coolant density reactivity coefficients in gFHR, converted from coolant temperature reactivity coefficients in Fig. 4.9

5.1.4 Model of the Control Rod Dependent Power Shape Function

One innovative feature developed in the research here and implemented in the SAM code is a point kinetics option which estimates the impact of the control rod movement on the reactivity in SAM based on pre-computed AGREE power distribution data. For most cases, the point kinetics solver is sufficiently accurate. However, for cases in which there a significant change in the power shape during the transient, the point kinetics solver can have substantial errors because it does not take into account changes in the spatial shape of the flux. For the transient cases studied in this section, the control rod position changes during the transient are modelled in SAM, which is one of the most important mechanisms for changes in the power distribution.

The control rod dependent power shape function was implemented in SAM by enabling the user to input a multi-linear interpolation function as a power shape function $p(z, pos_{cr})$ that is both axial (z) dependent and control rod position (pos_{cr}) dependent for a each core channel.

Fig. 5.3 is an illustration of a control rod position dependent axial power shape function of the gFHR core. In SAM code, once the control rod position pos_{cr} is determined in a certain time step, the axial power shape $p(z)$ at position pos_{cr} is interpolated and applied to the core channel as the heat source of the channel.

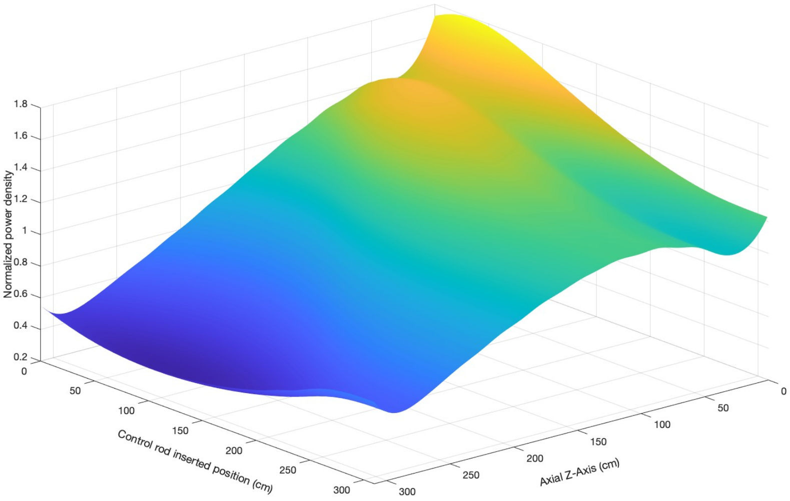

Fig. 5.3: The 3-D surface plot of the control rod position dependent axial power shape function of the gFHR core

The following case provides an example to demonstrate how the control rod dependent power shape function can improve the prediction of the power in a transient case. Assuming that the initial control rod position is $z_1 = 1.6\mathrm{m}$, during $0 < t < 1\mathrm{s}$, the control rod moves from the initial position z_1 to position $z_2 = 2.6\mathrm{m}$ in constant speed. In other words, the control rod is withdrawn from the core by $1.0\mathrm{m}$ in 1 second, which introduces a reactivity of around $1.15\$$. After $t > 1\mathrm{s}$, the control rod stays at $z_2 = 1.6\mathrm{m}$.

This transient case can be simulated in SAM in two ways:

(a) Assuming the core axial power shape is fixed during the whole transient. The fixed axial power shape is the power shape at $z_1 = 1.6\mathrm{m}$.

(b) Assuming the core axial power shape changes when the control rod moves. The axial power shape for control rod at $z_1 = 1.6\mathrm{m}$ and at $z_2 = 2.6\mathrm{m}$ are shown in Fig. 5.4.

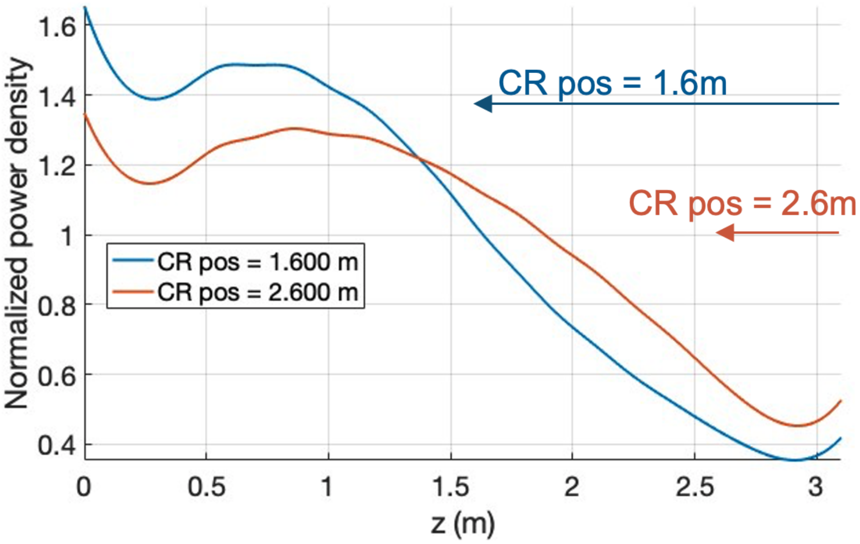

Fig. 5.4: The axial power shape when the control rod position is at $z_1 = 1.6\mathrm{m}$ and at $z_2 = 2.6\mathrm{m}$

The power history predicted by SAM for Case (a) and Case (b) are shown in Fig. 5.5. For the tail power of the transient case at $t = 10\mathrm{s}$, there is a 4.5% difference, which shows that the control rod position dependent power shape function does help the point kinetics solver improve the results in a transient simulation by taking the spatial effect into account.

5.2 Introduction of the gFHR Transient Case

In the gFHR benchmark developed and released by Kairos Power, the focus was primarily on the reactor core design and steady-state k_{eff} calculations. A transient reactivity case was developed in in the work here to demonstrate the results of this research.

A ramp reactivity transient case is created by inserting and removing a reactivity linearly. The transient is initialized by inserting a reactivity linearly of 0.5$ in 1.0 second. Then the reactivity is then removed also linearly in the next 5 seconds. This is depicted in Fig. 5.6.

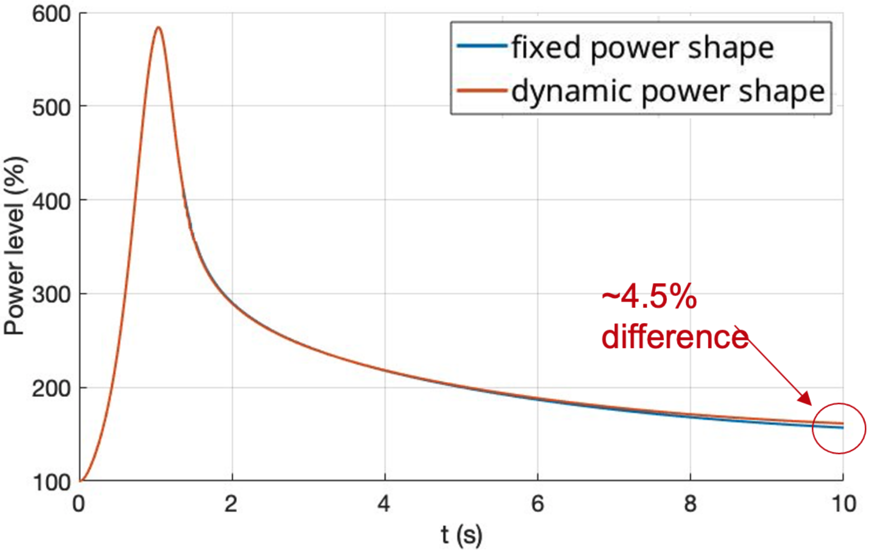

Fig. 5.5: The power history predicted by SAM for Case (a) fixed power shape, and Case (b) dynamic power shape

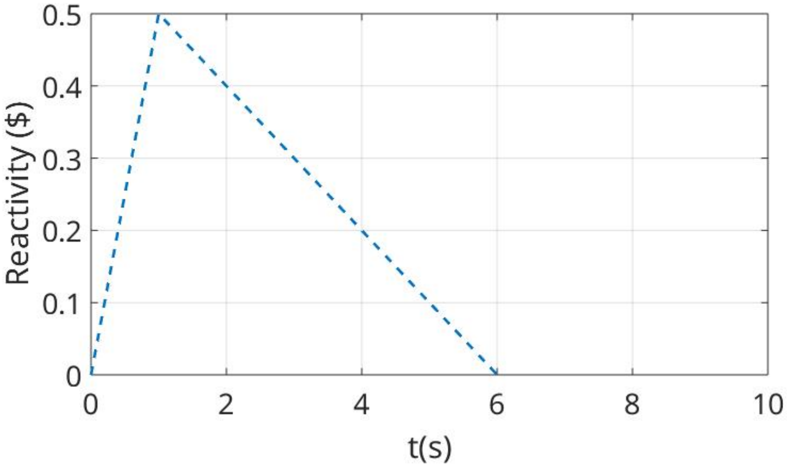

Fig. 5.6: The insertion and removal of external reactivity in the ramp reactivity transient case

The ramp reactivity case was simulated in both the AGREE code and SAM code. For the AGREE code, the case was simulated in three conditions:

(a) All the feedback are NOT considered.

(b) The feedback from fuel Doppler, coolant temperature and moderator temperature are considered. The fuel kernel temperature is calculated for Doppler feedback.

(c) The feedback from fuel Doppler, coolant temperature and moderator temperature are considered. The fuel kernel temperature is not calculated.

For the SAM code, the case was simulated for two conditions:

(a) All the feedback are NOT considered.

(b) The feedback from fuel Doppler, coolant temperature and moderator temperature are considered. The fuel kernel temperature is not calculated.

The power history results of the ramp reactivity transient case predicted by AGREE and Serpent are shown in Fig. 5.7. It shows that the results from AGREE and SAM agree well with each other for both the non-feedback case and the fuel Doppler without kernel temperature case.

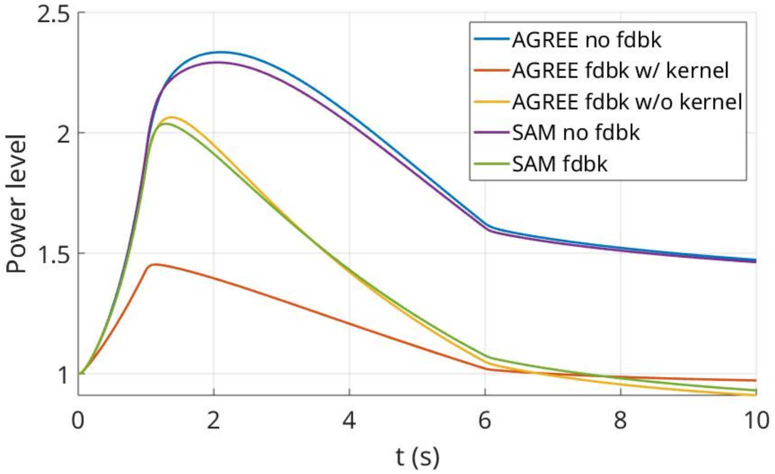

Fig. 5.7: The power history predicted by AGREE and SAM in different conditions during the ramp reactivity transient

The fuel temperature and the feedback reactivity from fuel Doppler calculated by AGREE and SAM are shown in Fig. 5.8 and Fig. 5.9, respectively. Fig. 5.8 and Fig. 5.9 explain the how the feedback reactivity in different simulation conditions affects the power history prediction shown in Fig. 5.7. When the fuel Doppler feedback is considered, the fuel temperature increases as the power increases, which brings negative feedback reactivity to the core. Thus the maximum power and the tail power during the transient are smaller. Since the fuel kernel temperature is higher than the average fuel temperature, if the fuel kernel temperature is calculated for the Doppler feedback, the negative feedback reactivity will be even larger and thus the peak power will be lower.

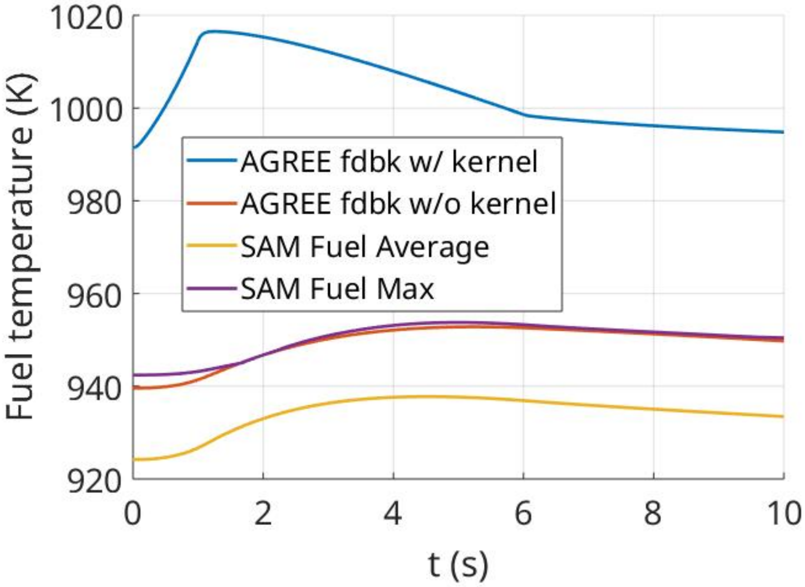

Fig. 5.8: The fuel temperature calculated by AGREE and SAM in different conditions during the ramp reactivity transient

5.3 Uncertainty of Neutronics Parameters in SAM Transient Simulations

5.3.1 Uncertainty Analysis of Control Rod Worth

The integral control rod worth is calculated by

$$\rho_{cr_i} = \rho_{cr_0} - \rho_{cr_i} = \frac{1}{k_i} - \frac{1}{k_0} \quad . \tag{5.4}$$

According to the rule of uncertainty propagation (referring to Appendix A),

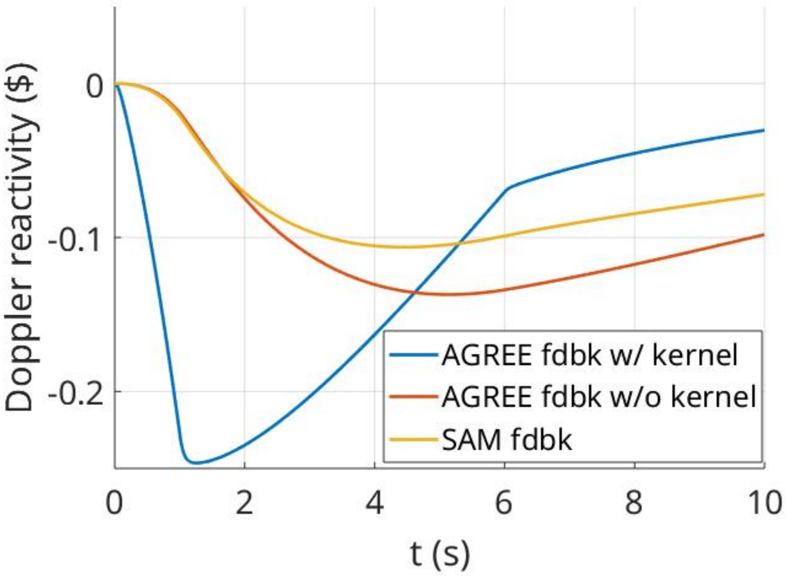

Fig. 5.9: The fuel Doppler feedback reactivity calculated by AGREE and SAM in different conditions during the ramp reactivity transient

$$\begin{aligned}\frac{\mathrm{d}\rho_{cr_i}}{\rho_{cr_i}} &= \mathrm{d}(\ln\rho_{cr_i}) \\ &= \frac{\partial(\ln\rho_{cr_i})}{\partial k_0}\mathrm{d}k_0 + \frac{\partial(\ln\rho_{cr_i})}{\partial k_i}\mathrm{d}k_i \quad ,\end{aligned} \tag{5.5}$$

the relative uncertainty of integral control rod worth ρ_{cr_i} can be evaluated by

$$\begin{aligned}\frac{\Delta_{\rho_{cr_i}}}{\rho_{cr_i}} &= \sqrt{\left(\frac{\partial(\ln\rho_{cr_i})}{\partial k_0}\Delta_{k_0}\right)^2 + \left(\frac{\partial(\ln\rho_{cr_i})}{\partial k_i}\Delta_{k_i}\right)^2} \\ &= \sqrt{\left[\left(\frac{1}{k_0 - k_i} - \frac{1}{k_0}\right)\Delta_{k_0}\right]^2 + \left[\left(\frac{1}{k_i - k_0} - \frac{1}{k_i}\right)\Delta_{k_i}\right]^2}\end{aligned} \tag{5.6}$$

where k_0 and k_1 are the nominal values, Δ_{k_0} and Δ_{k_1} are the uncertainties of k_0 and k_1.

If the control rod worth is reported in the unit of \$, i.e.,

$$\rho_{cr_i} = \frac{\rho_{cr_0} - \rho_{cr_i}}{\beta_{\text{eff}}} = \left(\frac{1}{k_i} - \frac{1}{k_0}\right)\frac{1}{\beta_{\text{eff}}} \quad , \tag{5.7}$$

the uncertainty of β_{eff} should also be considered. Then the propagation of the uncertainty of ρ_{cr_i}

becomes

$$\begin{aligned}\frac{\mathrm{d}\rho_{cr_i}}{\rho_{cr_i}} &= \mathrm{d}(\ln\rho_{cr_i}) \\ &= \frac{\partial(\ln\rho_{cr_i})}{\partial k_0}\mathrm{d}k_0 + \frac{\partial(\ln\rho_{cr_i})}{\partial k_i}\mathrm{d}k_i + \frac{\partial(\ln\rho_{cr_i})}{\partial \beta_{\text{eff}}}\mathrm{d}\beta_{\text{eff}} \quad . \end{aligned} \tag{5.8}$$

Thus, the relative uncertainty of integral control rod worth ρ_{cr_i} in unit of \$ can be evaluated by

$$\begin{aligned}\frac{\Delta_{\rho_{cr_i}}}{\rho_{cr_i}} &= \sqrt{\left(\frac{\partial(\ln\rho_{cr_i})}{\partial k_0}\Delta_{k_0}\right)^2 + \left(\frac{\partial(\ln\rho_{cr_i})}{\partial k_i}\Delta_{k_i}\right)^2 + \left(\frac{\partial(\ln\rho_{cr_i})}{\partial \beta_{\text{eff}}}\Delta_{\beta_{\text{eff}}}\right)^2} \\ &= \sqrt{\left[\left(\frac{1}{k_0-k_i}-\frac{1}{k_0}\right)\Delta_{k_0}\right]^2 + \left[\left(\frac{1}{k_i-k_0}-\frac{1}{k_i}\right)\Delta_{k_i}\right]^2 + \left(\frac{\Delta_{\beta_{\text{eff}}}}{\beta_{\text{eff}}}\right)^2}\end{aligned} \tag{5.9}$$

5.3.2 Uncertainty of Power Shape Function

The control rod dependent power shape function shown in Fig. 5.3 are obtained by moving the control rods in AGREE steady-state calculations. The control rods are moved by 15.5 cm in the active core region and 15.0 cm in the top reflector region for each case. Therefore, the control rods are moved by 24 times and 24 axial power shape functions are obtained to compose the control rod dependent power shape function in Fig. 5.3. It would be computationally expansive to quantify the uncertainty of local power for all the 24 cases. Therefore, only the local power uncertainty of the case that the control rods are at $z = 139.5\ \mathrm{cm}$ (near criticality control rod position) is quantified and the relative uncertainty for other cases are assumed to be the same as this case. The uncertainties of each axial nodes of the power shape function are shown in Fig. 5.10.

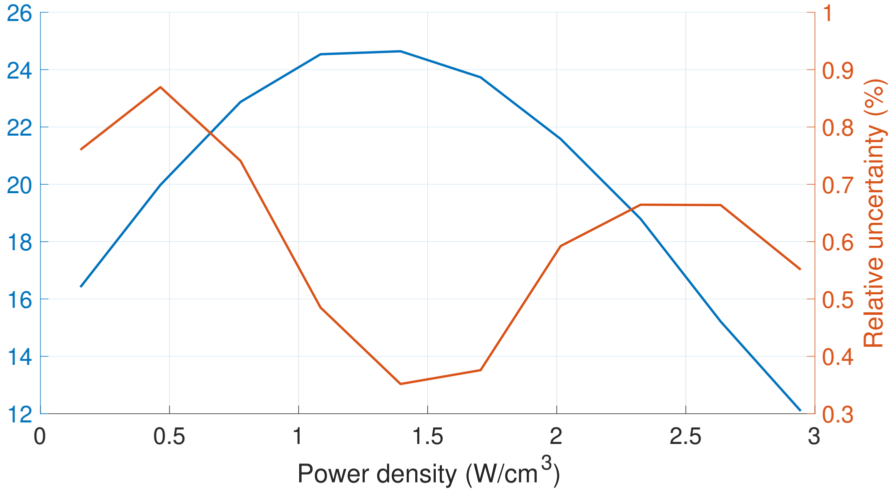

Fig. 5.10: Relative uncertainty of the axial power shape function

Fig. 5.10 shows that the relative uncertainties of the power shape function at all axial nodes are less than 1%. Besides, the uncertainties are smaller at the higher power density regions.

5.4 SAM-Dakota Coupling for UQ in Transient Simulations

The SAM-Dakota coupling scheme of the uncertainty quantification for SAM transient simulations is similar to what is illustrated in Fig. 4.31.

5.4.1 Results of the Ramp Reactivity Transient Case

For the ramp reactivity transient case, the neutronics parameters including the local power and region-wise reactivity coefficients from AGREE are used in SAM point kinetics model. Therefore, the uncertainties of the local power and region-wise reactivity coefficients are taken into account for the uncertainty quantification of the SAM transient simulation. The interested responses include the maximum coolant temperatures, the maximum fuel temperatures in the channels, the maximum core power and the asymptotic tail power.

The results of maximum channel coolant temperatures are shown in Table 5.3. Two estimations of the uncertainties are reported, one is calculated by assuming the neutronics parameters are independent, the other is calculated by assuming the neutronics parameters are correlated and the correlation matrix is obtained in Section 4.4.3. It shows that correlated estimations are smaller than the independent estimations, which means that the dominate correlation coefficients between the neutronics parameters are negative. Nevertheless, the independent assumption can provide a more conservative estimations for the uncertainties of maximum temperatures.

Table 5.3 shows that the uncertainties for the four channels are all smaller than $0.25\ \mathrm{K}$, which are almost negligible in the transient analysis. The contributions to the uncertainty from the uncertainty of local power and region-wise reactivity coefficients are shown in Table 5.4. It shows that the major contribution to the uncertainty of maximum channel coolant temperatures is from the uncertainty of local power, which is over 50%. The contribution from the uncertainty of fuel temperature reactivity coefficients is also significant, which is around 20% to 40%. The contribution from the uncertainty of reflector temperature reactivity coefficients is negligible. To be noted, the results in Table 5.4 show that, even the uncertainties of α_{T_m} and α_{T_c} are higher than the uncertainties of α_{T_f}, the contribution from $\Delta\alpha_{T_f}$ is still higher than the contributions from $\Delta\alpha_{T_m}$ and $\Delta\alpha_{T_c}$. There are two reasons: (1) the uncertainties are reported in relative percentages, even the relative uncertainties of α_{T_m} and α_{T_c} are higher, the absolute values may still be smaller than the uncertainties of α_{T_f}; (2) the temperature change in fuel are more dramatically than that in moderator and coolant, therefore, the reactivity feedback from fuel are stronger than that from moderator and coolant.

Tab. 5.3: Channel maximum coolant temperatures in the SAM simulation of the ramp reactivity transient case and their uncertainties

Parameter		$T_{c1,max}$	$T_{c2,max}$	$T_{c3,max}$	$T_{c4,max}$
Value (K)		966.0	956.0	936.3	919.9
Uncertainty (K)	independent	0.25	0.20	0.14	0.12
	correlated	0.13	0.12	0.10	0.08

Tab. 5.4: Percentage contributions to the channel maximum coolant temperature uncertainties from the uncertainties of local power and region-wise reactivity coefficients, unit: %

Contribution to	$\Delta T_{c1,max}$	$\Delta T_{c2,max}$	$\Delta T_{c3,max}$	$\Delta T_{c4,max}$
ΔP_i	73.3	65.4	51.6	55.4
$\Delta\alpha_{T_f,i}$	20.4	26.5	37.0	34.0
$\Delta\alpha_{T_m,i}$	4.8	6.2	8.8	8.2
$\Delta\alpha_{T_c,i}$	1.4	1.8	2.4	2.1
$\Delta\alpha_{T_r,i}$	0.0	0.0	0.0	0.0

The results of channel maximum fuel temperatures are shown in Table 5.5. It shows that the uncertainties for the four channels are all smaller than 0.44 K, which are almost negligible in the transient analysis. The contributions to the uncertainty from the uncertainty of local power and region-wise reactivity coefficients are shown in Table 5.6. Unlike the channel coolant temperature case, it shows that the major contribution to the uncertainty of channel maximum fuel temperatures is from the uncertainty of region-wise fuel temperature reactivity coefficients, which can be as high as over 70%. The contribution from the uncertainty of local power ranges from 7.7% to 25.3%, which is also not negligible.

Tab. 5.5: Maximum channel fuel temperatures in the SAM simulation of the ramp reactivity transient case and their uncertainties

Parameter		$T_{f1,max}$	$T_{f2,max}$	$T_{f3,max}$	$T_{f4,max}$
Value (K)		1070.8	1053.8	1024.3	1006.5
Uncertainty (K)	independent	0.44	0.39	0.33	0.34
	correlated	0.40	0.37	0.32	0.30

The results of the maximum core power and asymptotic core power are shown in Table 5.7. It shows that the uncertainties are both less than 0.2 %. The contributions to the uncertainty from

Tab. 5.6: Percentage contributions to the channel maximum fuel temperature uncertainties from the uncertainties of local power and region-wise reactivity coefficients, unit: %

Contribution to	$\Delta T_{f1,max}$	$\Delta T_{f2,max}$	$\Delta T_{f3,max}$	$\Delta T_{f4,max}$
ΔP_i	19.0	13.7	7.7	25.3
$\Delta \alpha_{T_f,i}$	63.5	67.6	72.4	58.6
$\Delta \alpha_{T_m,i}$	9.6	10.2	10.9	8.8
$\Delta \alpha_{T_c,i}$	7.7	8.2	8.8	7.1
$\Delta \alpha_{T_r,i}$	0.0	0.0	0.0	0.0

the uncertainty of local power and region-wise reactivity coefficients are shown in Table 5.8. It shows that contribution is mainly from the uncertainty of region-wise fuel temperature reactivity coefficients, which is more than 65%. For the maximum core power, the contribution from the uncertainty of moderator temperature reactivity coefficients is the second important; while for the asymptotic tail core power, the contribution from the uncertainty of coolant temperature reactivity coefficients is the second important.

Tab. 5.7: Maximum and asymptotic core power in the SAM simulation of the ramp reactivity transient case and their uncertainties

Parameter		P_{max}	P_{asy}
Value (% full-power)		207.2	87.3
Uncertainty (% full-power)	independent	0.17	0.19
	correlated	0.18	0.19

Tab. 5.8: Percentage contributions to the uncertainties of maximum core power and asymptotic core power from the uncertainties of local power and region-wise reactivity coefficients, unit: %

Contribution to	ΔP_{max}	ΔP_{asy}
ΔP_i	0.4	0.0
$\Delta \alpha_{T_f,i}$	65.3	72.6
$\Delta \alpha_{T_m,i}$	34.0	3.2
$\Delta \alpha_{T_c,i}$	0.2	24.0
$\Delta \alpha_{T_r,i}$	0.0	0.0

5.4.2 Results of the Ramp Reactivity Transient Case with Reduced Neutron Histories

In Section 3.3.4.2, the relation between the uncertainty and the number of neutron histories used in Monte Carlo cross section generation has been studied for the AGREE steady-state k_{eff} . In this section, a similar study is performed to investigate the relation between the uncertainty and the number of histories for the SAM transient output parameters.

In Section 5.4.1, the preceding Monte Carlo cross section generation simulates 500,000 neutrons for 100 inactive cycles and 500 active cycles. In this section, the number of neutrons is reduced by a factor of 10.

The relative uncertainty of the local power and the region-wise reactivities are shown in Fig. 5.11 to Fig. 5.13. Comparing the results to the uncertainty results calculated in Fig. 4.20, Fig. 4.22, Fig. 4.23, Fig. 4.24, Fig. 4.25, it can be observed that when the number of neutron histories is reduced by 10 times, the relative uncertainties are increased by around 3 times. In other words, the uncertainties of local power and region-wise reactivity coefficients are inversely proportional to the square root of the number of neutron histories, which is consistent with the expectation.

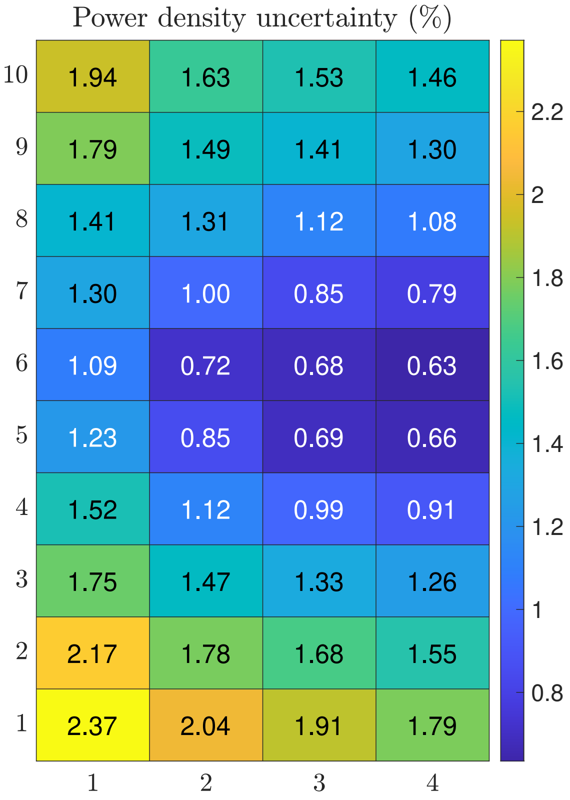

	1	2	3	4
10	1.94	1.63	1.53	1.46
9	1.79	1.49	1.41	1.30
8	1.41	1.31	1.12	1.08
7	1.30	1.00	0.85	0.79
6	1.09	0.72	0.68	0.63
5	1.23	0.85	0.69	0.66
4	1.52	1.12	0.99	0.91
3	1.75	1.47	1.33	1.26
2	2.17	1.78	1.68	1.55
1	2.37	2.04	1.91	1.79

Fig. 5.11: Relative uncertainty of local power density for reduced number of neutron histories

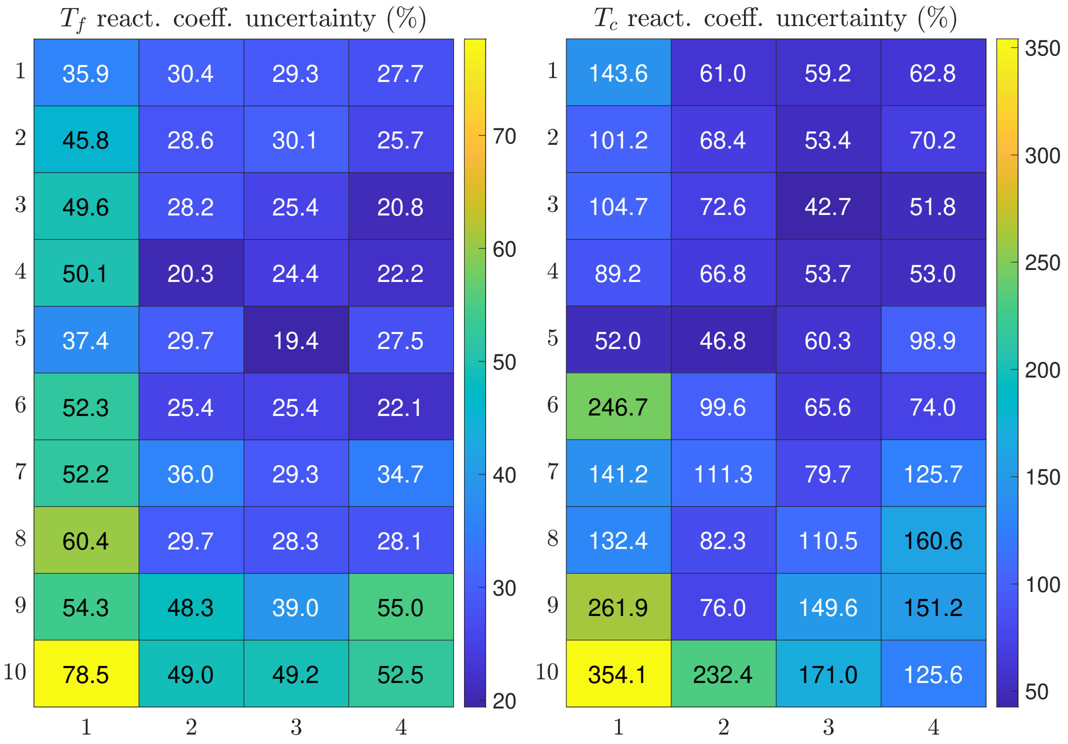

T_f react. coeff. uncertainty (%)

	1	2	3	4
1	35.9	30.4	29.3	27.7
2	45.8	28.6	30.1	25.7
3	49.6	28.2	25.4	20.8
4	50.1	20.3	24.4	22.2
5	37.4	29.7	19.4	27.5
6	52.3	25.4	25.4	22.1
7	52.2	36.0	29.3	34.7
8	60.4	29.7	28.3	28.1
9	54.3	48.3	39.0	55.0
10	78.5	49.0	49.2	52.5

T_c react. coeff. uncertainty (%)

	1	2	3	4
1	143.6	61.0	59.2	62.8
2	101.2	68.4	53.4	70.2
3	104.7	72.6	42.7	51.8
4	89.2	66.8	53.7	53.0
5	52.0	46.8	60.3	98.9
6	246.7	99.6	65.6	74.0
7	141.2	111.3	79.7	125.7
8	132.4	82.3	110.5	160.6
9	261.9	76.0	149.6	151.2
10	354.1	232.4	171.0	125.6

Figure 5.12: Relative uncertainty of region-wise α_{T_f} (left) and α_{T_c} (right) for reduced number of neutron histories

The uncertainties of local power and region-wise reactivity coefficients are then propagated to the SAM transient simulation of the ramp reactivity case. The results for the maximum coolant temperatures, maximum fuel temperatures and the core powers are shown in Table 5.9, Table 5.10 and Table 5.11, respectively. Comparing to the uncertainties listed in Table 5.3, Table 5.5 and Table 5.7, when the number of neutron histories in preceding Monte Carlo simulation is reduced by 10 times, the uncertainties of the SAM transient results are increased by about 3 times. It still satisfies the rule that the uncertainty is inversely proportional to the square root of the number of neutron histories.

Tab. 5.9: Channel maximum coolant temperatures in the SAM simulation of the ramp reactivity transient case and their uncertainties

Parameter	$T_{c1,max}$	$T_{c2,max}$	$T_{c3,max}$	$T_{c4,max}$
Value (K)	966.0	956.0	936.3	919.9
Uncertainty (K)	0.89	0.74	0.57	0.48

In this chapter, the impact of the uncertainty in the reactivity coefficient parameters calculated by Serpent/AGREE were propagated into the transient analysis of the SAM code using the Dakota

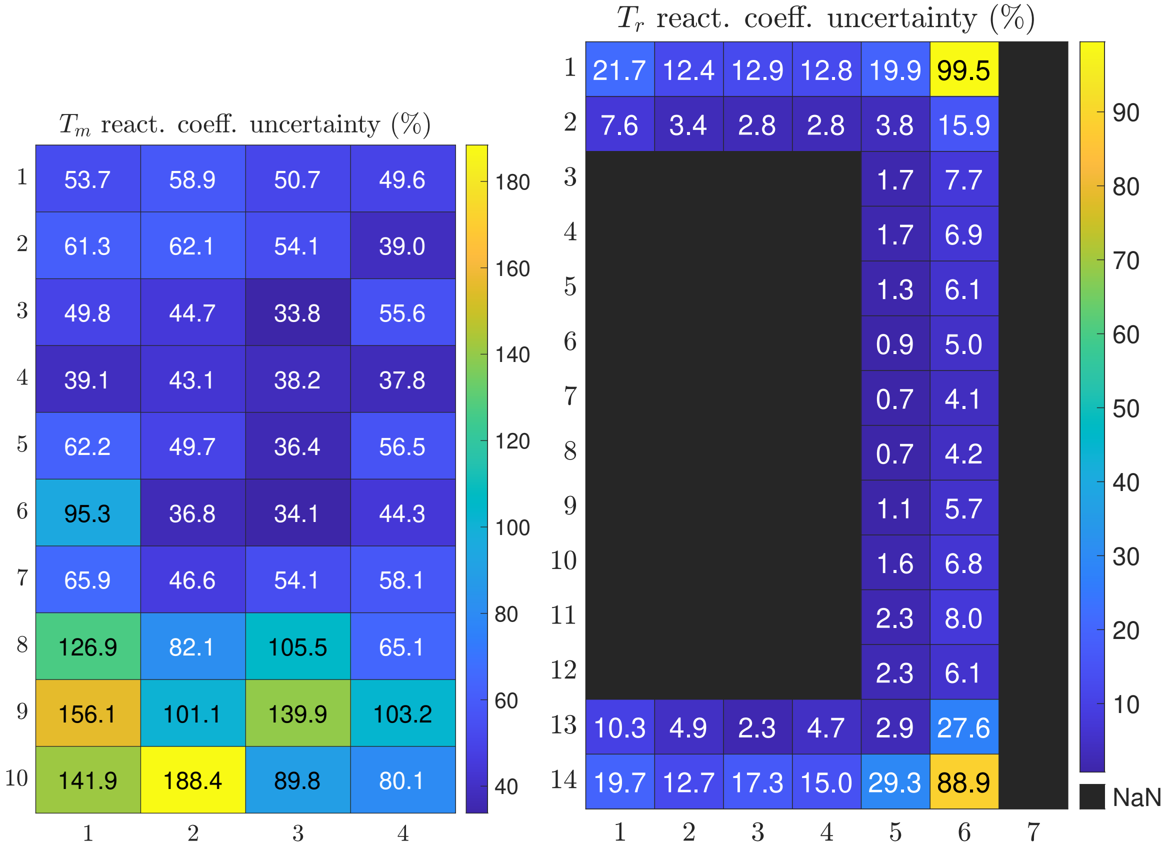

	1	2	3	4
1	53.7	58.9	50.7	49.6
2	61.3	62.1	54.1	39.0
3	49.8	44.7	33.8	55.6
4	39.1	43.1	38.2	37.8
5	62.2	49.7	36.4	56.5
6	95.3	36.8	34.1	44.3
7	65.9	46.6	54.1	58.1
8	126.9	82.1	105.5	65.1
9	156.1	101.1	139.9	103.2
10	141.9	188.4	89.8	80.1

	1	2	3	4	5	6	7
1	21.7	12.4	12.9	12.8	19.9	99.5	■
2	7.6	3.4	2.8	2.8	3.8	15.9	■
3	■	■	■	■	1.7	7.7	■
4	■	■	■	■	1.7	6.9	■
5	■	■	■	■	1.3	6.1	■
6	■	■	■	■	0.9	5.0	■
7	■	■	■	■	0.7	4.1	■
8	■	■	■	■	0.7	4.2	■
9	■	■	■	■	1.1	5.7	■
10	■	■	■	■	1.6	6.8	■
11	■	■	■	■	2.3	8.0	■
12	■	■	■	■	2.3	6.1	■
13	10.3	4.9	2.3	4.7	2.9	27.6	■
14	19.7	12.7	17.3	15.0	29.3	88.9	■

Figure 5.13: Relative uncertainty of region-wise α_{T_m} (left) and α_{T_r} (right) for reduced number of neutron histories

Tab. 5.10: Maximum channel fuel temperatures in the SAM simulation of the ramp reactivity transient case and their uncertainties

Parameter	$T_{f1,max}$	$T_{f2,max}$	$T_{f3,max}$	$T_{f4,max}$
Value (K)	1070.8	1053.8	1024.3	1006.5
Uncertainty (K)	1.42	1.28	1.09	1.10

Tab. 5.11: Maximum and asymptotic core power in the SAM simulation of the ramp reactivity transient case and their uncertainties

Parameter	P_{max}	P_{asy}
Value (% full-power)	207.2	87.3
Uncertainty (% full-power)	0.63	0.57

code and methods developed and demonstrated in in Chapter 4 The method was extended for the SAM transient simulations by first developing models in SAM for the gFHR transient simulation, to include the point kinetics solver, the reactivity feedback model, the control rod model, and the control rod dependent cross sections. Then a transient ramp reactivity case was created for the safety and operational analysis of the gFHR reactor.

Finally, the stochastic method for uncertainty propagation were applied to propagate the uncertainty of Serpent/AGREE calculated neutronics parameters to the uncertainty of SAM transient simulation results. The results show that the uncertainties of the maximum coolant and fuel temperatures and the maximum core power in the ramp reactivity transient case are very small when sufficient neutron histories are used in SERPENT to generate the few group macroscopic cross sections. However, when the number of histories is reduced and the uncertainty in the reactivity coefficients is large, the uncertainty in the transient predictions of the SAM code can be non-negligible. The contributions to the uncertainties from different parameters was also assessed which demonstrated that for different responses, the dominate contributions to the uncertainties result from different parameters.

CHAPTER 6

Summary, Conclusion and Future Work

6.1 Summary

There has been considerable research related to the quantification of uncertainties in nuclear reactor analysis methods for both existing light water and advanced reactors. The uncertainty analysis of HTRs was divided into several phases for both the pebble-bed and prismatic HTRs. The essential principles and methods proposed to assess the uncertainty in the HTR were similar in several ways to those used for LWRs. However, the complexity of the modeling required for HTR analysis can potentially introduce additional uncertainties. Specifically, the traditional "two-step" method used for LWR analysis can be less effective for modeling the HTR core. This is primarily because of the high leakage and the significant spatial variations in the neutron spectrum in the core. Several researchers have demonstrated the advantages of using full core Monte Carlo methods to generate homogenized multi-group cross sections for the small reactors such as the HTR. These cross sections are then used in deterministic core simulators for depletion and safety analysis. However, the stochastic nature of Monte Carlo processes has the potential to introduce additional statistical uncertainties in the overall uncertainty in the prediction of the core behavior.

The work performed in this thesis was not to provide a comprehensive uncertainty analysis of the HTR. Rather, the principal objective of the research in this thesis was to quantify the additional uncertainty introduced by the use of Monte Carlo multi-group cross sections into the analysis of the HTR. An overarching objective of the work here was the development of modeling insights and procedures to minimize the contribution of the uncertainty in multi-group cross sections generated by Monte Carlo methods to the overall uncertainty in deterministic calculations.

In this thesis, the objective was achieved by performing uncertainty quantification for the key output parameters in deterministic steady-state and transient safety calculations. The results show that when the homogenized multi-group cross sections are generated with sufficient number of neutron histories in the Monte Carlo calculation, the uncertainties in the subsequent deterministic simulations caused by the Monte Carlo cross section uncertainty are negligible. The percentage contributions from the uncertainties of different input parameters were also analyzed.

6.2 Conclusion

In this thesis, the uncertainty of the deterministic code calculated results due to the uncertainty introduced by preceding Monte Carlo cross section generation were quantified using the industry standard code Dakota. Based on the results obtained in this research, several conclusions were evident.

First, a probabilistic based method was developed for propagating the uncertainty introduced by Monte Carlo cross section generation to the subsequent neutronics and temperature fluids filed simulations, and compared to the results of an analytic perturbation based deterministic method. Both methods were applied to the HTR-10 experiments which were formalized in a IAEA benchmark problem. Good agreement was achieved between the probabilistic and analytic methods.

Second, parametric studies were performed to investigate the factors that would impact the uncertainty quantification. Analysis showed that the correlation between the cross section data was weak, so they could be treated as independent variables in the uncertainty quantification. Furthermore, when the number of neutron histories is fixed in the Monte Carlo cross section generation, the uncertainty is insensitive to the number of energy groups and to the mesh refinement in the neutron diffusion calculation.

Third, the uncertainty of Monte Carlo generated cross sections was propagated for several important neutronics parameters, including the k_{eff} , local power and region-wise reactivity coefficients. An innovative local power form function was developed for the SAM code to improve the accuracy of the point kinetics solution for control rod movement. The results of the uncertainty analysis showed that if a fixed number of neutron histories were used, the uncertainty of the k_{eff} and local power are small, while the uncertainty of some region-wise reactivity coefficients were larger.

Fourth, the uncertainty of Monte Carlo generated cross sections was also propagated to the thermo-fluids parameters in transient simulations through the neutronics parameters. Results showed that despite the uncertainty of some neutronics parameters being larger, the uncertainty of the important thermo-fluids parameters was small, such as the maximum coolant and fuel temperature.

Finally, the contributions of the uncertainty introduced from different neutronics parameters were analyzed in order to provide guidance to reactor analysts on the numbers of histories necessary to minimize the contribution of the uncertainty introduced from Monte Carlo into the prediction of HTR reactor safety performance.

6.3 Future Work

Some areas of future work are suggested to further refine the methods developed in this work. First, in the AGREE-Dakota coupling scheme, the computational burden for the AGREE calculations was significant since it was necessary to run multiple times with a set of sampled input parameters. This was especially the case for the problems requiring very fine 3-D discretizations such as HTR-10 benchmark. Several areas of research are possible, to include methods to better utilize the solutions to the AGREE neutron diffusion equation as initial guess to speed up convergence of the AGREE iterations of the perturbed cases. This research might include the use of reduced order model (eg. digital twins) to accelerate the coupled field solution.

Second, in the AGREE-Dakota coupling calculation, a set of sampled cases were generally performed in parallel on the compute cluster. It was evident that if multiple cases are performed on the same node, the computational time will increase significantly for all cases, despite that the cases being performed on their own processors independently. Several test cases were analyzed and it showed that the memory is not a limitation. This requires further investigated to determine the reasons for the reduced computing performance.

Finally, in the SAM code system modeling of the gFHR reactor, only the reactor core was assessed since the SAM FHR pump model was still under development. Once the pump model and other components models are qualified, a system model of the gFHR reactor should be developed and an uncertainty quantification should be performed using the same methods developed in this thesis.

APPENDIX A

Propogation of Uncertainty

Assuming a variable y is a function of variable $x_1, x_2, \cdots, x_n$:

$$y = F(x_i, x_2, \cdots, x_n) \quad . \tag{A.1}$$

where the uncertainties of variable $x_1, x_2, \cdots, x_n$ are $\Delta_{x_1}, \Delta_{x_2}, \cdots, \Delta_{x_n}$.

Since

$$\mathrm{d}y = \frac{\partial F}{\partial x_1}\mathrm{d}x_1 + \frac{\partial F}{\partial x_2}\mathrm{d}x_2 + \cdots + \frac{\partial F}{\partial x_n}\mathrm{d}x_n \quad , \tag{A.2}$$

the uncertainty of y propogated from the uncertainty of $x_1, x_2, \cdots, x_n$ is

$$\Delta_y = \sqrt{\left(\frac{\partial F}{\partial x_1}\right)^2 (\Delta_{x_1})^2 + \left(\frac{\partial F}{\partial x_2}\right)^2 (\Delta_{x_2})^2 + \cdots + \left(\frac{\partial F}{\partial x_n}\right)^2 (\Delta_{x_n})^2} \quad . \tag{A.3}$$

In some cases, the relative uncertainty of y is more interested. Since

$$\begin{aligned} \frac{\mathrm{d}y}{y} &= \mathrm{d}\ln y \\ &= \frac{\partial \ln F}{\partial x_1}\mathrm{d}x_1 + \frac{\partial \ln F}{\partial x_2}\mathrm{d}x_2 + \cdots + \frac{\partial \ln F}{\partial x_n}\mathrm{d}x_n \quad , \end{aligned} \tag{A.4}$$

the relative uncertainty of y propogated from the uncertainty of $x_1, x_2, \cdots, x_n$ is

$$\frac{\Delta_y}{y} = \sqrt{\left(\frac{\partial \ln F}{\partial x_1}\right)^2 (\Delta_{x_1})^2 + \left(\frac{\partial \ln F}{\partial x_2}\right)^2 (\Delta_{x_2})^2 + \cdots + \left(\frac{\partial \ln F}{\partial x_n}\right)^2 (\Delta_{x_n})^2} \quad . \tag{A.5}$$

Eq. (A.3) and (A.5) are the **Rule of Uncertainty Propogation**.

Based on Eq. (A.3) and (A.5), the uncertainty of some frequently used functions can be obtained:

$$\Delta_z = \sqrt{\Delta_x^2 + \Delta_y^2} \quad , \qquad \text{if} \quad z = x \pm y \quad ; \tag{A.6}$$

$$\frac{\Delta_z}{z} = \sqrt{\left(\frac{\Delta_x}{x}\right)^2 + \left(\frac{\Delta_y}{y}\right)^2} \quad , \qquad \text{if} \quad z = x \pm y \quad \text{or} \quad z = \frac{x}{y} \quad ; \tag{A.7}$$

$$\frac{\Delta_z}{z} = \sqrt{\left(m\frac{\Delta_x}{x}\right)^2 + \left(\frac{n\Delta_y}{y}\right)^2} \quad , \qquad \text{if} \quad z = x^m y^n \quad . \tag{A.8}$$

APPENDIX B

Uncertainty Bounding

Assume there are two correlated cross section data Σ_1, Σ_2. Both of them follow the normal distribution:

$$\Sigma_1 \sim \mathcal{N}(\overline{\Sigma}_1, \Delta_{\Sigma_1}) \tag{B.1}$$

$$\Sigma_2 \sim \mathcal{N}(\overline{\Sigma}_2, \Delta_{\Sigma_2}) \tag{B.2}$$

The covariance between them are $cov(\Sigma_1, \Sigma_2) = cov(\Sigma_2, \Sigma_1)$.

Generate a set of samples for both variables **independently**, say they are

$$\Sigma_1^1, \Sigma_1^2, \Sigma_1^3, \cdots, \Sigma_1^N \tag{B.3}$$

$$\Sigma_2^1, \Sigma_2^2, \Sigma_2^3, \cdots, \Sigma_2^N \quad . \tag{B.4}$$

Run a set of N cases with $\{\Sigma_1^1, \overline{\Sigma}_2\}, \{\Sigma_1^2, \overline{\Sigma}_2\}, \{\Sigma_1^3, \overline{\Sigma}_2\}, \cdots, \{\Sigma_1^N, \overline{\Sigma}_2\}$, the corresponding results are $k_{\text{eff},1}^1, k_{\text{eff},1}^2, k_{\text{eff},1}^3, \cdots, k_{\text{eff},1}^N$. Assuming above results follow a normal distribution

$$k_{\text{eff},1} \sim \mathcal{N}(\overline{k}_{\text{eff},1}, \Delta_{k_{\text{eff},1}}) \tag{B.5}$$

where the mean value and standard deviation

$$\overline{k}_{\text{eff},1} = \frac{1}{N}(k_{\text{eff},1}^1 + k_{\text{eff},1}^2 + k_{\text{eff},1}^3 + \cdots + k_{\text{eff},1}^N) \tag{B.6}$$

$$\Delta_{k_{\text{eff},1}} = \frac{1}{N}\left[(k_{\text{eff},1}^1 - \overline{k}_{\text{eff},1})^2 + (k_{\text{eff},1}^2 - \overline{k}_{\text{eff},1})^2 + (k_{\text{eff},1}^3 - \overline{k}_{\text{eff},1})^2 + \cdots + (k_{\text{eff},1}^N - \overline{k}_{\text{eff},1})^2\right] \tag{B.7}$$

can be calculated.

Thus the sensitivity of k_{eff} with respect to Σ_1 can be obtained:

$$S_{k_{\text{eff}}}^{\Sigma_1} = \frac{\Delta_{k_{\text{eff},1}}}{\Delta_{\Sigma_1}} \tag{B.8}$$

Similarly, the sensitivity of k_{eff} with respect to Σ_2 can be obtained:

$$S_{k_{\text{eff}}}^{\Sigma_2} = \frac{\Delta_{k_{\text{eff},2}}}{\Delta_{\Sigma_2}} \tag{B.9}$$

Since Σ_1 and Σ_2 are correlated, the total uncertainty of k_{eff} can be calculated with the **Sandwich Rule**:

$$\Delta_{k_{\text{eff}}}^2 = \vec{S}^T V \vec{S} \tag{B.10}$$

$$= \left[S_{k_{\text{eff}}}^{\Sigma_1} S_{k_{\text{eff}}}^{\Sigma_1}\right] \begin{bmatrix} cov(\Sigma_1, \Sigma_1) & cov(\Sigma_1, \Sigma_2) \\ cov(\Sigma_2, \Sigma_1) & cov(\Sigma_2, \Sigma_2) \end{bmatrix} \begin{bmatrix} S_{k_{\text{eff}}}^{\Sigma_1} \\ S_{k_{\text{eff}}}^{\Sigma_2} \end{bmatrix} \tag{B.11}$$

where

$$cov(\Sigma_1, \Sigma_1) = \Delta_{\Sigma_1}^2 \tag{B.12}$$

$$cov(\Sigma_2, \Sigma_2) = \Delta_{\Sigma_2}^2 \tag{B.13}$$

$$|cov(\Sigma_1, \Sigma_2)| = |cov(\Sigma_2, \Sigma_1)| \leqslant \sqrt{\Delta_{\Sigma_1}^2 \Delta_{\Sigma_2}^2} = \Delta_{\Sigma_1} \Delta_{\Sigma_2} \tag{B.14}$$

Then Eq.(B.11) yields

$$\Delta_{k_{\text{eff}}}^2 = \left(S_{k_{\text{eff}}}^{\Sigma_1}\right)^2 \Delta_{\Sigma_1}^2 + 2 S_{k_{\text{eff}}}^{\Sigma_1} S_{k_{\text{eff}}}^{\Sigma_2} cov(\Sigma_1, \Sigma_2) + \left(S_{k_{\text{eff}}}^{\Sigma_2}\right)^2 \Delta_{\Sigma_2}^2 \tag{B.15}$$

$$\leqslant \Delta_{k_{\text{eff},1}}^2 \pm 2\Delta_{k_{\text{eff},1}} \Delta_{k_{\text{eff},2}} + \Delta_{k_{\text{eff},2}}^2 \tag{B.16}$$

$$= \left(\Delta_{k_{\text{eff},1}} \pm \Delta_{k_{\text{eff},2}}\right)^2 \tag{B.17}$$

i.e., the uncertainty of k_{eff} can be bounded by

$$\Delta_{k_{\text{eff}}} \leqslant \Delta_{k_{\text{eff},1}} + \Delta_{k_{\text{eff},2}} \tag{B.18}$$

For the more general case with multiple cross section data, Eq.(B.18) becomes

$$\Delta_{k_{\text{eff}}} \leqslant \left|\left|\vec{\Delta}_{k_{\text{eff}}}\right|\right|_1 \tag{B.19}$$

APPENDIX C

Temperature Distribution Convergence

The fuel temperature distribution and coolant temperature distribution calculated based on the HZP cross sections, i.e., Step 2 in Section 4.1.3, are shown in Fig. C.1.

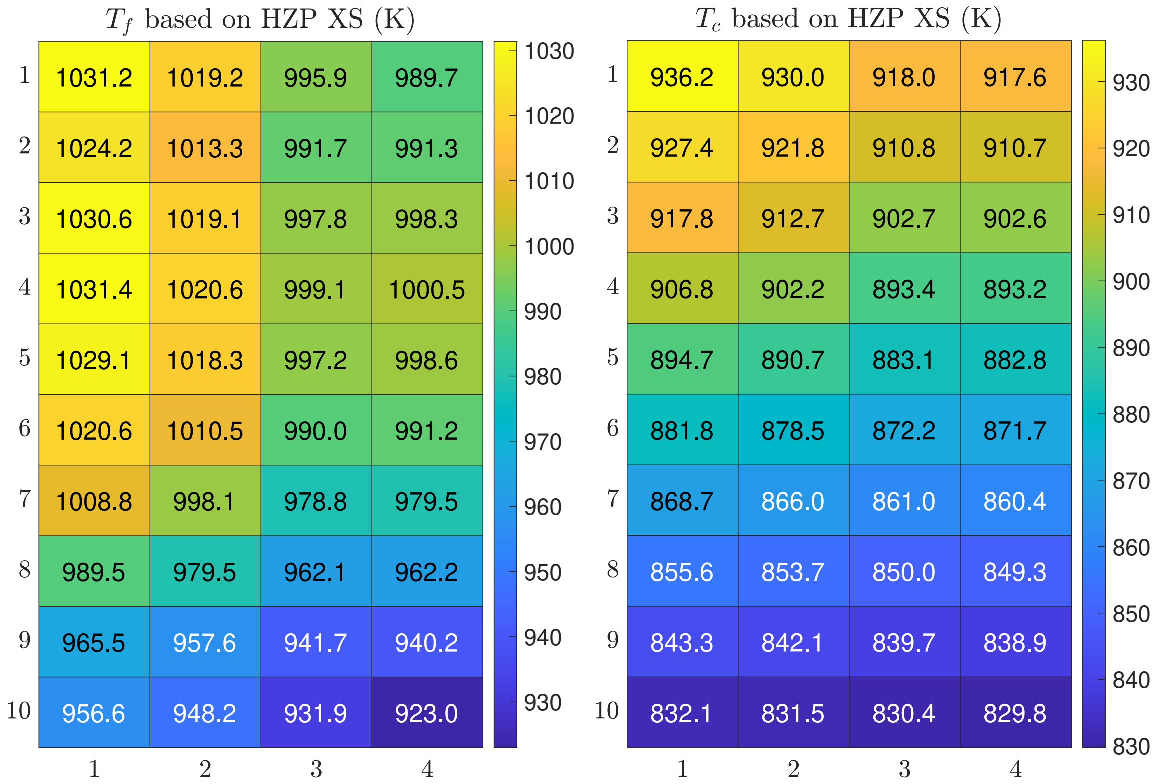

T_f based on HZP XS (K)

	1	2	3	4
1	1031.2	1019.2	995.9	989.7
2	1024.2	1013.3	991.7	991.3
3	1030.6	1019.1	997.8	998.3
4	1031.4	1020.6	999.1	1000.5
5	1029.1	1018.3	997.2	998.6
6	1020.6	1010.5	990.0	991.2
7	1008.8	998.1	978.8	979.5
8	989.5	979.5	962.1	962.2
9	965.5	957.6	941.7	940.2
10	956.6	948.2	931.9	923.0

T_c based on HZP XS (K)

	1	2	3	4
1	936.2	930.0	918.0	917.6
2	927.4	921.8	910.8	910.7
3	917.8	912.7	902.7	902.6
4	906.8	902.2	893.4	893.2
5	894.7	890.7	883.1	882.8
6	881.8	878.5	872.2	871.7
7	868.7	866.0	861.0	860.4
8	855.6	853.7	850.0	849.3
9	843.3	842.1	839.7	838.9
10	832.1	831.5	830.4	829.8

Fig. C.1: The fuel temperature distribution and coolant temperature distribution calculated based on the HZP cross sections

The fuel temperature distribution and coolant temperature distribution calculated based on the HFP cross sections, i.e., Step 3 in Section 4.1.3, are shown in Fig. C.2.

The difference between the fuel and coolant temperature distributions calculated from above two cases are shown in Fig. C.3.

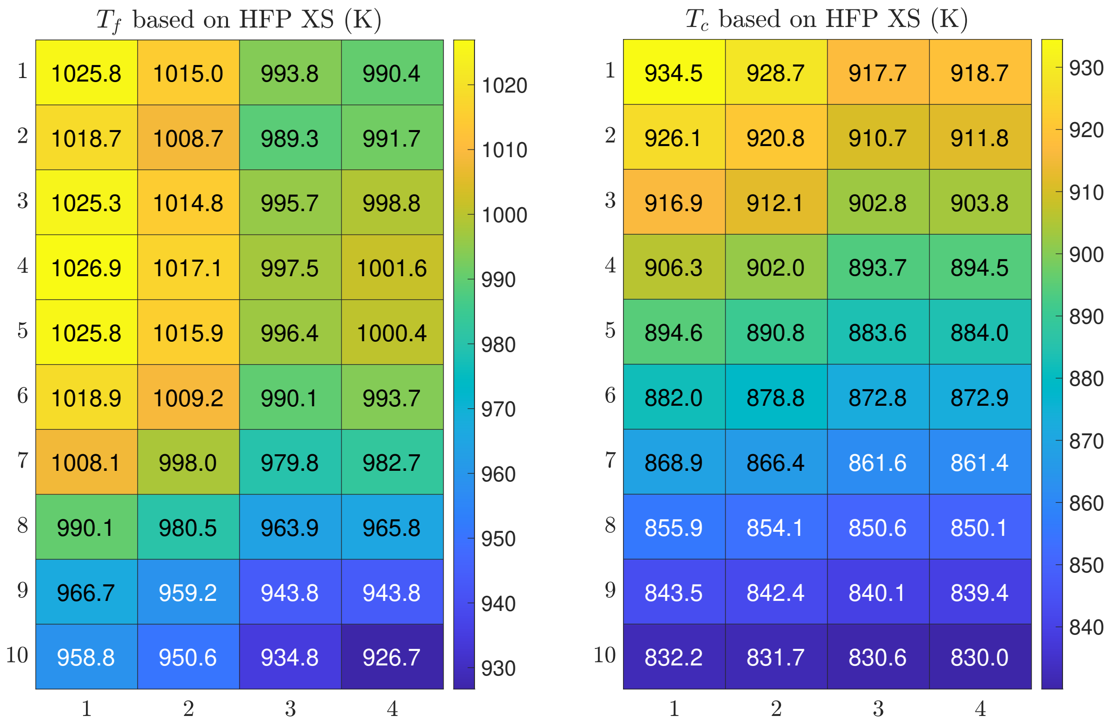

T_f based on HFP XS (K)

	1	2	3	4
1	1025.8	1015.0	993.8	990.4
2	1018.7	1008.7	989.3	991.7
3	1025.3	1014.8	995.7	998.8
4	1026.9	1017.1	997.5	1001.6
5	1025.8	1015.9	996.4	1000.4
6	1018.9	1009.2	990.1	993.7
7	1008.1	998.0	979.8	982.7
8	990.1	980.5	963.9	965.8
9	966.7	959.2	943.8	943.8
10	958.8	950.6	934.8	926.7

T_c based on HFP XS (K)

	1	2	3	4
1	934.5	928.7	917.7	918.7
2	926.1	920.8	910.7	911.8
3	916.9	912.1	902.8	903.8
4	906.3	902.0	893.7	894.5
5	894.6	890.8	883.6	884.0
6	882.0	878.8	872.8	872.9
7	868.9	866.4	861.6	861.4
8	855.9	854.1	850.6	850.1
9	843.5	842.4	840.1	839.4
10	832.2	831.7	830.6	830.0

Fig. C.2: The fuel temperature distribution and coolant temperature distribution calculated based on the HFP cross sections

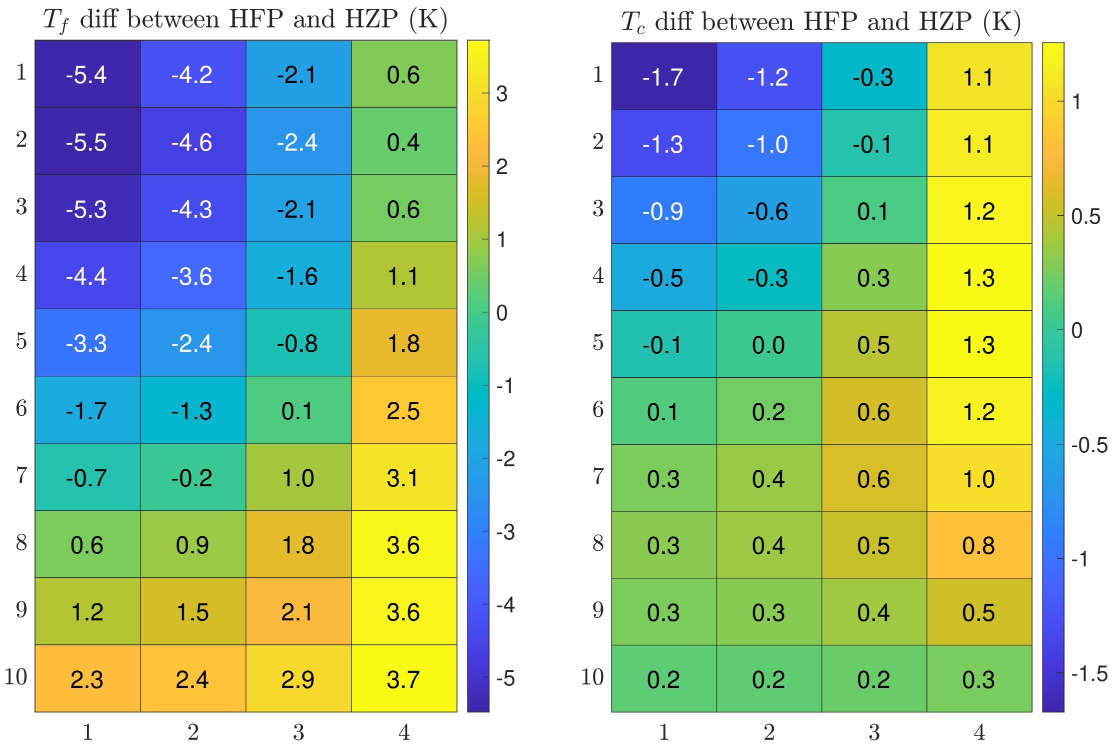

T_f diff between HFP and HZP (K)

	1	2	3	4
1	-5.4	-4.2	-2.1	0.6
2	-5.5	-4.6	-2.4	0.4
3	-5.3	-4.3	-2.1	0.6
4	-4.4	-3.6	-1.6	1.1
5	-3.3	-2.4	-0.8	1.8
6	-1.7	-1.3	0.1	2.5
7	-0.7	-0.2	1.0	3.1
8	0.6	0.9	1.8	3.6
9	1.2	1.5	2.1	3.6
10	2.3	2.4	2.9	3.7

T_c diff between HFP and HZP (K)

	1	2	3	4
1	-1.7	-1.2	-0.3	1.1
2	-1.3	-1.0	-0.1	1.1
3	-0.9	-0.6	0.1	1.2
4	-0.5	-0.3	0.3	1.3
5	-0.1	0.0	0.5	1.3
6	0.1	0.2	0.6	1.2
7	0.3	0.4	0.6	1.0
8	0.3	0.4	0.5	0.8
9	0.3	0.3	0.4	0.5
10	0.2	0.2	0.2	0.3

Fig. C.3: The difference between the fuel and coolant temperature distributions calculated based on the HZP and HFP cross sections

According to Fig. C.3, the differences between the fuel and coolant temperature distributions calculated from the Step 2 and Step 3 in Section 4.1.3 are below 6 K and 2 K, respectively. It shows that even the Step 2 and Step 3 are performed only one time, the temperature distributions are already converged pretty well. Therefore, the Step 2 and Step 3 in Section 4.1.3 are only performed one time in practice.

APPENDIX D

Matrix Structure of the Operators in Neutron Diffusion Equation

In Chapter 3 Eq. 3.2, the neutron diffusion equation is written into a operator form. In a 3-D multi-group discretization, the operator M and F are in matrix form. The matrix structurs of the operator M and F in Eq. 3.2 are shown in Fig. D.1 and Fig. D.2.

$$M = \begin{bmatrix}
A_{1-G}^{1} & \tilde{D}_{1-G}^{2,E,c} & 0 & 0 & \tilde{D}_{1-G}^{m1,S,c} & 0 & \cdots & 0 & \tilde{D}_{1-G}^{m2,T,c} & 0 & 0 \\
\tilde{D}_{1-G}^{1,W,c} & A_{1-G}^{2} & \tilde{D}_{1-G}^{3,E,c} & \ddots & 0 & \ddots & 0 & \vdots & 0 & \ddots & 0 \\
\vdots & \tilde{D}_{1-G}^{2,W,c} & A_{1-G}^{3} & \tilde{D}_{1-G}^{4,E,c} & 0 & \ddots & \tilde{D}_{1-G}^{n-4,S,c} & 0 & \ddots & 0 & \tilde{D}_{1-G}^{n,T,c} \\
0 & \vdots & \tilde{D}_{1-G}^{3,W,c} & A_{1-G}^{4} & \tilde{D}_{1-G}^{5,E,c} & \ddots & 0 & \tilde{D}_{1-G}^{n-3,S,c} & 0 & \vdots & 0 \\
\tilde{D}_{1-G}^{1,N,c} & 0 & \vdots & \tilde{D}_{1-G}^{4,W,c} & A_{1-G}^{5} & \ddots & 0 & 0 & \tilde{D}_{1-G}^{n-2,S,c} & 0 & \vdots \\
0 & \tilde{D}_{1-G}^{2,N,c} & 0 & \vdots & \tilde{D}_{1-G}^{5,W,c} & \ddots & \tilde{D}_{1-G}^{n-4,E,c} & 0 & 0 & \tilde{D}_{1-G}^{n-1,S,c} & 0 \\
\vdots & 0 & \tilde{D}_{1-G}^{3,N,c} & 0 & \vdots & \ddots & A_{1-G}^{n-4} & \tilde{D}_{1-G}^{n-3,E,c} & \ddots & 0 & \tilde{D}_{1-G}^{n,S,c} \\
0 & \vdots & 0 & \tilde{D}_{1-G}^{4,N,c} & 0 & \vdots & \tilde{D}_{1-G}^{n-4,W,c} & A_{1-G}^{n-3} & \tilde{D}_{1-G}^{n-2,E,c} & 0 & 0 \\
\tilde{D}_{1-G}^{1,B,c} & 0 & \ddots & 0 & \tilde{D}_{1-G}^{5,N,c} & \ddots & \vdots & \tilde{D}_{1-G}^{n-3,W,c} & A_{1-G}^{n-2} & \tilde{D}_{1-G}^{n-1,E,c} & 0 \\
0 & \ddots & \ddots & \vdots & 0 & \ddots & 0 & \vdots & \tilde{D}_{1-G}^{n-2,W,c} & A_{1-G}^{n-1} & \tilde{D}_{1-G}^{n,E,c} \\
0 & 0 & \tilde{D}_{1-G}^{n-m2+1,B,c} & 0 & \cdots & 0 & \tilde{D}_{1-G}^{n-m1+1,N,c} & 0 & 0 & \tilde{D}_{1-G}^{n-1,W,c} & A_{1-G}^{n}
\end{bmatrix}$$

Fig. D.1: Matrix structure of operator M in neutron diffusion equation

$$F = \begin{bmatrix}
f_{1-G}^{1} & & & \\
& f_{1-G}^{2} & & \\
& & \ddots & \\
& & & f_{1-G}^{n}
\end{bmatrix} = \begin{bmatrix}
\chi_1 \upsilon \Sigma_{f,1}^{1} & \cdots & \chi_1 \upsilon \Sigma_{f,G}^{1} & & & & \\
\vdots & \ddots & \vdots & & & & \\
\chi_G \upsilon \Sigma_{f,1}^{1} & \cdots & \chi_G \upsilon \Sigma_{f,G}^{1} & & & & \\
& & & \ddots & & & \\
& & & & \chi_1 \upsilon \Sigma_{f,1}^{n} & \cdots & \chi_1 \upsilon \Sigma_{f,G}^{n} \\
& & & & \vdots & \ddots & \vdots \\
& & & & \chi_G \upsilon \Sigma_{f,1}^{n} & \cdots & \chi_G \upsilon \Sigma_{f,G}^{n}
\end{bmatrix}$$

Fig. D.2: Matrix structure of operator F in neutron diffusion equation where A are $G \times G$ block matrices, while $\tilde{D}$ are $G \times G$ diagonal matrices.

In 3-D discretization, the operator M is a seven-diagonal matrix since each spatial region is connected to its six neighbors. In 2-D discretization, the operator M is a five-diagonal matrix since each spatial region is connected to its four neighbors.

For the 3×5 simplified gFHR fresh core demonstration model created in Chapter 3 Section 3.3.1, the matrix structures of the operator M and operator F are shown in Fig. D.3. The connections between a spatial region with its four neighbors are shown in colored blocks. When a cross section is perturbed, only the corresponding block in the operator M and F will be changed. Therefore, to obtain the perturbed operator ΔM and ΔF, only several entries in the matrix need to be considered.

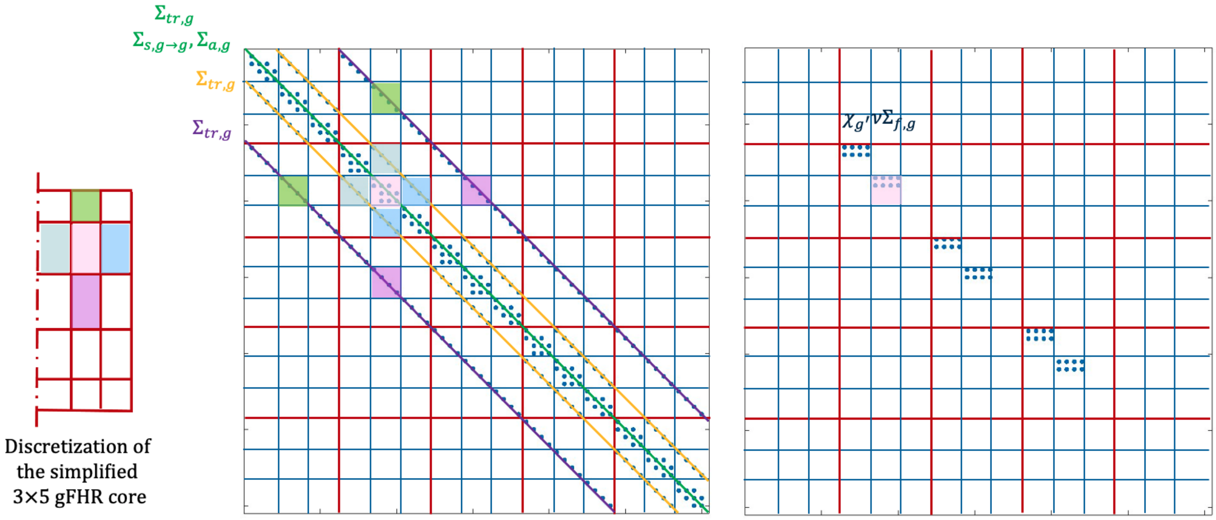

Discretization of the simplified 3×5 gFHR core

Matrix of operator ***M***

Matrix of operator ***F***

Fig. D.3: Matrix structure of operator M and F for the 3×5 demonstration model

BIBLIOGRAPHY

[1] Nicolas Zweibaum, Zhangpeng Guo, James Kendrick, and Per Peterson. Design of the Compact Integral Effects Test Facility and Validation of Best-Estimate Models for Fluoride Salt–Cooled High-Temperature Reactors. *Nuclear Technology*, 196, December 2016.

[2] IAEA. *Best Estimate Safety Analysis for Nuclear Power Plants: Uncertainty Evaluation*. Intl Atomic Energy Agency, Vienna, August 2008.

[3] Raluca O. Scarlat and Per F. Peterson. The current status of fluoride salt cooled high temperature reactor (FHR) technology and its overlap with HIF target chamber concepts. *Nuclear Instruments and Methods in Physics Research Section A: Accelerators, Spectrometers, Detectors and Associated Equipment*, 733:57–64, January 2014.

[4] A. Louis Qualls, Benjamin R. Betzler, Nicholas R. Brown, Juan J. Carbajo, M. Scott Greenwood, Richard Hale, Thomas J. Harrison, Jeffrey J. Powers, Kevin R. Robb, Jerry Terrell, Aaron J. Wysocki, Jess C. Gehin, and Andrew Worrall. Preconceptual design of a fluoride high temperature salt-cooled engineering demonstration reactor: Motivation and overview. *Annals of Nuclear Energy*, 107:144–155, September 2017.

[5] A. J. Novak, R. W. Carlsen, S. Schunert, P. Balestra, D. Reger, R. N. Slaybaugh, and R. C. Martineau. Pronghorn: A Multidimensional Coarse-Mesh Application for Advanced Reactor Thermal Hydraulics. *Nuclear Technology*, 207(7):1015–1046, July 2021. Publisher: Taylor & Francis _eprint: https://doi.org/10.1080/00295450.2020.1825307.

[6] A. J. Novak, S. Schunert, R. W. Carlsen, P. Balestra, R. N. Slaybaugh, and R. C. Martineau. Multiscale thermal-hydraulic modeling of the pebble bed fluoride-salt-cooled high-temperature reactor. *Annals of Nuclear Energy*, 154:107968, May 2021.

[7] Rui Hu, Ling Zou, and Guojun Hu. SAM User's Guide. Technical Report ANL/NSE-19/18, Argonne National Lab. (ANL), Argonne, IL (United States), August 2019.

[8] Zhiee Jhia Ooi, Ling Zou, Thanh Hua, Jun Fang, and Rui Hu. Modeling of a Generic Pebble Bed High-temperature Gas-cooled Reactor (PB-HTGR) with SAM. Technical Report ANL/NSE-22/59, Argonne National Lab. (ANL), Argonne, IL (United States), September 2022.

[9] Guojun Hu, Daniel O'Grady, Ling Zou, and Rui Hu. Development of a Reference Model for Molten-Salt-Cooled Pebble-Bed Reactor Using SAM. Technical Report ANL/NSE-20/31, Argonne National Lab. (ANL), Argonne, IL (United States), September 2020.

[10] Elia Merzari, Paul Fischer, Misun Min, Stefan Kerkemeier, Aleksandr Obabko, Dillon Shaver, Haomin Yuan, Yiqi Yu, Javier Martinez, Landon Brockmeyer, Lambert Fick, Giacomo Busco, Alper Yildiz, and Yassin Hassan. Toward Exascale: Overview of Large Eddy Simulations and Direct Numerical Simulations of Nuclear Reactor Flows with the Spectral Element Method in Nek5000. *Nuclear Technology*, 206(9):1308–1324, September 2020. Publisher: Taylor & Francis _eprint: https://doi.org/10.1080/00295450.2020.1748557.

[11] Elia Merzari, Haomin Yuan, Misun Min, Dillon Shaver, Ronald Rahaman, Patrick Shriwise, Paul Romano, Alberto Talamo, Yu-Hsiang Lan, Derek Gaston, Richard Martineau, Paul Fischer, and Yassin Hassan. Cardinal: A Lower-Length-Scale Multiphysics Simulator for Pebble-Bed Reactors. *Nuclear Technology*, 207(7):1118–1141, July 2021. Publisher: Taylor & Francis _eprint: https://doi.org/10.1080/00295450.2020.1824471.

[12] David Reger, Elia Merzari, Paolo Balestra, Ryan Stewart, and Gerhard Strydom. Discrete element simulation of Pebble Bed Reactors on graphics processing units. *Annals of Nuclear Energy*, 190:109896, September 2023.

[13] Friederike Bostelmann, G. Strydom, Frederik Reitsma, and Kostadin Ivanov. The IAEA coordinated research programme on HTGR uncertainty analysis: Phase I status and Ex. I-1 prismatic reference results. *Nuclear Engineering and Design*, 306, 2016.

[14] Frederik Reitsma, Gerhard Strydom, Bismark Tyobeka, and Kostadin Ivanov. The IAEA Coordinated Research Program on HTGR Reactor Physics, Thermal-hydraulics and Depletion Uncertainty Analysis: Description of the Benchmark Test Cases and Phases. Technical Report INL/CON-12-26565, Idaho National Lab. (INL), Idaho Falls, ID (United States), October 2012.

[15] RYAN N. Bratton, M. Avramova, and K. Ivanov. OECD/NEA BENCHMARK FOR UNCERTAINTY ANALYSIS IN MODELING (UAM) FOR LWRS – SUMMARY AND DISCUSSION OF NEUTRONICS CASES (PHASE I). *Nuclear Engineering and Technology*, 46(3):313–342, 2014.

[16] G Zhang, Kaiyue Zeng, N Stauff, Jason Hou, T Kim, and Thomas Fanning. UNCERTAINTY QUANTIFICATION OF ABR TRANSIENT SAFETY ANALYSIS. May 2018.

[17] N Stauff, Kaiyue Zeng, G Zhang, Gerardo Aliberti, Jason Hou, Thomas Fanning, and T Kim. UNCERTAINTY QUANTIFICATION OF ABR TRANSIENT SAFETY ANALYSIS - NUCLEAR DATA UNCERTAINTIES. May 2018.

[18] Guanheng Zhang, Acacia Brunett, Tyler Sumner, Nicolas Stauff, and Thomas Fanning. Dakota-SAS4A/SASSYS-1 Coupling for Uncertainty Quantification and Optimization Analysis. April 2017.

[19] Andy Rivas, Nicolas Stauff, Tyler Sumner, and Jason Hou. Propagating neutronic uncertainties for FFTF LOFWOS Test #13. *Nuclear Engineering and Design*, 375:111047, April 2021.

[20] Joel Aaron Kulesza, Terry R. Adams, Jerawan Chudoung Armstrong, Simon R. Bolding, Forrest Brooks Brown, Jeffrey S. Bull, Timothy Patrick Burke, Alexander Rich Clark, Robert Arthur Forster, III, Jesse Frank Giron, Tristan Sumner Grieve, Colin James Josey, Roger Lee Martz, Gregg Walter McKinney, Eric J. Pearson, Michael Evan Rising, Clell Jeffrey Solomon, Jr., Sriram Swaminarayan, Travis John Trahan, Stephen Christian Wilson, and Anthony J. Zukaitis. MCNP® Code Version 6.3.0 Theory & User Manual. Technical Report LA-UR-22-30006, Rev. 1, Los Alamos National Laboratory, Los Alamos, NM, USA, September 2022.

[21] Paul K. Romano, Nicholas E. Horelik, Bryan R. Herman, Adam G. Nelson, Benoit Forget, and Kord Smith. OpenMC: A state-of-the-art Monte Carlo code for research and development. *Annals of Nuclear Energy*, 82:90–97, August 2015.

[22] Jaakko Leppänen, Maria Pusa, Tuomas Viitanen, Ville Valtavirta, and Toni Kaltiaisenaho. The Serpent Monte Carlo code: Status, development and applications in 2013. *Annals of Nuclear Energy*, 82:142–150, August 2015.

[23] Kan Wang, Zeguang Li, Ding She, Jin'gang Liang, Qi Xu, Yishu Qiu, Jiankai Yu, Jialong Sun, Xiao Fan, and Ganglin Yu. RMC – A Monte Carlo code for reactor core analysis. *Annals of Nuclear Energy*, 82:121–129, August 2015.

[24] B. Kochunas, B. Collins, D. Jabaay, T. J. Downar, and W. R. Martin. *Overview of development and design of MPACT: Michigan parallel characteristics transport code*. American Nuclear Society - ANS, United States, 2013. INIS Reference Number: 45033649.

[25] Boyan D. Ivanov, Kostadin N. Ivanov, and Rudi J. J. Stamm'ler. Helios, current coupling collision probability method, applied for solving the NEA C5G7 MOX benchmark. *Progress in Nuclear Energy*, 45(2):119–124, January 2004.

[26] Volkan Seker and Thomas Downar. Kairos power advanced gas reactor evaluator theory manual. Technical report, University of Michigan (United States), 2019.

[27] Jaakko Leppänen. Two practical methods for unionized energy grid construction in continuous-energy Monte Carlo neutron transport calculation. *Annals of Nuclear Energy*, 36(7):878–885, July 2009.

[28] Yuxuan Liu, Ding She, Kan Wang, and Ganglin Yu. Optimization treatment of point-wise nuclear data in Monte Carlo criticality and burnup calculations. *Annals of Nuclear Energy*, 38(7):1489–1495, July 2011.

[29] Yuxuan Liu and William R. Martin. Assessment of homogeneous and heterogeneous resonance integral tables and their applications to the embedded self-shielding method. *Annals of Nuclear Energy*, 92:186–197, June 2016.

[30] Sooyoung Choi, Kord S. Smith, Hanjoo Kim, Taewoo Tak, and Deokjung Lee. On the diffusion coefficient calculation in two-step light water reactor core analysis. *Journal of Nuclear Science and Technology*, 54(6):705–715, 2017. Publisher: Taylor & Francis _eprint: https://doi.org/10.1080/00223131.2017.1299648.

[31] Antonio Dambrosio, Marek Ruščák, Mazzini Guido, and Alis Musa. Neutronic analysis of the LVR-15 research reactor using the PARCS code. *Annals of Nuclear Energy*, 117:145–154, 2018.

[32] Zeyun Wu, Qiong Zhang, and Hany Abdel-Khalik. Hybrid Monte Carlo-Deterministic Methods for Reactor Analysis. *Nuclear Technology*, 180:372–382, 2012.

[33] Giorgio Locatelli, Mauro Mancini, and Nicola Todeschini. Generation IV nuclear reactors: Current status and future prospects. *Energy Policy*, 61:1503–1520, 2013.

[34] H. Ardiansyah, V. Seker, T. Downar, S. Skutnik, and W. Wieselquist. Evaluation of PBMR-400 Core Design Steady State Condition with Serpent and AGREE. *Journal of Physics: Conference Series*, 2048(1):012024, 2021. Publisher: IOP Publishing.

[35] E. Fridman and J. Leppänen. On the use of the Serpent Monte Carlo code for few-group cross section generation. *Annals of Nuclear Energy*, 38(6):1399–1405, June 2011.

[36] Jaakko Leppänen, Maria Pusa, and Emil Fridman. Overview of methodology for spatial homogenization in the Serpent 2 Monte Carlo code. *Annals of Nuclear Energy*, 96:126–136, October 2016.

[37] INTERNATIONAL ATOMIC ENERGY AGENCY. Current Status and Future Development of Modular High Temperature Gas Cooled Reactor Technology. Text IAEA-TECDOC-1198, IAEA, February 2001. Publisher: IAEA.

[38] Yuanhui Xu and Kaifen Zuo. Overview of the 10 MW high temperature gas cooled reactor—test module project. *Nuclear Engineering and Design*, 218(1):13–23, 2002.

[39] International Atomic Energy Agency. *Evaluation of high temperature gas cooled reactor performance: benchmark analysis related to initial testing of the HTTR and HTR-10.* International Atomic Energy Agency, Vienna, 2003. OCLC: 68944964.

[40] International Atomic Energy Agency. *Evaluation of high temperature gas cooled reactor performance: benchmark analysis related to the PBMR-400, PBMM, GT-MHR, HTR-10 and the ASTRA critical facility.* 2013. OCLC: 857246871.

[41] Volkan Şeker and Üner Çolak. HTR-10 full core first criticality analysis with MCNP. *Nuclear Engineering and Design*, 222(2):263–270, 2003.

[42] Douglas W. (ORCID:0000000238210025) Marshall. AGR-5/6/7 Fuel Fabrication Report. Technical Report INL/EXT-19-53720-Rev000, Idaho National Lab. (INL), Idaho Falls, ID (United States), May 2019.

[43] Nader Satvat, Fatih Sarikurt, Kevin Johnson, Ian Kolaja, Massimiliano Fratoni, Brandon Haugh, and Edward Blandford. Neutronics, thermal-hydraulics, and multi-physics benchmark models for a generic pebble-bed fluoride-salt-cooled high temperature reactor (FHR). *Nuclear Engineering and Design*, 384:111461, December 2021.

[44] Kairos Power. Generic FHR Core Model – Kairos Power.

[45] Keith R. Dalbey, Michael S. Eldred, Gianluca Geraci, John D. Jakeman, Kathryn A. Maupin, Jason A. Monschke, Daniel Thomas Seidl, Anh Tran, Friedrich Menhorn, and Xiaoshu Zeng. Dakota, A Multilevel Parallel Object-Oriented Framework for Design Optimization, Parameter Estimation, Uncertainty Quantification, and Sensitivity Analysis: Version 6.16 Theory Manual. Technical Report SAND2022-6172, Sandia National Lab. (SNL-NM), Albuquerque, NM (United States), January 2021.

[46] Kairos Power. Equilibrium core concentrations.

[47] Volkan Seker and Thomas Downar. Kairos power advanced gas reactor evaluator user's manual. Technical report, University of Michigan (United States), November 2018.

[48] Rike Bostelmann, Cihangir Celik, Robert F. Kile, and William A. Wieselquist. SCALE Analysis of a Fluoride Salt-Cooled High-Temperature Reactor in Support of Severe Accident Analysis. Technical Report ORNL/TM-2021/2273, Oak Ridge National Lab. (ORNL), Oak Ridge, TN (United States), March 2022.

[49] A. Ward, Y. Xu, and T. Downar. Code for Generating the PARCS Cross Section Interface File PMAXS. Technical report, University of Michigan, February 2021.

[50] T. Folk, D. Price, B. Kochunas, S. Srivastava, and K. Garikipati. Analytic error analysis of cross section interpolation methods in nodal diffusion codes - I : Theory. In *Proceedings of the international conference on physics of reactors (PHYSOR 2022)*, Pittsburgh, United States, 2022. ANS - American Nuclear Society. INIS Reference Number: 54002266.

[51] Kairos Power. Generic FHR Reactivity Control System, October 2021.

[52] Rui Hu, Ling Zou, Guojun Hu, Daniel Nunez, Travis Mui, and Tingzhou Fei. SAM Theory Manual. Technical Report ANL/NSE-17/4 Rev. 1, Argonne National Lab. (ANL), Argonne, IL (United States), February 2021.

[53] Manohar S. Sohal, Matthias A. Ebner, Piyush Sabharwall, and Phil Sharpe. Engineering Database of Liquid Salt Thermophysical and Thermochemical Properties. Technical Report INL/EXT-10-18297, Idaho National Lab. (INL), Idaho Falls, ID (United States), March 2010.